NTNU – Trondheim
Norwegian University of
Science and Technology

Unconventional Propeller Tip Design

Hydrodynamic Study

Andreas Ommundsen

Marine Technology
Submission date: June 2015
Supervisor: Håvard Holm, IMT

Norwegian University of Science and Technology
Department of Marine Technology

Preface

This Master's Thesis was written in the final term of the engineering studies with specialisation in hydrodynamics at the Marine Technology Centre in Trondheim, under the Norwegian University of Science and Technology. The topic of unconventional propellers was chosen because of curiosity and an interest in CFD. It was a very fascinating subject to study, and I learned a lot during the process.

There are probably always things one should have done differently, but that is easier to see in hindsight than right in the middle of the thesis work. It would be interesting to test many variants of winglet designs, but there was simply not enough time. The lifting line computer program was more time demanding to write than first anticipated, but proved very useful in the design process and overall understanding of how propellers are engineered.

Thanks go to my supervisor, Associate Professor Håvard Holm, for good help and very supportive guidance meetings. Thanks are also given to my co-supervisor Professor Sverre Steen for valuable help in understanding the lifting line theory and propeller theory in general. I also want to thank my second co-supervisor Luca Savio, working at SINTEF MARINTEK, especially for giving great tips of what to include in the post processing of the CFD results.

Trondheim, June 2015
Andreas Ommundsen

Abstract

The use of winglets on aircraft wings have proven to be beneficial regarding resistance and efficiency. Devices like these have seen little use on ship propellers, which also in essence are wings, only in a rotating motion. Propeller blades create lift by sustaining a pressure difference between the two surfaces, but this pressure difference will naturally vanish as soon as the span of the blade ends. The lift on the outer sections of the propeller blade will therefore be reduced, and vortices are formed because of the pressure leakage around the blade tip. These vortices will also induce velocities on the blade which alters the angle of inflow, and effectively the propeller pitch. The induced velocities will also induce a drag component, implying that it is wise to minimise them. A winglet is able to sustain the pressure difference further towards the blade tip by acting as a physical barrier against the pressure leakage, and at the same time reduce the tip vortices and induced velocities. It will in addition, if designed carefully, be able to create a small thrust in the direction of travel.

A conventional propeller has its lift distributed such that the blade is unloaded to zero at the tip to minimise the forming of tip vortices. This also indicates that the outer blade sections are not lifting optimally. The idea of a winglet is that the lift can be maintained further towards the tip, and rather go to zero at the winglet.

A computer program based on two-dimensional lifting line theory with the induction factor method was therefore written in order to design a propeller with an arbitrary lift distribution. Two different propellers were modelled from the same criteria – one with lift equal to zero on the blade tip, and one with a finite loading. The tip loaded propeller was the basis for the winglet propellers, of which two were made – one with a tall, and one with a shorter winglet.

A detailed CFD analysis was conducted on all the propellers. The results were presented in open water diagrams, and with figures of cavitation patterns and vorticity details. The winglet propellers were then compared with the conventional propeller, which served as the reference.

The goal of higher efficiency was not reached. The thrust increased by 24.5 % and 40.3 % at the operating point for the short and tall winglet respectively – while the torque increased by 34.4 % and 58.8 % for the short and tall winglet respectively. This lead to an efficiency reduction of 5.5 and 8.7 percentage points respectively. The cavitation performance of the winglet propellers were also worse than for the conventional propeller. It is assumed that the negative effects are connected to the design of the winglets. They did not follow the radial curvature of propeller circle correctly, and will therefore be oriented at an angle of attack on the inflow. A larger pressure resistance is also likely, but it was in addition observed larger tip vortices for the winglet propellers, something that contributes to a higher torque. Increased viscous resistance is also a factor that will increase the torque.

The reason for the thrust to go up is believed to be the sustaining of the pressure difference towards the blade tip, and the fact that the tip vortex was displaced away from the propeller blade and up to the top of the winglet. This leads to lower induced velocities at the blade, and therefore a higher pitch at the outer blade sections.

It is nevertheless concluded that there may be a potential in this type of propellers if the winglet is designed carefully.

Sammendrag

Bruken av winglets på flyvinger har vist seg å være fordelaktig med tanke på motstand og effektivitet. Det har vært lite å se til den typen innretninger på skipspropeller, som i og for seg også er vinger, bare i en roterende bevegelse. Et propellblad skaper løft ved å opprettholde en trykkforskjell mellom de to overflatene, men denne trykkforskjellen vil naturlig nok opphøre så snart bladet stopper opp. Løftet på de ytre seksjonene av propellbladet vil derfor være redusert, og det dannes i tillegg virvler på grunn av trykklekkasjen rundt bladtuppen. Disse virvlene vil indusere hastigheter på bladet som endrer innstrømningsvinkelen, og i praksis stigningen på propellen. De induserte hastighetene vil også indusere en motstandskomponent, noe som vil si at det er fordelaktig å minimere dem. En winglet vil kunne opprettholde trykkforskjellen lengre ut mot bladtuppen ved å virke som en fysisk barriere mot trykklekkasjen, samtidig som den også ideelt sett er med på å redusere endetuppvirvlene og de induserte hastighetene. I tillegg vil den, hvis den er designet riktig, være med på å skape en liten skyvkraft i fartsretningen.

En konvensjonell propell har løftet sitt fordelt slik at bladet avlastes til null mot tuppen, nettopp for å minimere dannelsen av tuppvirvler. Det vil si at også en stor del av de ytre bladseksjonene ikke løfter optimalt. Ideen bak en winglet er at løftet kan opprettholdes lengre ut mot tuppen, og heller gå mot null på wingleten.

Et dataprogram basert på todimensjonal løftelinjeteori med induksjonsfaktormetoden ble derfor skrevet for å kunne designe en propell med en vilkårlig løftfordeling. To ulike propeller ble modellert ut fra de samme kriteriene – den ene med løft lik null på bladtuppen, og den andre med en endelig belastning. Den tuppbelastede propellen var utgangspunktet for wingletpropellene, som det ble laget to varianter av – en med høy og en med lavere winglet.

En detaljert CFD-analyse ble gjennomført på alle propellene. Resultatene ble framstilt i friprøvediagram, og med bilder av kavitasjonsmønstre og virvlingsdetaljer. Wingletpropellene ble så sammenlignet med den konvensjonelle propellen, som ble brukt som referansegrunnlag.

Målet om høyere virkningsgrad ble ikke nådd. På operasjonspunktet økte skyvkraften med 24,5 % og 40,3 % for propellene med henholdsvis lav og høy winglet – mens dreiemomentet økte med henholdsvis 34,4 % og 58,8 %. Det førte til en reduksjon i virkningsgraden på henholdsvis 5,5 og 8,7 prosentpoeng. Kavitasjonsegenskapene var også dårligere for wingletpropellene enn den konvensjonelle propellen. Det antas at grunnen til de negative effektene er knyttet opp til utformingen av wingletene. De følger ikke kurvaturen til propellsirkelen korrekt, og vil derfor stå med en angrepsvinkel på innstrømningen. Større trykkmotstand er også sannsynlig, men det ble i tillegg observert større tuppvirvler for wingletpropellene, noe som også bidrar til økt dreiemoment. Større viskøs motstand vil også bidra til det økte dreiemomentet.

Grunnen til at skyvkraften gikk opp antas å være at trykkforskjellen ble opprettholdt lengre ut mot bladtuppen, og at tuppvirvelen ble flyttet vekk fra propellbladet og opp til toppen av wingleten. Dette fører til lavere induserte hastigheter på bladet, og derfor en høyere stigning ved de ytre bladseksjonene.

Det konkluderes likevel med at det kan ligge et potensiale i denne typen propeller hvis wingleten designes med stor nøyaktighet.

Nomenclature

g	Acceleration of gravity
u	Velocity in x-direction
v	Velocity in y-direction
w	Velocity in z-direction
V	Free stream velocity
V_0	Ship speed
V_A	Advance velocity
V_L	Local velocity
V_t	Total velocity
u_*	Friction velocity
U_A	Induced axial velocity
U_T	Induced tangential velocity
i_a	Axial induction factor
i_t	Tangential induction factor
β_i	Hydrodynamic angle of attack
α	Angle of attack
α_i	Ideal angle of attack
ρ	Density
p	Pressure
p_v	Vapour pressure
σ	Cavitation number, structural stress
σ_y	Structural yield stress
I	Second area of moment
M	Bending moment
C_p	Pressure coefficient
C_L	Lift coefficient
C_D	Drag coefficient
C_F	Friction coefficient
Re	Reynolds' number
F_n	Froude's number
t	Thickness
c	Chord length
r	Radial position
R	Propeller radius
D	Propeller diameter, drag force
P	Propeller pitch
n	Propeller speed in rps
L	Lift force
T	Propeller thrust
Q	Propeller torque
η	Propeller efficiency
K_T	Thrust coefficient
K_Q	Torque coefficient
J	Advance number
Z	Number of blades
w	Wake factor
Γ	Circulation
k	Circulation factor
k_c	Camber factor
k_a	Angle of attack factor
k_t	Thickness factor
$y+$	Wall distance
τ_w	Wall shear stress
EAR	Expanded Area Ratio
ϕ	General scalar
$\mathrm{P_D}$	Delivered power
ν	Kinematic viscosity
μ	Dynamic viscosity

Contents

Chapter 1

Introduction

1.1 Motivation and Objectives

Tip modified wing sections have been used in the aircraft industry for quite some time – dating back to Sighard F. Hoerner's work from the 1950's (Hoerner 1952), and in particular Richard T. Whitcomb's work from the 1970's (Whitcomb 1976).

Most wing tip devices have in common that they form a physical barrier between the suction and pressure sides of the lifting surface, preventing some of the pressure leakage at the tip from taking place. This increases the lift, and reduces the wing tip vortices – furthermore reducing the downwash and drag. In addition, modern *winglets* are lifting surfaces themselves, managing to create a slight forward thrust by utilising the flow from the wing tip vortices, as seen in Figure 1.1 below.

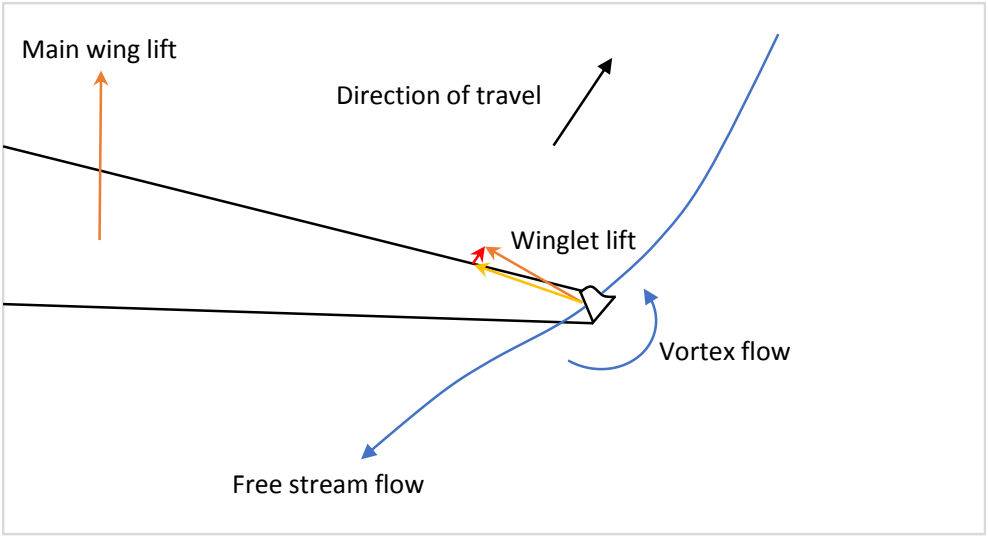

Figure 1.1: Overview of the flow around a winglet fitted wing. The vortex flow alters the inflow to the winglet. As the winglet creates a lift that is normal to the free stream flow, the lift may be decomposed into a thrust component that is aligned with the direction of travel (red arrow). The winglet also has a drag component, but it is lower than the resulting thrust.

The motivation behind this thesis is simple. Winglets have been successful in the aircraft industry – so why have similar designs not been applied to marine propellers, which are lifting surfaces too? The aim is to figure out if there could be potential performance gains for a marine propeller by applying aircraft inspired lifting winglets. Special emphasis is put on the open water efficiency, but all the propeller coefficients, as well as the cavitation performance and

vorticity details will also be covered. This is in accordance with the thesis problem text, which is cited below.

Thesis Problem Text

"The main objective of the thesis is to study the effects of adding aircraft style winglets to marine propellers, with special emphasis put on the open water efficiency. A litterature study should be conducted to see what has been achieved already in the field of unconventional tip designs.

New variants of winglet designs should be modelled and analysed with state of the art CFD software, and the results should be presented in a thorough manner."

1.2 Previous Work

There are two major propeller tip modified designs that have been studied, namely the 'Contracted and Loaded Tip' (CLT) propeller, and the 'Kappel' propeller. Both of them have a thorough theoretical foundation and have also been tested in full-scale on a diverse range of ships. The results are promising, and claims of notable efficiency gains have been reported.

1.2.1 The 'Contracted and Loaded Tip' Propeller

The CLT propeller originated in the wake of a 1976 study on Tip Vortex Free propellers of G. Perez Gomez (Gennaro and Gonzalez-Adalid 2012). The spanish company SISTEMAR was established in 1987 to further develop the design and to commercialise the product.

The CLT propeller differs considerably from a conventional design, with the most visibly striking being the substantial tip chord length and large end-plates, which follow the entire tip chord and point towards the blades' pressure sides. Little skew is also a common feature.

Figure 1.2: A 5.25 m diameter fixed pitch CLT propeller installed behind a wake equalising duct on the tanker M/T 'Roy Maersk' of A.P. Møller – Mærsk (The Motorship 2012a).

The blade tip is loaded, with the unloaded end-plates acting as barriers between the suction and pressure sides of the propeller, thereby preventing pressure leakage over the tip. The end-plates are positioned at a sharp angle to the blades, and runs along the entire tip chord length.

The main goal of the CLT propeller is to improve the open water efficiency by reducing the hydrodynamic angle of attack (β_i in Figure 2.4) through a reduction of the induced velocities (Gennaro and Gonzalez-Adalid 2012). An increase in the efficiency of 5 to 8 % over the entire operational range have been reported, as well as lower induced noise and vibrations and better manoeuvrability (Gonzalez-Adalid and Gennaro 2011). These results are presented by SISTEMAR themselves, and should be taken with a grain of salt – but it is worth noting that A.P. Møller – Mærsk decided that the CLT propeller was the most promising energy saving device after a research and development program, also involving model trials at The Hamburg Ship Model Basin (HSVA) and CEHIPAR in Madrid. As shown in Figure 1.2, 'Roy Maersk' was retrofitted with a CLT propeller in 2009, and promising results were obtained after a long research period (Gonzalez-Adalid and Gennaro 2011).

The large number of vessels fitted with CLT propellers (around 300) is an indication for the maturity of the design. Vessels ranging from hydrofoils to bulk carriers and VLCC's (Very Large Crude Carriers) have successfully been using CLT propellers.

Figure 1.3: A hydrofoil vessel fitted with two fixed pitch CLT propellers (Gonzalez-Adalid and Gennaro 2011).

So, why are not every single new build then fitted with CLT propellers? There are, according to a thorough study, possibly several reasons for this (Bertetta et al. 2012). The shape and position of the end-plates introduce mechanical strength issues, and there are also a higher risk of double tip vortex cavitation (i.e cavitation vortices originating from two locations on the propeller tip). Since tip vortices are a significant source of energy loss and hydroacoustic noise, it is important to have a proper understanding of the vortex dynamics, which is more challenging for an unconventional propeller like the CLT design. The geometry is also likely to produce a very complex wake field which interacts with the tip vortices. Another important aspect is that the scale effects are not yet fully understood. The study also revealed that the presence of the end-plates increases the risk of cavitation inception at the end-plate root and tip, but it was also mentioned that the higher tip loading itself could stabilise the cavitation sheet in the presence of unavoidable cavitation.

Another reason for the CLT propeller's lack of popularity might be that it is a radically different design that shipowners might be reluctant to purchase. They are often not risk takers, and choose the conventional and well-proven design instead. The CLT propeller still seems like a promising design, with the relatively numerous full scale applications backing it up furthermore.

1.2.2 The 'Kappel' Propeller

The Kappel propeller was presented in 2001 after long development by the Danish engineer Jens Julius Kappel. It stands out from the CLT design in a number of ways. The blade tips are lifting, and curved gradually towards the suction side of the propeller with a large amount of skew. This means that the blades are non-planar lifting surfaces, differing substantially from most conventional propellers (Nielsen et al. 2012).

Figure 1.4: A 1:28 scale model of a Kappel Alpha 6.4 m diameter propeller (The Motorship 2012b).

The efficiency gains are claimed to be in the same vicinity as the CLT design – around 6 % (Nielsen et al. 2012). Reduced noise and vibration levels are additional listed benefits.

The Kappel design has not been around for as long as the CLT propellers, and are therefore not yet seen fitted to the same amount of vessels. The popularity is however on the rise. The first full scale test was done in the early 2000's on the 35 000 dwt tanker M/T 'Nordamerika' of Dampskibsselskabet Norden, right after it had undergone testing of a state of the art conventional propeller. Off the coast of Portugal, in similar calm weather conditions, a 4 % higher efficiency was achieved, as well as slightly lower pressure pulses (DTU 2014).

Over the years, passenger ferries, tankers, reefers, Ro-Pax ferries and even U-boats have been fitted with Kappel propellers (Nielsen et al. 2012). Also, eight new 58 500 dwt bulk carriers of Cyprus based Lemissoler Navigation, scheduled for delivery in 2015 and 2016, will be fitted with them.

A study from 2010 compared experimental and numerical results of a Kappel propeller ('KAP510') and a conventional propeller ('CV1700'), with special emphasis on scale effects and structural performance (Cheng et al. 2010). The Kappel propeller suffered from greater scale effects, and had a larger stress concentration at the blade tip. In full scale ($D = 6.6$ m), the blade tip deflection was 1.65 cm for the conventional propeller and 4.74 cm for the Kappel propeller. It was also found that the efficiency of the two propellers essentially was identical, contrary to other full scale test reports.

The Kappel design was acquired by MAN Diesel & Turbo in 2012, and is now an integrated part of their line of propulsion systems. Torben Johansen, the director of their Propeller & Aft Ship Department, says that they have difficulties convincing the shipowners of the design when it comes to scaling the model results. The effects of the Kappel propeller are not as evident in

full scale as in model scale, but they are certain that an increase in efficiency of at least 3 % can be achieved (Ingeniøren 2014).

It seems that the Kappel propellers are of a design that bears great potential, but with much ground to break when it comes to widespread use.

1.3 Outline of Thesis

The Kappel propeller is equipped with lifting blade tips, whereas the CLT propeller is not. The Kappel propeller is therefore closest to the thesis motivation of a lifting winglet – but there are a number of ways of conducting such a design. The blade tips of the Kappel propeller may resemble the 'raked wingtip' of some aircraft (e.g the Boeing 777 and 787), which has proven to be very effective on long distance flights. Another widely used wing tip device on aircraft is the 'blended winglet' – as seen on the Boeing 737, among others.

Both the Kappel and CLT propeller have been developed over several decades, which makes it unlikely that much contribution can be made to those designs in a Master's Thesis. A different approach is therefore chosen, with a design more analogous to the blended winglet.

Figure 1.5: The blended winglet of a Boeing 737-800 (Wikimedia Commons 2007).

The winglet equipped propellers had to be compared with a similar conventional propeller in order to quantitatively validate the performance. A propeller of the conventional type was therefore designed, and served as the reference case throughout the thesis. The winglet propellers, of which there were two variants, have the same main dimensions and operational conditions.

There are a lot of parameters in a propeller design phase that might be interesting to monitor and fine tune, but only the open water thrust, torque and efficiency results, as well as the cavitation performance and vorticity details are discussed. The reason for limiting the thesis to these parameters and propeller designs is simply because of practical concerns and the time scope. The results are presented in Chapter 6 and are thoroughly discussed in Chapter 7.

The lifting line computer program that was written for the sake of the propeller design will contribute to a significant part of the thesis.

Chapter 2

Theory

2.1 Linear Foil Theory

Propellers are lifting surfaces, where each blade are hydrofoils in circular motion. It is therefore important to have a good understanding of foil theory in order to design a functional propeller.

A hydrofoil experiencing an inflow will accelerate the water, and induce velocities both on the upper and lower surface. Common practice is to make a simplification, and assume these velocities to be equal in magnitude at each position on the upper and lower surfaces, but with different signs. This is shown in Figure 2.1 below.

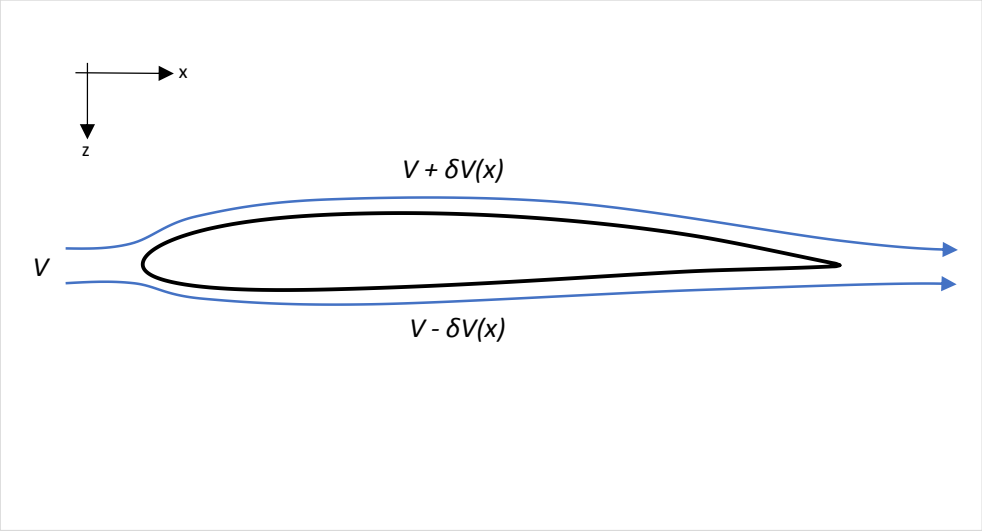

Figure 2.1: Overview of a foil profile, showing the inflow velocity V and induced velocity δV.

These velocities will lead to a pressure difference between the two surfaces, which can be found by Bernoulli's Principle:

$$\text{dynamic pressure} + \text{static pressure} + \text{local pressure} = \text{constant}$$

Choosing a point along a streamline, $\frac{1}{2}\rho V^2$ is the dynamic pressure, where ρ is the density of water and V is the fluid velocity. The static pressure consist of two parts, the hydrostatic pressure $\rho g z$ and the atmospheric pressure p_{atm}, where g is the acceleration of gravity and z is the submergence of the hydrofoil. The local pressure at the chosen point is only denoted as p. The sum of all these terms is constant along a streamline.

By choosing a point in front of the hydrofoil where the velocity is undisturbed, and then a point at the hydrofoil itself along the very same streamline, these two expressions equate to the same constant according to Bernoulli's Principle. The following two expressions are obtained, if this is done for both the upper and lower surfaces and any differences in submergence between the two streamlines are neglected:

$$\frac{1}{2}\rho V^2 + \rho g z + p_{\text{atm}} + p_0 = \frac{1}{2}\rho \left(V + \delta V(x)\right)^2 + p_{\text{atm}} + \rho g z + p_{\text{upper}} \tag{2.1}$$

$$\frac{1}{2}\rho V^2 + \rho g z + p_{\text{atm}} + p_0 = \frac{1}{2}\rho \left(V - \delta V(x)\right)^2 + p_{\text{atm}} + \rho g z + p_{\text{lower}} \tag{2.2}$$

p_0 is the local pressure at the point in front of the hydrofoil. It is obvious that the atmospheric pressure cancels out since it is constant and equal at every point below the water surface, and therefore will not affect the flow in any way. The hydrostatic pressure follows the same argument since any differences in submergence between the two streamlines are neglected.

The expressions for the pressures at the upper and lower surfaces of the hydrofoil can be found by reorganising Equations 2.1 and 2.2:

$$p_{\text{upper}}(x) = \frac{1}{2}\rho \left(V^2 - \left(V + \delta V(x)\right)^2\right) + p_0 \tag{2.3}$$

$$p_{\text{lower}}(x) = \frac{1}{2}\rho \left(V^2 - \left(V - \delta V(x)\right)^2\right) + p_0 \tag{2.4}$$

Even more interesting than the pressure is the hydrofoil's ability to create lift. Therefore, the pressure difference between the two surfaces must be found and integrated over the chord length to find the total lift. As Equations 2.3 and 2.4 show, p_{upper} has a lower value than p_{lower}. This means that the foil will lift upwards, so now defining this as the positive direction, p_{upper} may be subtracted from p_{lower} to obtain a positive pressure difference:

$$\Delta p(x) = p_{\text{lower}}(x) - p_{\text{upper}}(x) = \rho V \cdot 2\delta V(x) \tag{2.5}$$

The total lift can be found by integrating Equation 2.5 over the chord length c:

$$L = \rho V \int_c 2\delta V(x)\ \mathrm{d}x = \rho V \Gamma \tag{2.6}$$

This equation is called the Kutta-Joukowski theorem. It is now time to introduce the term *circulation*, where Γ as defined in Equation 2.6 is the total circulation around the foil profile. The circulation has dimension m^2/s, and physically represents the total lift contribution from the velocity jump $2\delta V(x)$ between the lower and upper surface at each chord-wise position. At each infinitesimal chord-wise section $\mathrm{d}x$, there is an induced velocity jump $2\delta V(x)$ which gives rise to an infinitesimal lift $\mathrm{d}L$. Γ is the total contribution to the lift of all these velocities.

The foil profiles used for conventional propeller design have low thickness ratios, and operate at very low angles of attack with low lift coefficients due to the cavitation criteria. These properties must be valid in order to use linear foil theory. Linear foil theory is great, much because of the highly desirable qualities it involves. The effects of thickness, camber and angle of attack can for example be handled individually, and then later be superimposed to get the combined result. Lift coefficients and angles of attack also scales linearly with each other, which is a very useful property.

2.2 Cavitation

Cavitation is the formation of vapour cavities in a liquid due to low pressure rather than high temperature. It can also be termed 'cold boiling', as the temperature is kept constant (possibly very low), and still the phase transition from liquid to vapour is present – contrary to the usual boiling of water. The thermodynamic processes are in both cases exactly similar. If the pressure falls below what is called the vapour pressure (around 1700 Pa for water at 15 °C), there is danger of cavitation – but in perfectly clean water, with no impurities whatsoever (e.g bubbles of air or minute amounts of vapour), there will not be any cavitation. Cavitation only occur when these nuclei become unstable and grow when subjected to lower pressure. This is a necessary condition, but cavitation is sure to evolve to some degree or another as there always are impurities in natural water.

The suction side of a hydrofoil or a propeller is prone to cavitate due to the low pressure. This is one of the key issues that drives the propeller design. Cavitation is an exclusively negative effect from a marine engineer's point of view, and life would be much better without it. A lot of research, time and money goes into avoiding cavitation for several reasons:

- The cavitation sheet on a propeller or hydrofoil alters the water flow, effectively changing the geometry and making it less efficient.
- Cavitation is noisy. The cavities may collapse and implode as they go from regions with low pressure to regions with higher pressure. This is a surprisingly noisy and violent transition from vapour to liquid that creates shock waves and very high local pressure peaks. The same sound may be heard when rapidly boiling water on a stove, as the temperature close to the bottom of the kettle is higher than further up. Cavities may form near the bottom, but as they are are convected upwards where the temperature is not high enough to sustain the vapour phase (or equivalently, the vapour pressure is lower than the ambient pressure) they will collapse and create shock waves which make the familiar sound. Later, as the temperature becomes more uniform, the sound disappear as the cavities are sustained all the way to the surface.
- Cavitation may also introduce unpleasant vibrations. This may be noticed if a large ferry reverses its propellers when for example docking – which may be slightly uncomfortable, but fortunately not for very long. The problem may be more severe if excessive cavitation occurs at normal operations. Also, if cavitation happens only at a certain point during the propeller revolution, fatigue of axles, bearings and other structural components may be an issue.
- Especially one form of cavities (bubble cavitation) erode the surface they collapse on. The shock waves literally dissolve the material, even if it is solid steel. There are instances of poorly designed propellers that have lost blades after a short amount of time because of bubble cavitation at the blade root. Structural integrity is compromised, and a blade could snap off.

These are all good reasons to avoid cavitation. Fortunately, a criteria for the cavitation inception can be developed. The microscopic structures of the cavitation nuclei are ignored in the following derivation, meaning that the cavity is modelled as a uniformly distributed pocket of water vapour. Surface forces acting on it are also ignored.

A hydrofoil with velocity V submerged at depth $z = h$ will serve as the starting point, as shown in Figure 2.2 below.

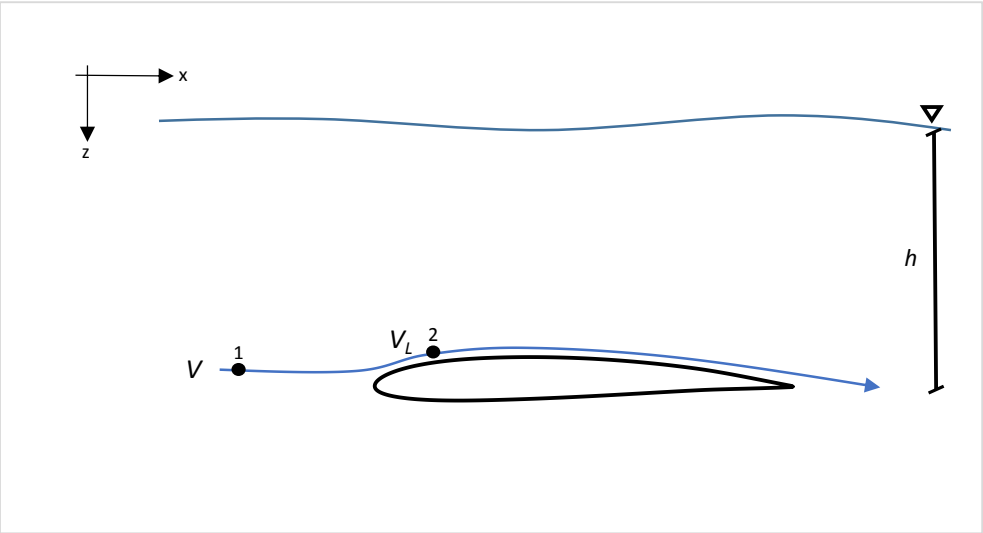

Figure 2.2: A hydrofoil with velocity V, submerged at depth $z = h$.

Point one is in the undisturbed free stream with velocity V, and point two is located at the hydrofoil, with local velocity V_L. If the streamline from point one to point two is followed, Bernoulli's Principle can be used to get an expression for the local pressure at point two (the difference in submergence is ignored):

$$\frac{1}{2}\rho V^2 + \rho g h + p_{\text{atm}} + p_1 = \frac{1}{2}\rho V_L^2 + \rho g h + p_{\text{atm}} + p_2 \implies p_2 = p_1 + \frac{1}{2}\rho V^2 \left(1 - \left(\frac{V_L}{V}\right)^2\right) \tag{2.7}$$

The pressure at point one is known to be $p_1 = \rho g h + p_{\text{atm}}$, and the desired situation is that the local pressure at point two is larger than the vapour pressure p_{v} in order to avoid cavitation:

$$p_2 = \rho g h + p_{\text{atm}} + \frac{1}{2}\rho V^2 \left(1 - \left(\frac{V_L}{V}\right)^2\right) > p_{\text{v}} \tag{2.8}$$

Reorganising gives

$$\left(1 - \left(\frac{V_L}{V}\right)^2\right) > \frac{p_{\text{v}} - p_{\text{atm}} - \rho g h}{\frac{1}{2}\rho V^2} \tag{2.9}$$

Multiplying by (-1) on both sides, the criteria for *no cavitation* is achieved as

$$\sigma > -C_p \tag{2.10}$$

where σ is the cavitation number, defined as

$$\sigma = \frac{p_{\text{atm}} - p_{\text{v}} + \rho g h}{\frac{1}{2}\rho V^2} \tag{2.11}$$

and $-C_p$ is the negative pressure coefficient defined as

$$-C_p = \left(\frac{V_L}{V}\right)^2 - 1 \tag{2.12}$$

The reason for the negative sign, which might seem like an unnecessary convention, is that the positive C_p is a non-dimensional number widely used in foil theory in general.

Equation 2.10 gives the criteria for no cavitation. Cavitation inception happens when $\sigma = -C_p$, so the flow is cavitating when $\sigma \leq -C_p$. Both σ and $-C_p$ are non-dimensional numbers. σ is independent of the foil, and since only the ratio of local velocity and inflow velocity is present in $-C_p$, the pressure coefficient is independent from everything but the foil geometry. The free stream velocity is irrelevant for $-C_p$, as the ratio between the two velocities is constant no matter what the free stream velocity is.

This is a simplified approach to the cavitation problem, and is not able to accurately predict cavitation inception. It is however a good starting point, and will tell if the flow is *likely* to cavitate or not. It is important to note that cavitation may occur at a higher σ than expected, for example due to turbulence (Steen 2014).

A worst case value of $-C_p$ for a symmetric NACA 0012 foil is 0.411 (Abbott, Doenhoff, and Stivers Jr. 1945). With $\rho = 1025$ kg/m^3, $p_{\text{atm}} = 101\,325$ Pa, $p_{\text{v}} = 1500$ Pa and $h = 1$ m, the limiting upper velocity for cavitation free operation for this hydrofoil is just above 44 knots. Cavitation becomes very difficult to avoid when the velocity increases above 50 knots. Water jets, or even super cavitating or surface piercing foil profiles must be used for propulsion in order to increase the velocity further.

2.3 NACA 16-series and the '$a = 0.8$' Camber Line

Foil profiles come in all kinds of variations, tailor made to different applications. Most of the early foil design was based on trial and error until the 'inverse design' approach came along, meaning that the designer then could choose the desired pressure distribution and compute the resulting geometry. This technique was utilised in the late 1930's to come up with the NACA 1-series. Of the 1-series, only the variant with minimum pressure located at 60 % of the chord length has seen widespread use, and consequently the 1-series is often referred to as the 16-series.

The 16-series has been particularly popular in aircraft and ship propeller design. This is mainly due to characteristics like low drag at high speed, and the fact that it avoids low pressure peaks (Scott 2001).

The thickness distribution is at first symmetrical, and must therefore be tilted at an angle of attack to produce lift. However, lift can also be produced by curving the profile. The flow direction is forced to change, which accelerates the fluid and creates a lift force according to Newton's 2$^{\text{nd}}$ law. This effect may be achieved by combining the thickness distribution with a camber line. There are a large number of different camber lines available. Particularly the $a = 0.8$ line is popular in propeller design. It has a constant circulation distribution up until 80 % of the chord length, before it eventually reduces linearly to zero at the trailing edge. The $a = 1.0$ camber line with constant circulation over the entire chord length is theoretically the best choice, but the $a = 0.8$ line is preferred due to risk of flow separation and reduced lift (Steen 2014). A camber line is usually designed with a lift coefficient equal to one, meaning that it has to be scaled linearly if other lift coefficients are desired.

For a given camber line, there exists an angle of attack which makes the foil section to lift *purely* by camber – called the *ideal* angle of attack, α_i. This means that the foil does not generate any lift due to an angle of attack, but only because of the applied camber. The lift coefficient is therefore equal to the lift coefficient of the camber line. Operating at an angle of attack will greatly increase the $\left(\frac{V_L}{V}\right)^2$ term in the pressure coefficient (Equation 2.12), meaning that hydrofoils and propellers are prone to experience severe cavitation if tilted to anything else than the ideal angle of attack. It is therefore highly desirable to operate at exactly the

ideal angle of attack. $\alpha_i = 1.54°$ for the $a = 0.8$ camber line (Abbott, Doenhoff, and Stivers Jr. 1945). The ideal angle of attack scales linearly with the lift coefficient.

The symmetric NACA 16-012 profile and the $a = 0.8$ camber line for $C_L = 1$ can be seen in Figure 2.3 below, together with the superimposed final foil profile.

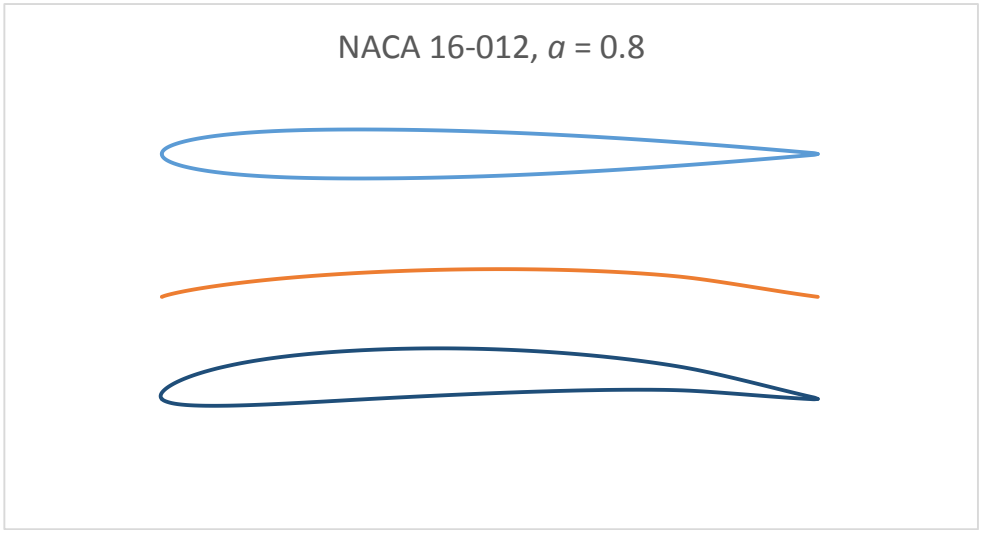

Figure 2.3: NACA 16-012 profile and the $a = 0.8$ camber line for $C_L = 1$. Superposition of the two yields the NACA 16-012, $a = 0.8$ foil profile.

2.4 Lifting Line Theory

2.4.1 Introduction

The lifting line theory is a two-dimensional approach to the propeller design, where the propeller is divided into a multiple of cross sections in the radial direction. A radial circulation distribution $\Gamma(r)$ is chosen, which essentially is a distribution of the lift along the propeller blade, as seen from Equation 2.6. A number of other key parameters must also be chosen, like for instance the radial chord length and thickness distributions, ship speed, propeller diameter and RPM. The total thrust can be found by integrating the sectional lift forces, and the total torque can be found by applying a suitable friction line. The induced axial and tangential velocities are also calculated, which leads to the design pitch distribution.

Lifting line theory works best on lifting surfaces with minor 3D effects, i.e long and slender high aspect ratio blades. This favours for example wind turbines which achieve great results by this approach, but propeller blades are not comparable. They are usually of low aspect ratio due to diameter restrictions and the cavitation criteria. Lifting line theory is however used in this application as well and yields fair results – but not to the same degree as for wind turbines.

2.4.2 Procedure

At first, the lifting line theory assumes an infinite number of blades, which obviously has to be corrected for. This can be done in a number of ways, i.e by Prandtl's tip loss factors, Goldstein factors or Lerbs' induction factors. This affects the induced velocities, and therefore also the pitch distribution.

The Biot-Savart law is an important equation in fluid mechanics. It is probably most famous for its applications in electromagnetics – more specifically the magnetic field induced by an electrical current – but the Biot-Savart law may also be used in hydrodynamics to express

the velocities induced by vortices. The vortex strength is set equal to the circulation at each radial position, so the induced tangential velocity may be expressed by Biot-Savart's law as

$$U_T = \frac{\Gamma}{2\pi r} \tag{2.13}$$

By geometric considerations of Figure 2.4 below, an expression for the induced axial velocity can be found, where V_0 is the ship speed, and w is the wake factor:

$$\frac{V_0\,(1-w) + \frac{U_A}{2}}{2\pi r n - \frac{U_T}{2}} = \frac{U_T}{U_A} \implies U_A^2 + U_A\,(2\,V_0(1-w)) - U_T(4\pi r n - U_T) = 0 \tag{2.14}$$

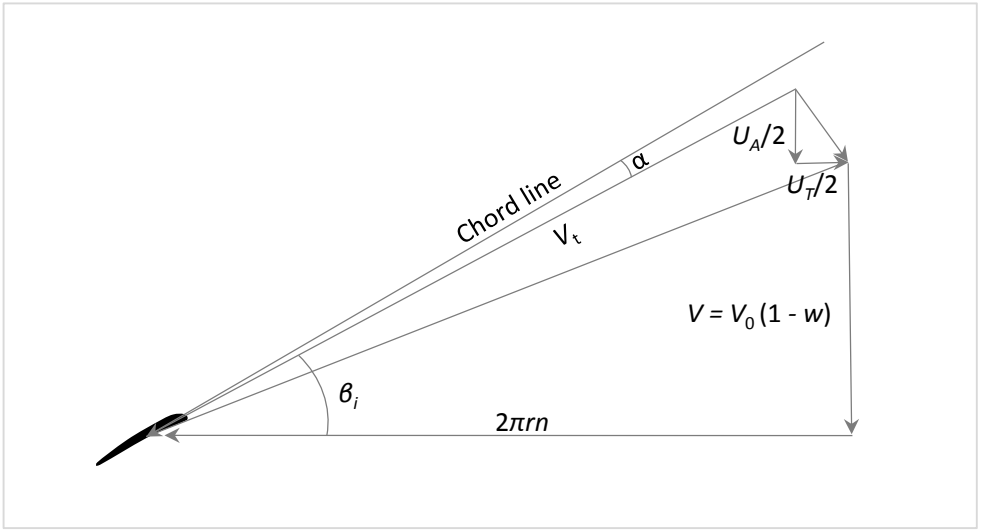

Figure 2.4: Velocities acting on a propeller blade section.

The induced axial velocity U_A is in the same direction as the inflow velocity V, therefore adding to the axial component of total velocity vector V_t. The induced tangential velocity U_T is in the opposite direction as the blade section velocity $2\pi rn$, therefore reducing the tangential component of V_t. The result of the induced velocities is an increase in the hydrodynamic angle of attack, β_i. There is also an induced drag component because the lift vector becomes slightly angled by the induced downwash. This drag component could be reduced by minimising the induced velocities.

The reason for the division by two in the induced velocities at the blade sections is that they at this position are half the value of the velocities further downstream.

Equation 2.14 is a quadratic equation on the common form $ax^2 + bx + c = 0$, with $x = U_A$ and coefficients $a = 1$, $b = 2\,V_0(1-w)$ and $c = -U_T(4\pi rn - U_T)$. Two solutions are therefore possible, but only the positive makes sense.

The solutions to U_A and U_T are at this stage usually called the *mean* induced velocities, as they are not yet corrected for a finite number of blades. From now on, the notation $U_{A,\,\mathrm{mean}}$ and $U_{T,\,\mathrm{mean}}$ will be used for the uncorrected velocities, and U_A and U_T will be used when they are corrected for a finite number of blades.

The mean hydrodynamic angle of attack may be expressed as follows:

$$\beta_{i,\,\mathrm{mean}} = \arctan\left(\frac{U_{T,\,\mathrm{mean}}}{U_{A,\,\mathrm{mean}}}\right) \tag{2.15}$$

As already mentioned, there are different methods of correcting for a finite number of blades. The one that gives the most accurate results for the lifting line method is Lerbs' induction factors, and is therefore the one that will be covered. Assuming that the circulation distribution $\Gamma(r)$ is for *each blade*, and not all in total (otherwise there must be an additional factor of $\frac{1}{\mathrm{Z}}$), the expressions for the induced velocities become

$$U_A(r_0) = \fint_{r_\mathrm{h}}^{R} \frac{i_a(r,\, r_0,\, \beta_i,\, \mathrm{Z})}{2\pi} \frac{\mathrm{d}\Gamma(r)}{\mathrm{d}r} \frac{1}{r_0 - r}\, \mathrm{d}r \tag{2.16}$$

$$U_T(r_0) = \fint_{r_\mathrm{h}}^{R} \frac{i_t(r,\, r_0,\, \beta_i,\, \mathrm{Z})}{2\pi} \frac{\mathrm{d}\Gamma(r)}{\mathrm{d}r} \frac{1}{r_0 - r}\, \mathrm{d}r \tag{2.17}$$

where r_0 is the fixed radial position of interest, r is the running variable, i_a and i_t are the axial and tangential induction factors respectively, Z is the number of blades, r_h is the hub radius and R is the propeller radius.

The dashed integral signs denote that these are *principal value* integrals, meaning that they have a singularity when $r = r_0$. Special care must be taken at this point, as the integral is undefined here and may shoot off to infinity.

The hydrodynamic angle of attack now has to be expressed in a new way, as the corrected induced velocities may change sign, and are therefore poorly defined by Equation 2.15:

$$\beta_i = \arctan\left(\frac{V_0(1-w) + \frac{U_A}{2}}{2\pi r n - \frac{U_T}{2}}\right) \tag{2.18}$$

The equations commonly used for the induction factors are as follows (van Oossanen 1974), where $\widetilde{\mathrm{R}} = r_0/r$:

$$\left.\begin{aligned} i_a &= (\widetilde{\mathrm{R}} - 1)\frac{\mathrm{ZA}}{\tan(\beta_i)} \\ i_t &= \left(1 - \frac{1}{\widetilde{\mathrm{R}}}\right)\mathrm{Z}\,(1 + \mathrm{A}) \end{aligned}\right\} \quad \text{for } \widetilde{\mathrm{R}} > 1 \tag{2.19}$$

$$\left.\begin{aligned} i_a &= \cos(\beta_i) \\ i_t &= \sin(\beta_i) \end{aligned}\right\} \quad \text{for } \widetilde{\mathrm{R}} = 1 \tag{2.20}$$

$$\left.\begin{aligned} i_a &= (1 - \widetilde{\mathrm{R}})\frac{\mathrm{Z}\,(1 + \mathrm{B})}{\tan(\beta_i)} \\ i_t &= \left(\frac{1}{\widetilde{\mathrm{R}}} - 1\right)\mathrm{ZB} \end{aligned}\right\} \quad \text{for } \widetilde{\mathrm{R}} < 1 \tag{2.21}$$

where

$$\mathrm{A} = \mathrm{f}\left[\frac{1}{\mathrm{u} - 1} - \frac{\mathrm{g}}{24\mathrm{Z}} \ln\left(\frac{\mathrm{u}}{\mathrm{u} - 1}\right)\right]$$

$$\mathrm{B} = \mathrm{f}\left[\frac{\mathrm{u}}{1 - \mathrm{u}} - \frac{\mathrm{g}}{24\mathrm{Z}} \ln\left(\frac{1}{1 - \mathrm{u}}\right)\right]$$

$$\mathrm{f} = \sin^{-\frac{1}{2}}(\beta_i)\, \mathrm{p}^{-\frac{1}{4}}$$

$$u = \exp\left[Z\left(\ln\left[(p^{-\frac{1}{2}} - 1)\left(\sin^{-1}(\beta_i) - 1\right)^{-1}\frac{1}{\widetilde{R}}\right] + p^{\frac{1}{2}} - \sin^{-1}(\beta_i)\right)\right]$$

$$g = \sin^3(\beta_i)\left[2 + \frac{9}{\tan^2(\beta_i)}\right] + (3p - 5)\,p^{-\frac{3}{2}}$$

$$p = 1 + \left[\frac{\widetilde{R}}{\tan(\beta_i)}\right]^2$$

Figure 2.5 and 2.6 below show the induction factors for a 5-bladed propeller and a selection of hydrodynamic angles of attack – $\beta_i = 25°$, $50°$ and $75°$:

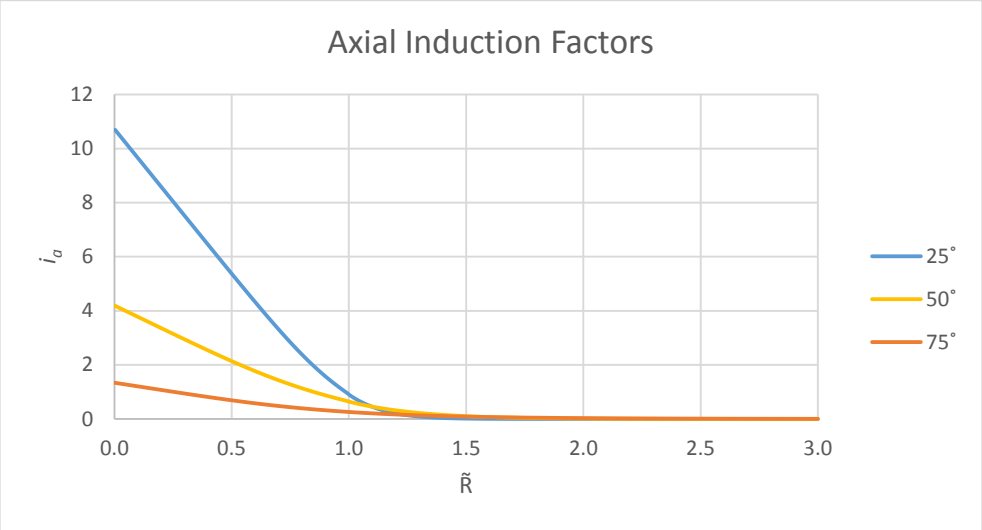

Figure 2.5: Axial induction factors for Z = 5. $\beta_i = 25°$, $50°$ and $75°$.

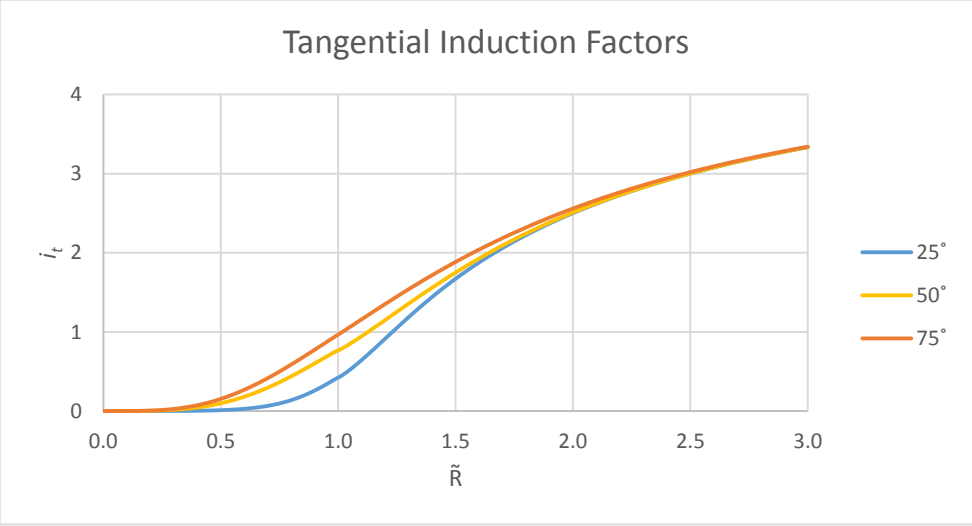

Figure 2.6: Tangential induction factors for Z = 5. $\beta_i = 25°$, $50°$ and $75°$.

The induction factors i_a and i_t depends on the hydrodynamic angle of attack β_i, which again depends on the induced velocities that are to be calculated. The problem is therefore implicit, and an iteration algorithm has to be applied in order to get a solution. A first guess on the induced velocities must be made, which leads to an initial hydrodynamic angle of attack. A

good start is to use the mean induced velocities and the mean hydrodynamic angle of attack as defined by Equations 2.13 – 2.15, but any start value could in principle be used.

The solution strategy becomes as follows:

For each r_0 from r_h to R:

- Solve Equations 2.16 and 2.17:
  - Guess $U_A(r_0)$, $U_T(r_0)$ and $\beta_i(r_0)$
  - For each r from r_h to R:
    - Calculate $\widetilde{\mathrm{R}} = r_0/r$
    - Calculate $i_a(\widetilde{\mathrm{R}}, \beta_i, \mathrm{Z})$ and $i_t(\widetilde{\mathrm{R}}, \beta_i, \mathrm{Z})$ from Equations 2.19 – 2.21
    - Multiply the induction factors by the derivative of the circulation distribution and $\frac{1}{2\pi}\frac{1}{r_0 - r}$
  - Calculate $U_A(r_0)$ and $U_T(r_0)$ by integrating from $r = r_\mathrm{h}$ to $r = R$
  - Calculate β_i from Equation 2.18
- Check for convergence of $U_A(r_0)$ and $U_T(r_0)$. The entire procedure must be repeated for the current lifting line if there is not yet any convergence, now by using the calculated values as (hopefully) improved guesses. The next lifting line can be calculated if there is convergence.

The next steps to be done in order to get an estimation of the thrust and torque of the propeller are as follows (most variables are functions of the radial position r, but this is not typed explicitly in order to avoid excessive clutter in the equations):

- Calculate the total velocity at each blade section:

$$V_\mathrm{t} = \sqrt{\left(V_0 + \frac{U_A}{2}\right)^2 + \left(2\pi r n - \frac{U_T}{2}\right)^2} \tag{2.22}$$

- Calculate the lift of each section:

$$\mathrm{d}L = \rho V_\mathrm{t} \Gamma \tag{2.23}$$

- Calculate the lift coefficient of each section:

$$C_L = \frac{\mathrm{d}L}{\frac{1}{2}\rho V_\mathrm{t}\, c} \tag{2.24}$$

- Calculate the friction coefficient of each section (by using the ITTC '57 friction line):

$$C_F = \frac{0.075}{\left[\log(\mathrm{Re}) - 2\right]^2} \tag{2.25}$$

  where Re is the Reynolds number, defined as follows, with ν as the kinematic viscosity:

$$\mathrm{Re} = \frac{V_\mathrm{t}\, c}{\nu}$$

- Calculate the drag coefficient of each section:

$$C_D = 2C_F\left(1 + 2\frac{t}{c}\right) \tag{2.26}$$

- Calculate the drag of each section:

$$\mathrm{d}D = \frac{1}{2}\rho V_{\mathrm{t}}^2 C_D \, c \tag{2.27}$$

- Calculate the thrust of each section:

$$\mathrm{d}T = \rho\Gamma\left(2\pi r n - \frac{U_T}{2}\right) - \mathrm{d}D\sin(\beta_i) \tag{2.28}$$

- Calculate the torque of each section:

$$\mathrm{d}Q = \rho\Gamma\left(V_0(1-w) + \frac{U_A}{2}\right) r - \mathrm{d}D\cos(\beta_i)\, r \tag{2.29}$$

- Integrate to find the total thrust and torque:

$$T = \int_{r_{\mathrm{h}}}^{R} \mathrm{d}T \, \mathrm{d}r \tag{2.30}$$

$$Q = \int_{r_{\mathrm{h}}}^{R} \mathrm{d}Q \, \mathrm{d}r \tag{2.31}$$

- The total efficiency of the propeller can now be found:

$$\eta = \frac{VT}{2\pi n Q} \tag{2.32}$$

VT is the total thrust of the propeller times the ship speed, which is the usable power. $2\pi nQ$ is the angular speed of the propeller times the total torque, which is the total power absorbed by the propeller. The ratio is the efficiency, which is always lower than 100 %.

'Foil and Propeller Theory' by Professor Sverre Steen (Steen 2014) has been used extensively for the lifting line implementation.

2.4.3 Cavitation Implementation

Cavitation may be introduced in the lifting line procedure. The cavitation number σ must be calculated and compared with the pressure coefficient $-C_p$ at each blade section. With h set to the draught of the propeller hub, and V_{t} given by Equation 2.22, the cavitation number becomes

$$\sigma(r) = \frac{p_{\mathrm{atm}} - p_{\mathrm{v}} + \rho g(h-r)}{\frac{1}{2}\rho V_{\mathrm{t}}^2} \tag{2.33}$$

The maximum local velocity at the blade suction side must be expressed in order to find the correct $-C_p$ of each blade section. This is a combination of both thickness and camber contributions, and can be superimposed when linear foil theory is used. These data are tabulated and can be scaled linearly with the thickness to chord ratio and lift coefficient. The velocity due to thickness is

$$\left(1 + \frac{v}{V}\right) = \left[\left(\frac{v}{V}\right)_{t/c=0.12} - 1\right]\frac{t/c}{0.12} + 1 \tag{2.34}$$

where the value of $\left(\frac{v}{V}\right)_{t/c=0.12}$ is taken from tables, and serves as the reference thickness for scaling of the velocities. Another thickness ratio than 0.12 could just as well be used. Only the velocity increase contributed by the thickness *on top of* the free stream velocity should be taken into account when scaling, which is the reason why there is a -1 inside the brackets of Equation 2.34 (and the reason why it is added once again after the scaling is done). The free stream velocity should of course not be scaled by any thickness.

The velocity due to camber is

$$\frac{\Delta v}{V} = C_L \left(\frac{\Delta v}{V}\right)_{C_L=1} \tag{2.35}$$

where $\left(\frac{\Delta v}{V}\right)_{C_L=1}$ is taken from tables for the desired camber distributions. Only the increase in velocity due to the camber is tabulated, meaning that they can be scaled directly without subtracting any free stream velocity. This is different from the tabulated thickness velocities described above.

The ratio of local and total free stream velocity then becomes

$$\frac{V_L}{V_\mathrm{t}} = \left(1 + \frac{v}{V}\right) + \frac{\Delta v}{V} \tag{2.36}$$

and the pressure coefficient becomes

$$-C_p = \left(\frac{V_L}{V_\mathrm{t}}\right)^2 - 1 \tag{2.37}$$

Cavitation is avoided as long as $\sigma(r) > -C_p$ at each section.

As can be seen from Equation 2.22, the total velocity at each section increases linearly with the radial position. $\sigma(r)$ is inversely proportional with V_t^2, which implies that $\sigma(r)$ is inversely proportional with r^2. In addition, there is a linear factor of $-r$ in the numerator, which further increases the inversely proportional trend. The cavitation number decreases rapidly with the radius, therefore making it more and more difficult to avoid cavitation as we proceed towards the tip of the propeller.

2.5 Open Water Tests

Propellers are usually going through two kinds of tests – a propulsion test done in a towing tank, and an open water test done either in a cavitation tunnel or in a towing tank. The propulsion test is done together with the correct ship model to check for propeller-hull interactions and to check how the ship performs with its propeller. Only the open water test will be discussed here, as this is the one relevant for this thesis.

The open water test is, as the name suggest, done in open water, implying that there is no disturbing ship hull present. This means that the best possible operating conditions for the propeller are achieved, and that the optimum performance can be examined. A cavitation tunnel is especially suitable for such an experiment, with good control of the water inflow and high quality measuring equipment usually already installed.

A set of dimensionless coefficients are necessary to present the data in a standardized and comparable way. The *advance number* is first introduced, which provides a quantity describing the loading of the propeller:

$$J = \frac{V_A}{nD} \tag{2.38}$$

where V_A is the advance velocity – the speed at which the propeller advances forward (usually the ship speed itself) – n is the propeller speed and D is the propeller diameter. Physically, the number may be understood as a ratio of the ship speed relative to the speed of the propeller (actually the number of $\frac{1}{\pi}$ circumferences the propeller tip manages to rotate every second, since πD equals one complete circumference). An alternative, and maybe more intuitive way to understand the advance number is by dividing with n in both the numerator and denominator. J is then the distance the propeller moves forward in one revolution relative to its diameter.

A large J implies that V_A is much larger than nD, meaning that the propeller speed is low compared to the ship speed. This can be understood as a lightly loaded propeller, as it moves forward quite easily. The opposite case where J is low can be understood as a heavily loaded propeller. The propeller must work hard in order to advance forward. This is particularly the case for anchor handlers or tugs, where the propellers provide a lot of thrust, but hardly move forward at all.

The thrust and torque are the two key parameters needed to describe a propeller's performance. The propeller efficiency can be deduced from these two parameters, as already seen in Equation 2.32. Physically, the thrust is the forward directed force, and the torque is how 'heavy' the propeller is to turn around. The water will resist to move, and this is partly felt as a torque on the propeller.

The thrust and torque are made non-dimensional, and expressed in this way:

$$K_T = \frac{T}{\rho n^2 D^4} \tag{2.39}$$

$$K_Q = \frac{Q}{\rho n^2 D^5} \tag{2.40}$$

where K_T and K_Q are the thrust and torque coefficients, respectively.

The following expression for the efficiency can be found by expressing T and Q from Equations 2.39 and 2.40, and substituting them into Equation 2.32 – where the ship speed V has been used in the advance number J:

$$\eta = \frac{J}{2\pi}\frac{K_T}{K_Q} \tag{2.41}$$

Equations 2.32 and 2.41 express the exact same quantity – only with different parameters. Equation 2.41 is usually preferred for open water tests.

The results from an open water test are presented in an 'open water diagram', where K_T, $10K_Q$ and η are plotted for a range of advance numbers J. The advance number is usually changed by varying the advance velocity (inflow velocity in a cavitation tunnel or carriage speed in a towing tank) and keeping n constant.

The reason for plotting $10K_Q$ rather than K_Q is just to make the diagram more readable, by better matching the orders of magnitude.

It is referred to Chapter 6.1.1 for examples of what open water diagrams look like.

Chapter 3

Lifting Line Computer Program

3.1 Introduction

It was difficult to find freely available 3D models of propellers on the Internet. An important part of the idea behind winglet fitted propellers is the ability to load the propeller tip more than conventional propellers. This served as a motivation for writing a computer program for propeller design. If a conventional propeller was found on the Internet, it would most probably have a circulation distribution going to zero at the propeller tip, and the fitting of a winglet would not necessarily yield any better thrust or efficiency. It proved very useful to have the ability to freely choose an arbitrary circulation distribution, thickness and chord distribution, propeller diameter, RPM as well as ship speed – and have the resulting pitch distribution and correctly scaled foil sections calculated. To have complete control of the propeller design was valuable, and it also goes without saying that writing such a program gave a lot of insight and knowledge about the propeller design process.

The program was based on the lifting line theory with Lerbs' induction factors as described in Chapter 2.4. It was written in MATLAB, and consists of three functions:

- **`lifting_line_induction.m`**
  This is the main body of the program, controlling the calculations, as well as all inputs and outputs.
- **`induction_factors.m`**
  Calculates the induction factors.
- **`NACA_16_a08.m`**
  Scales and prints NACA 16-series foil profiles with the $a = 0.8$ mean line, according to the thickness, chord length and lift coefficient.

The source code for all functions can be found in Appendix A.1.

3.2 Review of the Program

The review of the program has been broken down into sections that cover the main topics and how they have been handled in the code. All functions are explained, but the emphasis will be on `lifting_line_induction.m`, which is the main part of the program. It will be mentioned explicitly in the text when a certain part of the program is handled by either `induction_factors.m` or `NACA_16_a08.m`.

3.2.1 Main Inputs

The main input parameters to `lifting_line_induction.m` are as follows:

- Number of lifting lines
- Propeller diameter
- Propeller RPM
- Number of propeller blades
- Ship speed in knots
- Water density
- Kinematic viscosity of water
- Draught of the propeller hub
- Number of propeller sections to print
- Yield stress of the propeller material
- A Scale factor for the circulation distribution
- A convergence criteria for the induction factor iteration loop
- An option for 3D correction
- A number of plot controls, and an option for printing the run-time outputs to a text file

Some of the distributions are handled internally in the function. The circulation distribution is for example based on a sixth order polynomial with a linear scale factor that can be given as input, and the thickness distribution follows the Wageningen B-Series thickness. The program is written to handle an arbitrary radial wake distribution, but it is set to zero as standard.

Other distributions must be entered inside the code if changes are desired. This is just to reduce the number of input parameters to the function.

3.2.2 Calculation of the Induced Velocities

The chord distribution is interpolated after the initialising of all internal variables, and the circulation and thickness distributions are computed. The differentiation of the circulation distribution is done numerically, with a second order accurate central differencing scheme at all points except the end points, where first order accurate forward and backward schemes are used.

The main loop is then entered, where the solving of Equations 2.16 and 2.17 for every lifting line takes place. The numerical integration is done in a 'brute force' manner – that is, hoping for convergence by simply skipping the singular point altogether, and summing up a large number of small rectangles of the integrand. This requires a fine resolution of integration points, but nothing more than what an average laptop can handle in a few minutes. This is hard coded to be the same as the number of lifting lines – N lifting lines will also give N integration points.

The integrand may look like this:

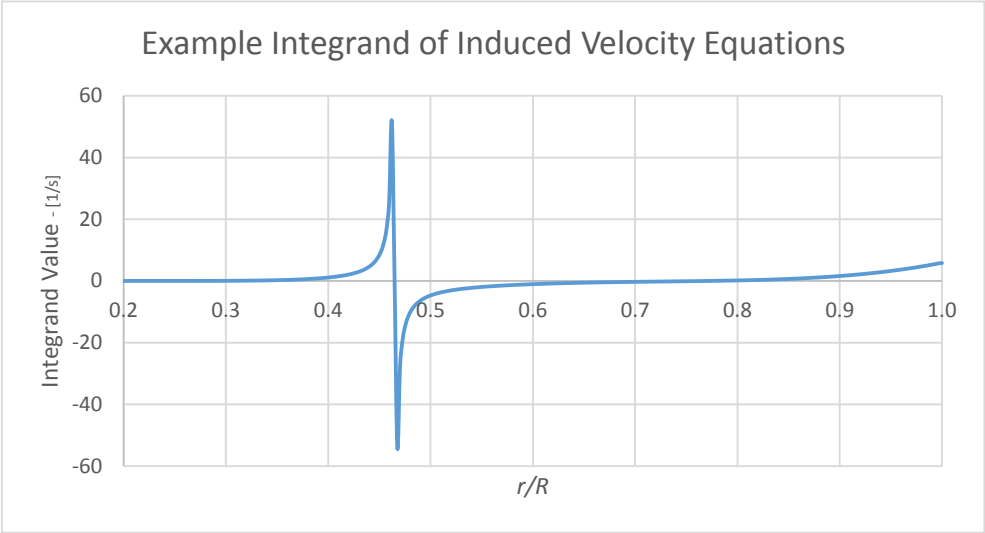

Figure 3.1: What the integrand of Equations 2.16 and 2.17 might look like (the singularity is clipped).

The integral should converge by approaching the singularity as close as possible from both sides, and including everything except the infinite value. The way this is handled in the loop is by skipping the index where $r = r_0$, and summing up everything else. Residuals are calculated after the induced velocities are computed, as well as a new value of the hydrodynamic angle of attack. All this happens inside a 'while loop', which runs as long as the residuals are higher than the convergence criteria, or the maximum number of iterations per lifting line is not exceeded (set to 100 as standard). The induced velocities usually converge in less than ten iterations to a final residual criteria of maximum 10^{-9}.

The function `induction_factors.m` handles the calculation of the induction factors, and is called at this stage of the program. It is not much more to say about this function other than that it follows Equations 2.19 – 2.21 exactly as they are presented. The inputs to the function are as follows:

- The ratio of the fixed radial position and running radial position – that is $\widetilde{\mathrm{R}}$
- The hydrodynamic angle of attack
- The number of blades

There has to be calculated a new set of induction factors for each radial position at each and every lifting line. In addition, the iteration loop repeats this process, which means that the function is called a large amount of times. For a final residual criteria of 10^{-9}, the average number of iterations per lifting line is a little less than 8.5. This means that the function is called approximately $8.5 \cdot N^2$ times. The total number becomes about 8.5 million for $N = 1000$, which was the number used for the propeller design.

The whole process of integrating Equations 2.16 and 2.17 could be done more elegant, e.g by a clever change of variables and a Fourier series expansion of both the circulation distribution and induction factors (van Oossanen 1974). The singularity then disappears altogether, and the equations may be integrated with very good accuracy using just a few integration points. However, the mathematical complexity of this approach would require a lot of effort, and it was not investigated further as the simpler method converged nicely.

The Concept of Residuals

Suppose that the the equation $f(x) = y$ is to be solved – that is finding the x that gives y. A guess of the solution could be made, for example x_0. The *error* is $\varepsilon = x_0 - x$, and assuming that the answer y is known, as is the case for an explicit problem, the *residual* is $r = f(x_0) - f(x) = y_0 - y$. Finding the error involves knowing the correct solution x, which in general could be very difficult to find, but finding the residual does not involve knowing the correct solution – only the difference of the computed value and the desired one. The answer is good if the difference is close to zero, implying that the solution is good – that is $x_0 \approx x$. The solution is certainly useless if the residual is large – that is $x_0 \neq x$, and a new guess must be made. The residual is therefore a good representation of the solution's validity, but it must not be mistaken as the error.

Suppose that even y is unknown, as is the case for an implicit problem, where the solution x itself depends on the answer y – that is $x = x(y)$ and $f(x(y)) = y$. The best thing to do is start guessing, and check for convergence after some trials. The residual then becomes the difference of the sequence of iterations, that is $r_1 = y_1 - y_0$, $r_2 = y_2 - y_1$ and so forth, where the current answer is compared with the previous value of y. If the sequence of residuals are diminishing, both x and y are converging, and the solution is approaching. Note that the first residual can be computed only after two iterations are completed, otherwise a value of y_0 must be guessed as well.

The scary part of this technique is that it is not known which solution is the correct one. There may be several solutions to the equation, meaning that there is a risk for the iterative sequence to converge nicely, but to the wrong solution. However, this does not necessarily have to be a big issue if one has good understanding of the problem and qualified guesses that are in the near vicinity of the expected values.

The problem is implicit in the case of the induction factor based lifting line method, and needs treatment of the type described above, where $f(x(y))$ and y can be seen as the right and left hand side respectively of Equations 2.16 and 2.17. The meaning of x is the correct solution, for example the correct β_i, that must be found in order to calculate the correct values of y – that is U_A and U_T. The hydrodynamic angle of attack β_i is a function of U_A and U_T, so $x = x(y)$.

The mean values of the induced axial and tangential velocities are used as first guesses for the input on the right hand side of the equations. These are good guesses which the corrected velocities should not differ too much from, meaning that the converged values are believed to be correct if they are reasonably close.

3.2.3 Cavitation Implementation

The cavitation check is done according to the procedure presented in Chapter 2.4.3. The cavitation number and pressure coefficient are calculated at each radial position and plotted in the same figure to see if the criteria is fulfilled. The submergence of the propeller hub is needed for this, so the cavitation check is skipped if a draught of zero is chosen. Only the worst case position of the blade is checked, which is when it points straight up towards the free surface.

The worst case value of $\left(\frac{v}{V}\right)_{t/c=0.12}$ is 1.137 for the NACA 16-012 profile, and the worst case value of $\left(\frac{\Delta v}{V}\right)_{C_L=1}$ is 0.278 for the $a = 0.8$ camber line (Abbott, Doenhoff, and Stivers Jr. 1945).

3.2.4 Structural Design

The structural integrity of the propeller is very important. It experiences heavy loading, and must therefore be properly designed so the internal stresses are not too high. A simple procedure to check for the capacity in bending moment failure was written. It is based on the familiar formula

$$\sigma = \frac{M}{I} y \tag{3.1}$$

where σ is the bending stress, M is the bending moment, I is the cross section's second moment of area, and y is the distance to the axis of bending. M is found at each blade section by integrating the thrust loads that contribute to the moment at that section – i.e all blade sections outside (larger radial coordinate) of the one in interest.

The second moment of area is an important parameter, and is given by the formula

$$I = \iint_A y^2 \, \mathrm{d}A \tag{3.2}$$

for a rotation about the x-axis. Physically, I is a measure of a cross sections resistance against rotation.

For a rectangle, with center at the origin, width b along the x-axis and height h along the y-axis, the integral can be expressed in this way:

$$I = \int_{-b/2}^{b/2} \int_{-h/2}^{h/2} y^2 \, \mathrm{d}y \, \mathrm{d}x = \frac{1}{12} b h^3 \tag{3.3}$$

I has dimension m^4, and a small change in h will make a significant contribution to the final value.

The foil sections of a propeller change along the span, meaning that I changes as well. Thickness and chord lengths change a lot, but the *geometry* itself does not change that much, even though there is some camber that makes this assumption not entirely valid. A NACA 16-012 profile, with no camber and a chord length of 1 m was used to base the second moment of area on. This value of I could then be scaled to get quite accurate approximations for different similar cross sections. A simple MATLAB function, `second_area_moment.m`, was written to calculate I for the standard cross section. The code is based on Equation 3.3 – so a summation of many small rectangles of the foil cross section is done. The resulting value was $I = 7.0994865 \cdot 10^{-5}$ m^4.

At first, it is natural to think that I scales with the thickness to the third power, and the chord length to the first power. It does scale with the thickness to the third power, but as the thickness is given in terms of the chord length, it actually scales with the chord length to the fourth power as well. The logic behind this is that a doubling of the chord length increases I by a factor of two, but as the thickness is given by the t/c-ratio, the thickness also doubles – which increases I eightfold. The total increase is in this case therefore sixteen – the multiplication factor raised to the fourth power, 2^4 – which means that I scales as c^4. An increase in the thickness ratio t/c alone does not affect the chord length, implying that I scales as t^3. A doubling of both t and c would then lead to a multiplication of the original I by a factor $2^3 \cdot 2^4 = 2^7 = 128$. This demonstrates the profound effect a change of the cross section has on the ability to resist rotation – or the ability to absorb stresses. A large second moment of area results in low stresses, as seen in Equation 3.1.

y is in the case of Equation 3.1 set equal to $t/2$. The standard NACA 16-012 cross section has dimensions $c = 1$ m and $t = 0.12$ m, which means that scaling the thickness involves

dividing by 0.12 before multiplying by the new thickness. This can be included directly into the scaling of the second moment of area as $I = i\left(\frac{t}{0.12}\right)^3 c^4$, where i is the second moment of area of the standard cross section. The chord length is already at unity, which implies that the new chord length may be used without modifications. Substituting this value of I, and the yield stress $\sigma = \sigma_y$ as well as $y = t/2$ into Equation 3.1, it is possible to express a minimal thickness required to avoid bending moment blade failure:

$$t_{\min} = \sqrt{\frac{27}{31250}\frac{M}{i\,c^4\,\sigma_y}} \tag{3.4}$$

All units are SI, which means that the dimension of t is metres. To avoid blade failure, $t > t_{\min}$.

It is crucial to highlight that this formula *only* takes into account the bending moment contribution. This may be the most important one, but there are others as well, where especially fatigue failure is vital to look out for. In addition, the propeller may experience significantly higher loads at operational conditions other than the optimum. The thickness implied by Equation 3.4 should therefore be regarded as the absolute lower limit, which most probably is a bit too low. Because of this, the thickness distribution by Wageningen (Steen 2014) has also been included as a conservative upper value. This is a linear thickness distribution for use with the Wageningen B-series propellers, so a different one should probably be considered if the type of propeller differs much from this series in terms of loading or geometry.

3.2.5 Correction for 3D Effects

One of the input parameters to the program is the number of sections that should be printed to text files. If for example ten are selected, ten equally spaced radial positions between the hub radius and tip radius are chosen. The program searches for the sections which are closest and stores the indices, so that all necessary data from the different distributions may be fed into the function handling scaling and printing of the sections. The 3D correction is done at this point. Some corrections must be made since the lifting line procedure in its nature is two-dimensional, and cannot account for the helical motion of a three-dimensional propeller. There are several different ways of doing such a correction, but most of them are based on a large amount of three-dimensional lifting surface simulations with different number of blades, Expanded Area Ratios and pitch distributions. Finding the right correction factors in a general lifting line program would require a very large database of correction factors and a clever interpolation algorithm across several parameters. This is a cumbersome process, which led to a compromise and the use of the following set of equations instead (Steen 2014):

- The correction factor for camber:

$$k_c = 1.6946 + 0.5048\left(\frac{r}{R}\right) - 4.0012\left(\frac{r}{R}\right)^2 + 4.3283\left(\frac{r}{R}\right)^3 \tag{3.5}$$

- The correction factor for angle of attack:

$$k_a = 1 + 1.46\left(\frac{r}{R}\right)^3 \tag{3.6}$$

- The correction factor for thickness effects:

$$k_t = 2.5\,\frac{t}{r}\frac{c}{D}\cos(\beta_i) \tag{3.7}$$

These factors contribute mostly to an increase in the camber and angle of attack. The factors are used as follows:

- Corrected total camber:
$$\left(\frac{f}{c}\right)_{\text{total}} = k_c \cdot C_L \cdot \left(\frac{f}{c}\right)_{\text{a}=0.8} \tag{3.8}$$
where $\left(\frac{f}{c}\right)$ is the maximum camber ratio.

- Corrected ideal angle of attack:
$$\alpha_{i,\,3\text{D}} = k_a \cdot 1.54 \cdot C_L \tag{3.9}$$

- Corrected angle of attack due to thickness effects:
$$\alpha_t = k_t \, \frac{t}{c} \tag{3.10}$$

This gives a corrected angle of attack:

$$\alpha_{\text{corrected}} = \alpha_{i,\,3\text{D}} + \alpha_t \tag{3.11}$$

The correction factors are calculated at the end of `lifting_line_induction.m`, and then used as input to `NACA_16_a08.m` which deals with scaling of the foil profiles and the final correction.

3.2.6 Scaling and Printing of Propeller Foil Sections

The inputs to `NACA_16_a08.m` are given for each foil section that should be printed, and are as follows:

- The section number of the foil
- Radial position
- Lift coefficient
- Absolute thickness
- Chord length
- The hydrodynamic angle of attack
- 3D correction factors
- Propeller radius
- An option for centring the foil coordinates around $x = 0$
- An option for plotting the resulting profile

The standard NACA 16-012 foil section is again used as the reference. A foil geometry scales very close to linearly with the thickness and chord length, meaning that it is unnecessary to calculate new coordinates for each unique foil profile. The coordinates for the 16-012 profile was obtained by the aid of a FORTRAN program called 'NACA456' (PDAS 2001), published by Public Domain Aeronautical Software and written by Ralph L. Carmichael, based on previous programs developed by NASA. This produced a high quality dense spacing of the coordinates, leading to a more accurate representation of the profile (and eventually propeller surface) compared to the tabulated coordinates produced by (Abbott, Doenhoff, and Stivers Jr. 1945). The $a = 0.8$ camber line is taken directly from Abbott et al., so the coordinate spacing is therefore quite coarse, but this is not a problem as there are no strong variations in the camber line geometry. The camber line is interpolated onto the same x-coordinates as the thickness distribution, making them identical, so that the transformation of the thickness distribution can be done. This happens according to the following formulas (Abbott, Doenhoff, and Stivers Jr. 1945):

$$x_u = x_t - y_t \sin(\vartheta) \tag{3.12}$$

$$x_l = x_t + y_t \sin(\vartheta) \tag{3.13}$$

$$y_u = y_c + y_t \cos(\vartheta) \tag{3.14}$$

$$y_l = y_c - y_t \cos(\vartheta) \tag{3.15}$$

where x_u, y_u and x_l, y_l are the upper and lower side x- and y-coordinates respectively. x_t, y_t and x_c, y_c are the x- and y-coordinates of the thickness and camber distribution respectively. ϑ is given by the following expression:

$$\vartheta = \arctan\left(\frac{\mathrm{d}y_c}{\mathrm{d}x_t}\right) \tag{3.16}$$

This implies that also the derivative of y_c must be mapped onto the same x-axis, i.e x_t.

`NACA_16_a08.m` then scales the camber line to the correct lift coefficient, as well as the thickness and chord length to the desired values, before writing the final coordinates to a text file. This is done in a right handed circular direction – that is, starting from the leading edge and writing the coordinates of the upper side all the way to the trailing edge, before continuing writing the lower side coordinates from the trailing edge and back to the leading edge. This is a common way of presenting foil-coordinates. In addition, other useful data is written to the text file, like for example the radial position and hydrodynamic angle of attack and ideal angle of attack. This is to make the 3D CAD-modelling as efficient as possible.

Finally, `lifting_line_induction.m` calculates the total thrust and torque, as well as the efficiency, according to the procedure outlined by Equations 2.22 – 2.32. The Expanded Area Ratio (EAR) is also calculated, as well as the pitch ratio (P/D) distribution.

Run-time outputs, like final residuals of the lifting lines, a summary of the final design or warning messages to be aware of, are written to the MATLAB window upon execution of the program. These can also be printed to a text file if desired. Examples of the run-time output can be found in Appendix A.2.

Chapter 4

Design

4.1 Reference Ship

A realistic propeller loading for a given diameter was desired instead of just choosing some random value. Quite accurate data for a real ship is needed for that purpose, and this is usually difficult to get hold of. Luckily, there are some benchmark models with lots of test data available, which are often used to check CFD codes and towing tank measuring equipment. The 'KRISO Container Ship' (Korea Research Institute for Ships and Ocean Engineering) was chosen, which is a 230 m long 3600 TEU container vessel with a cruise speed of 24 knots ($F_n = 0.26$). The propeller has diameter 7.9 m, five blades, and an expanded area ratio (EAR) of 0.8. All the main particulars of the ship can be found in the following reference (Simman 2008).

The diameter and blade number of the propeller is fixed during the design phase, but other parameters may be changed. All deviations from the propeller of the KRISO Container Ship (designated KCS from now on) design will be made clear.

One of the key pieces of information regarding the container ship is its resistance at cruise speed. The total resistance coefficient in model scale (scale factor $\lambda = 31.5994$) was found equal to $3.71 \cdot 10^{-3}$ (Iranzo et al. 2007). This value was used to find the full scale total resistance, equal to approximately 1.8 MN. The propeller must then deliver at least 1.8 MN of thrust to be able to reach a cruise speed of 24 knots.

The object of the scaling was to find a reasonable full scale value, not the 'undeniably correct' one. The point was to figure out approximately what kind of thrust the propeller must deliver.

Another parameter that must be decided is the RPM of the propeller. The propeller of the KCS has a P/D ratio at $0.7R$ equal to 0.997, which could be used to find the resulting RPM. However, the RPM of large single screw ships are usually decided by the engine RPM itself since the propellers tend to be driven directly without any gears. A search was therefore done at the Sea-Web online ship database (www.sea-web.com) to find similar sized ships as the KCS, and to see what RPM the propellers were driven at. The container ship of Hapag-Lloyd AG called 'Box Trader' (IMO No. 9423035) built in 2010, with length 228.62 m and a cruise speed of 23.75 knots was used as comparison. Its engine speed of 102 RPM will therefore serve as the RPM of all propeller designs in this thesis.

4.2 Conventional Propeller

4.2.1 Circulation Distribution

The radial circulation distribution is based on the following expression (Steen 2014):

$$\Gamma(r') = k\left[\sin(\pi r') - a\sin(2\pi r')\right]^m \tag{4.1}$$

where $r' = \frac{r-r_h}{R-r_h}$ and k, a and m are constants. With $k = 1$, $a = 0.3$ and $m = 0.5$, the distribution looks like this, mapped onto the r/R axis:

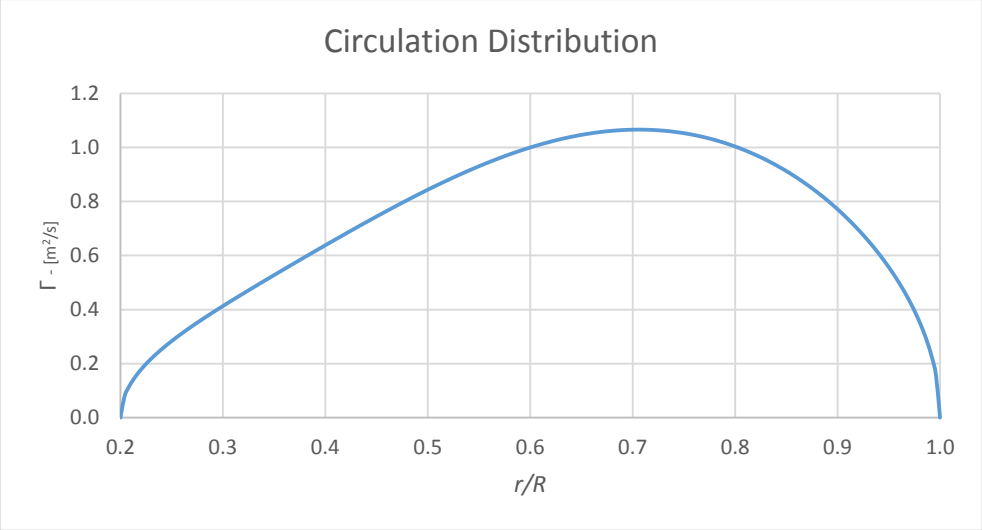

Figure 4.1: The circulation distribution, according to Equation 4.1, with $k = 1$, $a = 0.3$ and $m = 0.5$.

The derivative of this circulation distribution is very high at the end points, which led to dubious results that could not be trusted. The distribution was therefore modified in Microsoft Excel, which could do a sixth-order curve fit over the newly specified points. The resulting polynomial is as follows:

$$\Gamma(x) = k\left[-35.0640x^6 + 76.3500x^5 - 53.5030x^4 + 7.7968x^3 + 3.3104x^2 + 1.0523x + 0.0575\right] \tag{4.2}$$

where k still is a constant, and x runs from 0 to 1.

The resulting distribution looks the following, mapped onto the r/R axis and with $k = 1$:

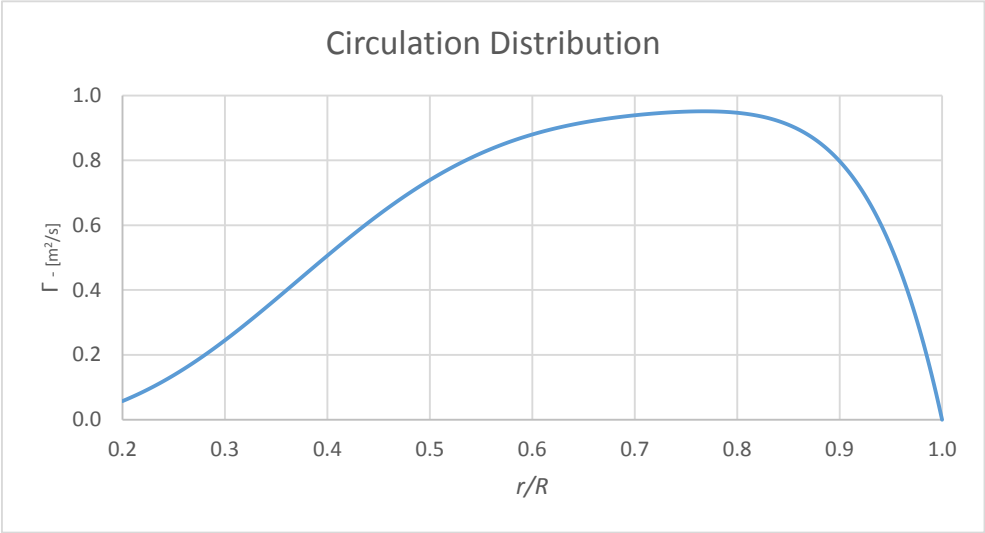

Figure 4.2: The circulation distribution, according to Equation 4.2, with $k = 1$.

The finite value at the hub radius is to avoid the large derivative, and the slope is also more gradual at the propeller tip. The maximum circulation is pushed more towards the tip as well. The derivative of the distribution is as follows:

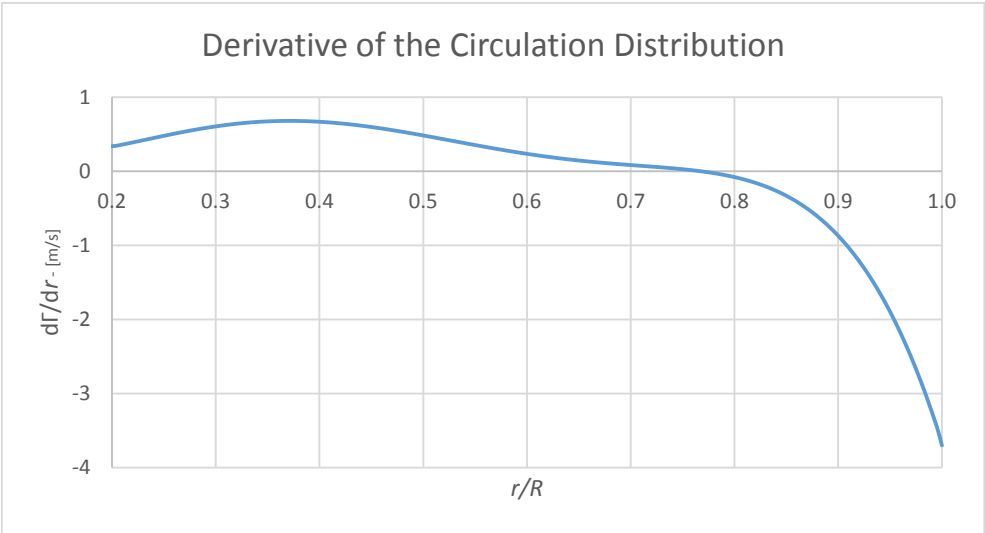

Figure 4.3: The derivative of the circulation distribution, given by Equation 4.2, with $k = 1$.

4.2.2 Chord Length Distribution

The chord length distribution was chosen mostly on the basis of avoiding cavitation. A lot of trial and error was done in order to get a suitable final distribution. A sixth-order curve fit was not accurate enough, so a cubic spline interpolation between the desired values was therefore done in MATLAB instead. The values were made non-dimensional by the diameter, and are as follows:

r/R	0.200	0.300	0.400	0.500	0.600	0.700	0.800	0.900	0.950	0.975	0.990	1.000
c/D	0.160	0.210	0.260	0.296	0.320	0.330	0.320	0.280	0.230	0.186	0.140	0.080

Table 4.1: Values of interpolated non-dimensional chord lengths.

As can be seen, the chord length is not retracted to zero at the tip. The interpolated distribution is as follows when multiplied by the diameter:

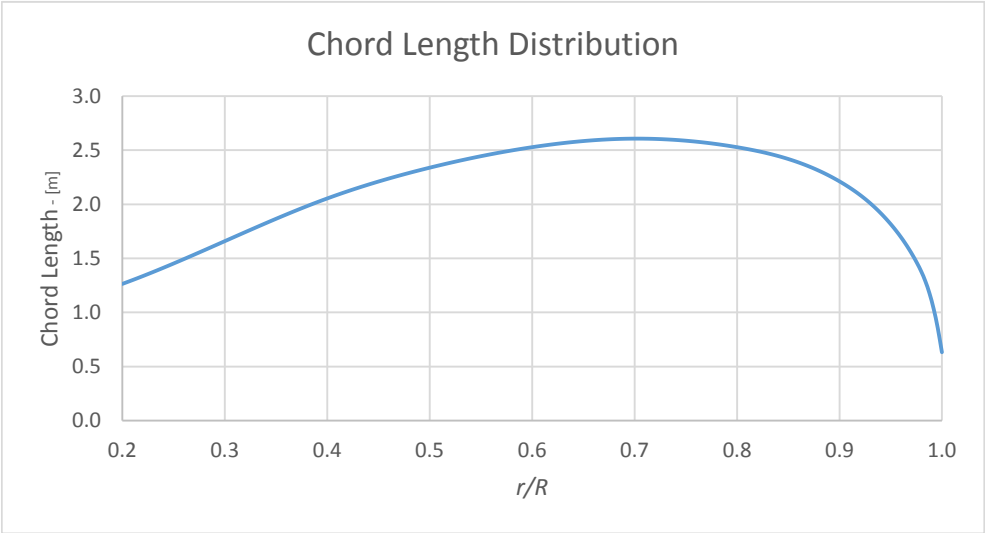

Figure 4.4: The total chord length distribution.

4.2.3 Thickness Distribution

The thickness distribution follows the linear Wageningen distribution as described in Chapter 3.2.4. The lower limit in the following figure is the thickness calculated from Equation 3.4, with yield stress $\sigma_y = 275$ MPa:

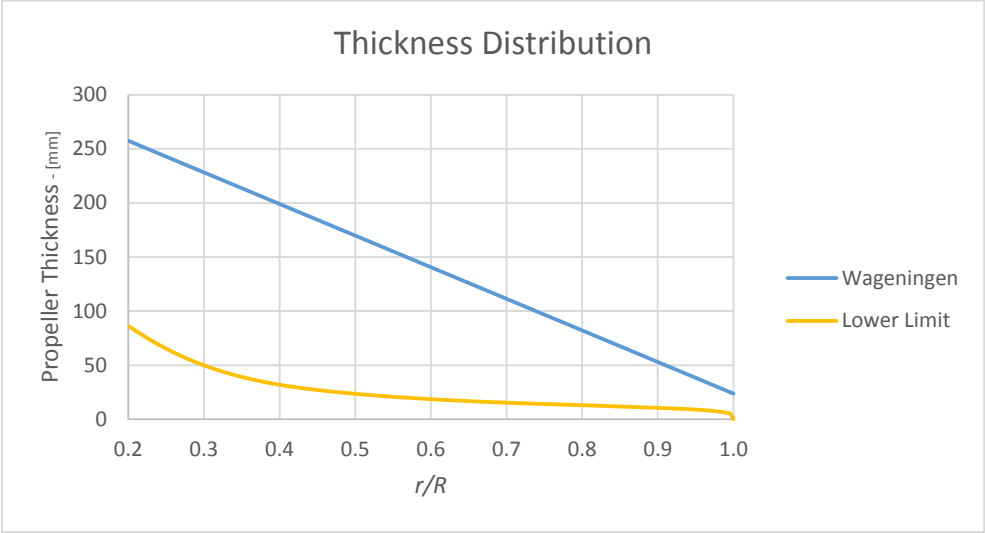

Figure 4.5: The Wageningen thickness distribution is the one that has been used in the design, and the lower limit is based on Equation 3.4, with $\sigma_y = 275$ MPa.

Equation 3.4 takes the actual propeller loading into account, whereas the Wageningen distribution does not. The Wageningen distribution probably overestimates the thickness, and Equation 3.4 probably underestimates it, as discussed in Chapter 3.2.4. The Wageningen distribution was chosen to be on the safe side.

It is necessary to find the t/c distribution that gives the Wageningen distribution after it has been multiplied by the chord length distribution. The best way of assuring this is to solve

the equation $t/c = \frac{t_W}{c}$ at each radial position, where t_W is the Wageningen thickness, and c on the right hand side is the chord length distribution. The resulting t/c distribution is as follows:

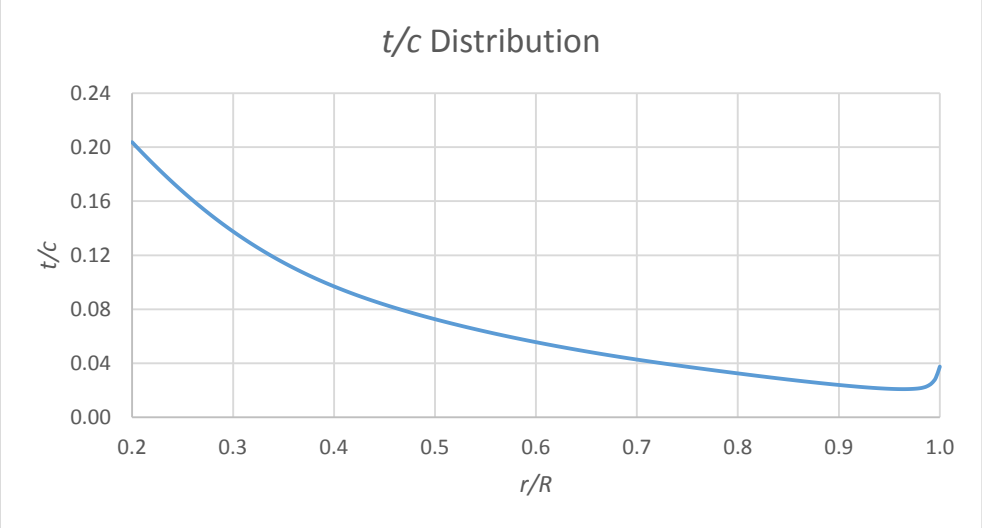

Figure 4.6: The t/c distribution.

4.2.4 Lifting Line Results

The lifting line program can now be run with all these distributions defined. The linear circulation scale factor k is set to 38.055, the ship speed is set to 24 knots, the number of propeller blades is set to five, the propeller speed is set to 102 RPM, the propeller diameter is set to 7.9 m, the propeller hub draught is set to 6.68 m, the density of water ρ is set to 1025 kg/m^3 and the kinematic viscosity of water ν is set to $1.004 \cdot 10^{-6}$ m^2/s. The following results are obtained with the residual convergence criteria set to 10^{-9} and the number of lifting lines set to 1000:

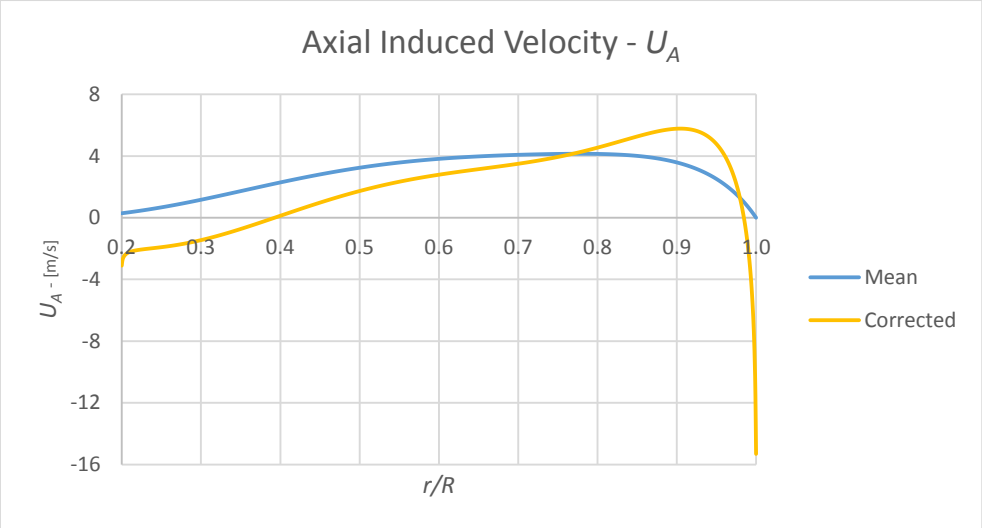

Figure 4.7: Axial induced velocities of the final design.

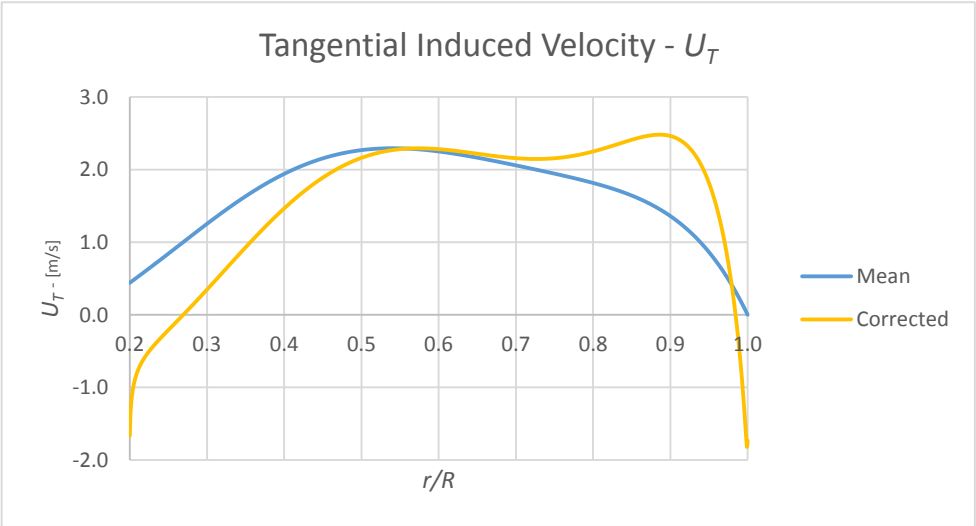

Figure 4.8: Tangential induced velocities of the final design.

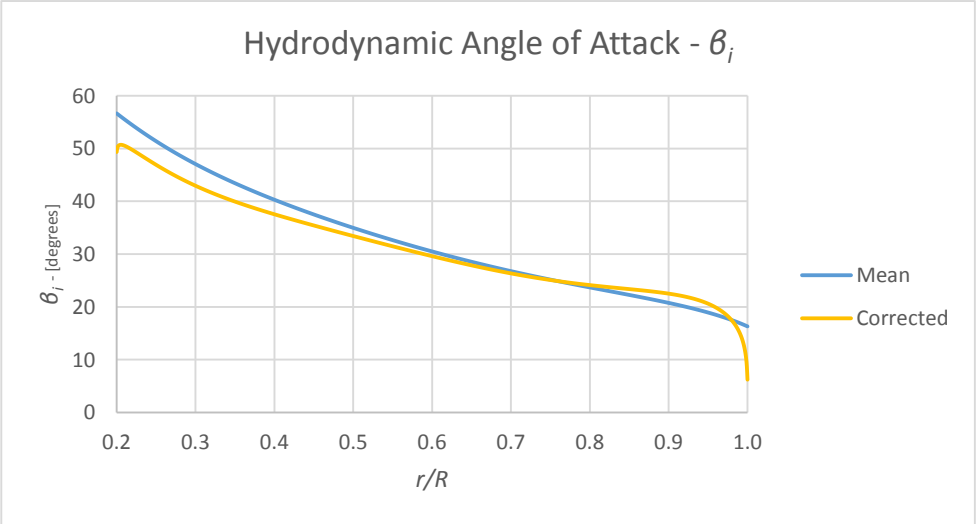

Figure 4.9: Hydrodynamic angle of attack of the final design.

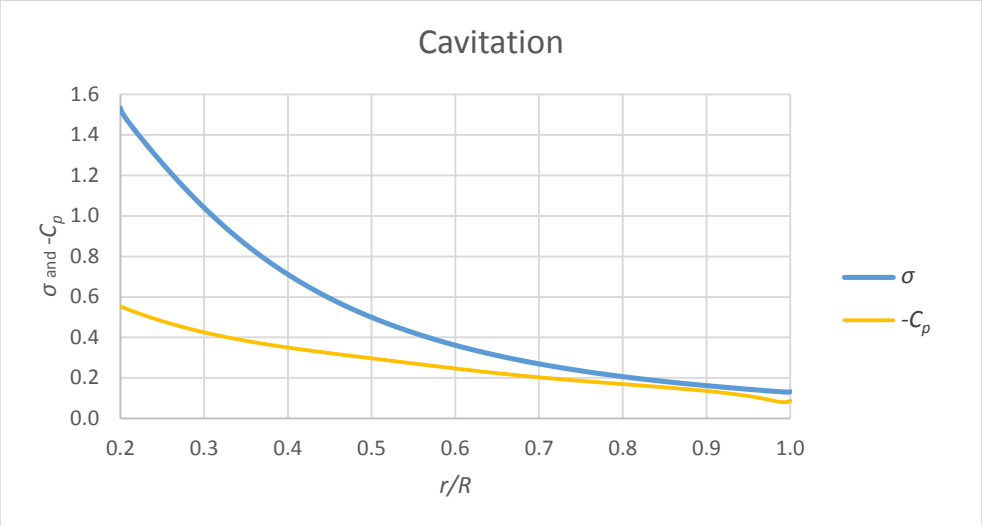

Figure 4.10: Cavitation criteria for the final design – no cavitation when $-C_p < \sigma$.

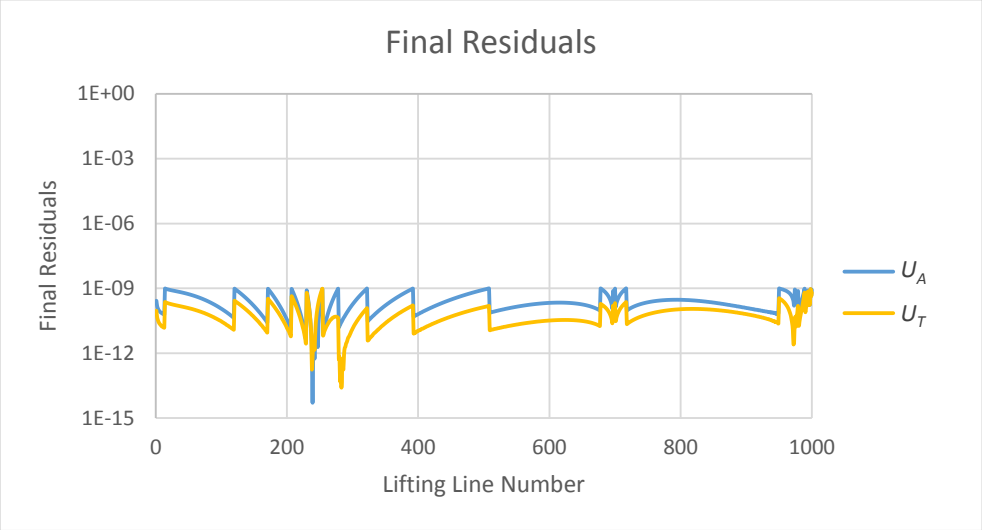

Figure 4.11: Final residuals for each lifting line.

Total thrust	T	2.15 MN
Total torque	Q	2.95 MNm
Efficiency	η	84.4 %
Expanded Area Ratio	EAR	0.7
Pitch ratio at $0.7R$	P/D	1.37
Advance number	J	0.92

Table 4.2: Results of the final design.

At first, the negative induced velocities at certain radial positions, as presented in Figure 4.7 and 4.8, seemed erroneous. Whether they are realistic or not will not be discussed, but it is what the induction factor method may give. Two effects can cause this:

- The r_0-coordinate is small close to the propeller hub, meaning that all the consecutive values of r makes the factor $\frac{1}{r_0-r}$ negative as the integration is done. It is therefore likely that the integral may become negative.

- As r_0 approaches R, the singularity moves towards the tip of the propeller (Figure 3.1). This means that only the part to the left of the singularity is included. Since r has a lower value than r_0 on this side, the factor $\frac{1}{r_0-r}$ is positive, and this should result in the summation of only positive values of the integrand. However, there is only a negative contribution to the integral because of the negative circulation derivative towards the propeller tip, and the fact that the cancelling part on the right side of the singularity is not present.

Maybe a different treatment of the singularity would lead to other results, but the ones obtained here were accepted – backed up by the fact that Justin E. Kerwin also has found negative induced velocities (Kerwin 2001). The very large negative value for the axial velocity is probably not physically correct, which is especially clear by looking at the hydrodynamic angle of attack in Figure 4.9. The negative U_A reduces β_i (Equation 2.18) too much towards the tip. This is therefore corrected by linearly extrapolating from the value at $r/R = 0.9$. Risk of pressure side cavitation and negative lift on the propeller tip would otherwise be present, due to an effective negative angle of attack. Similar is done close to the hub where the tiny

bend is flattened. These corrections are obviously a source of error, as it is difficult to know for sure what the angle should be.

The design is made with a slightly larger thrust than 1.8 MN. This is because 3D effects played a larger role than first anticipated. The correction done in Chapter 3.2.5 was not enough to make the lifting line results and CFD results similar in terms of the key parameters. The thrust was initially too low, so a higher scale factor on the circulation distribution was introduced to compensate. It is therefore highly unlikely that an efficiency of 84.4 % will be achieved in the CFD-results.

The design differs from the standard propeller of the KCS in some aspects:

- The EAR is 0.7, and not 0.8.
- The P/D ratio at $0.7R$ is 1.37, and not 0.997. This indicates that the design J is higher than the one used in the KCS reference, meaning that the KCS reference has a higher propeller speed.
- The hub diameter is $0.2D$, and not $0.18D$.
- In addition, the propeller rotation is left-handed and not right-handed, as will be seen later. This has no influence on the final open water results, and was only done because of more efficient 3D modelling due to the way the foil sections were printed.

A total of 20 foil sections were printed to text files, which will be used as the basis in the CAD modelling.

4.2.5 3D CAD Modelling

The CAD modelling was done in a program called 'Inventor Professional 2015', made by Autodesk. It is a commercial CAD software, with many powerful features. The author is not an experienced CAD modeller in any way, but the final geometry was at least of sufficient quality to be used in the CFD simulations.

It was easy to define new separate work planes in Inventor with their own coordinate system, which the foil sections could be imported to – at their correct radial positions. When rotated to their correct angle of attack, it was possible to create a solid 3D body by 'lofting' a surface through each of the foil sections. This loft procedure was done accurately by also defining guide lines (called 'rails' in Inventor) that were touching the leading and trailing edges of all the foil sections. These provided a boundary for the loft algorithm to follow, capturing all the important features of the propeller geometry.

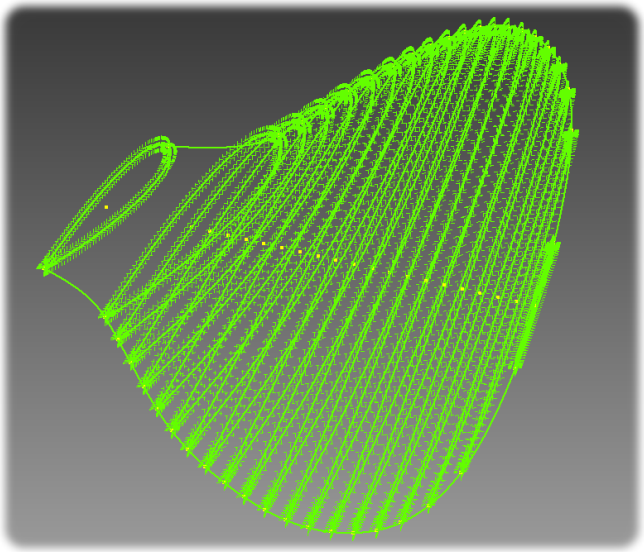

Figure 4.12: The foil sections and guide lines as seen before the lofting procedure.

A standard hub was designed, with the following dimensions (in metres):

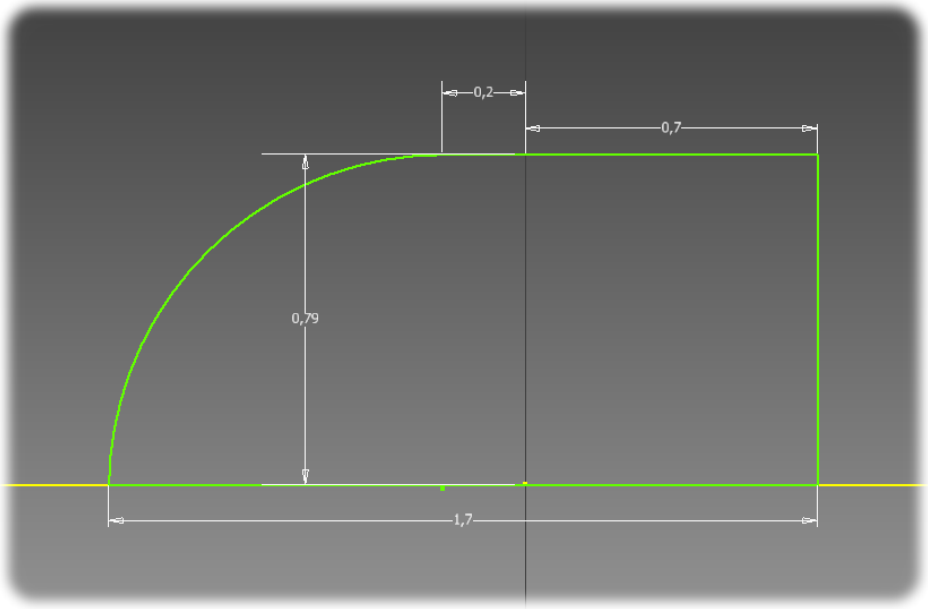

Figure 4.13: The half cross section of the propeller hub. The solid hub is generated by revolving the sketch 360° around the horizontal axis. All dimensions are in metres.

Only one blade needs to be modelled, as it is possible to repeat it in a circular pattern which finishes the remaining four.

The final propeller looks as follows:

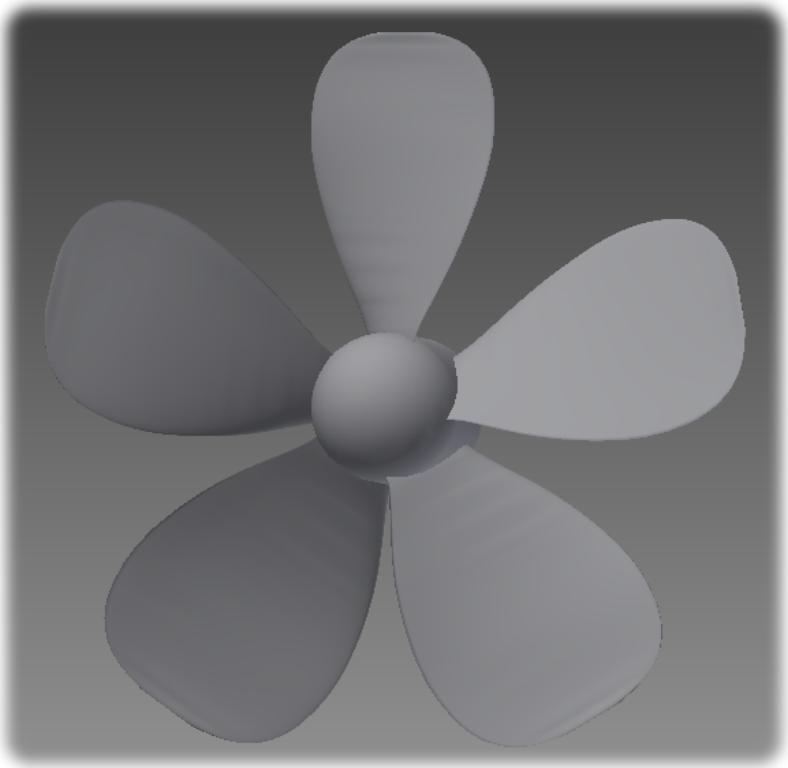

Figure 4.14: Final geometry of the conventional propeller.

Modern propellers may have a lot of skew to help minimising cavitation. The designs in this thesis will have no skew (except for the winglet propellers that have some skew on the outer sections). The applied skew is tailored to the wake field of the ship that the propeller should power. Only the open water performance is to be tested, completely free of any of wake, so no skew is therefore added.

4.3 Tip Loaded Propeller

The winglet propellers have the same base design – i.e the exact same tip loaded circulation distribution, as well as identical chord length and thickness distributions. The propeller tips themselves are the only difference. This tip loaded base geometry will be presented in the following chapter.

4.3.1 Circulation distribution

An Excel curve fit was done, and the following sixth-order polynomial represents the circulation distribution:

$$\Gamma(x) = k\left[-22.8500x^6 + 46.3040x^5 - 25.4270x^4 - 4.3941x^3 + 5.6943x^2 + 0.8884x + 0.0964\right] \quad (4.3)$$

where x runs from 0 to 1. Mapped onto the r/R axis, the resulting distribution is as follows, with $k = 1$:

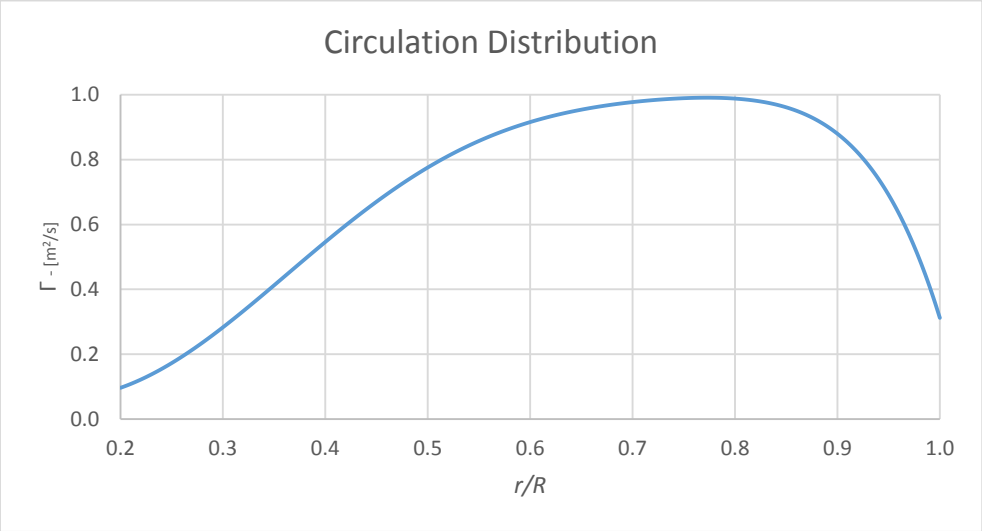

Figure 4.15: The tip loaded circulation distribution, according to Equation 4.3, with $k = 1$.

The derivative of the circulation distribution is as follows:

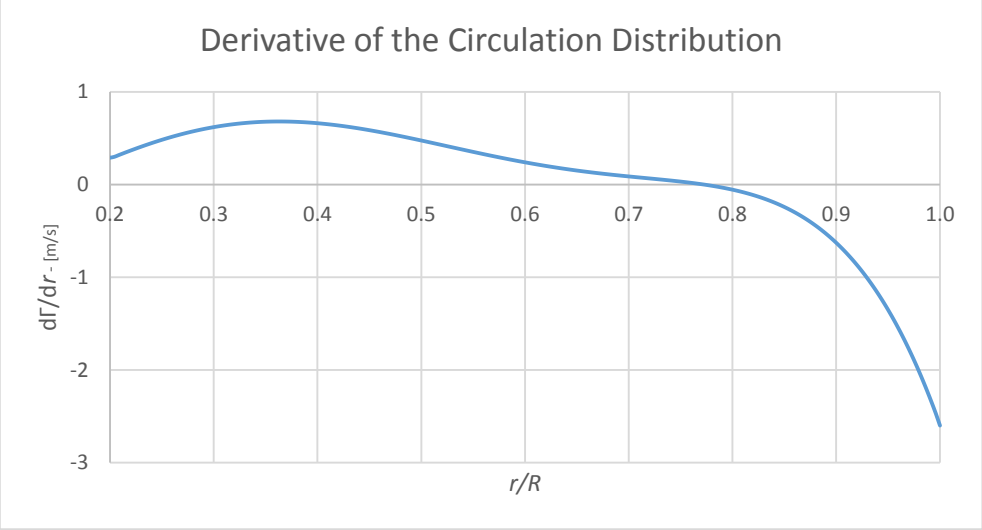

Figure 4.16: The derivative of the circulation distribution, given by Equation 4.3, with $k = 1$.

There is no clever theory behind the choice of this exact circulation distribution. A tip value that seemed appropriate, and did not introduce severe cavitation problems with a sensible tip chord length was chosen.

4.3.2 Chord Length Distribution

The curve fit in Excel was better for this chord length distribution, and led to the following expression:

$$\frac{c(x)}{D} = -17.6590x^6 + 55.6410x^5 - 69.5800x^4 + 43.3210x^3 - 14.4010x^2 + 2.9474x - 0.1055 \quad (4.4)$$

where x runs from 0.2 to 1. The final values are obtained by multiplying with the diameter D, and looks as follows:

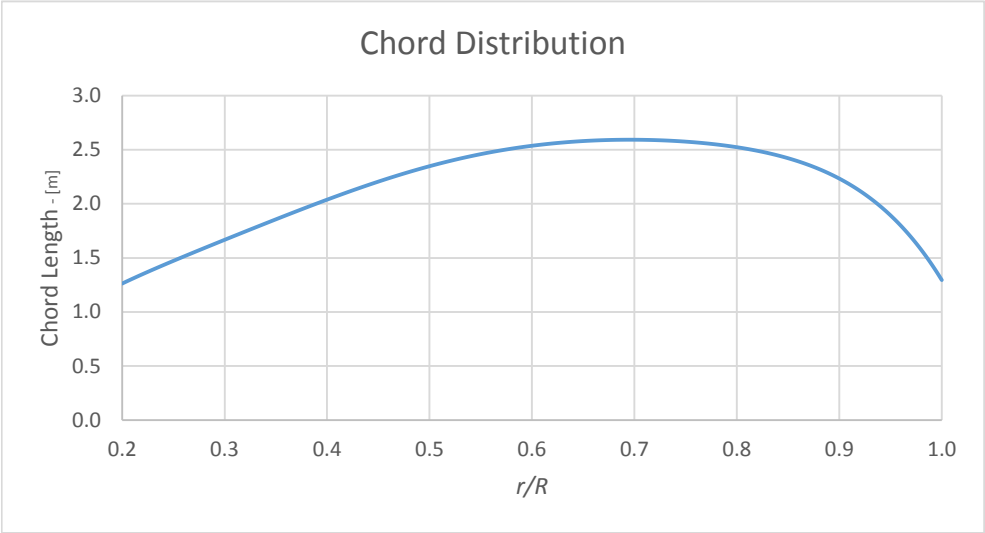

Figure 4.17: The total tip loaded chord length distribution.

4.3.3 Thickness Distribution

The thickness distribution follows the same Wageningen curve as the conventional propeller loading, shown in Figure 4.5. The lower limit for the tip loaded propeller follows almost the exact same curve as for the conventional propeller loading.

The thickness to chord ratio distribution for the tip loaded propeller is as follows:

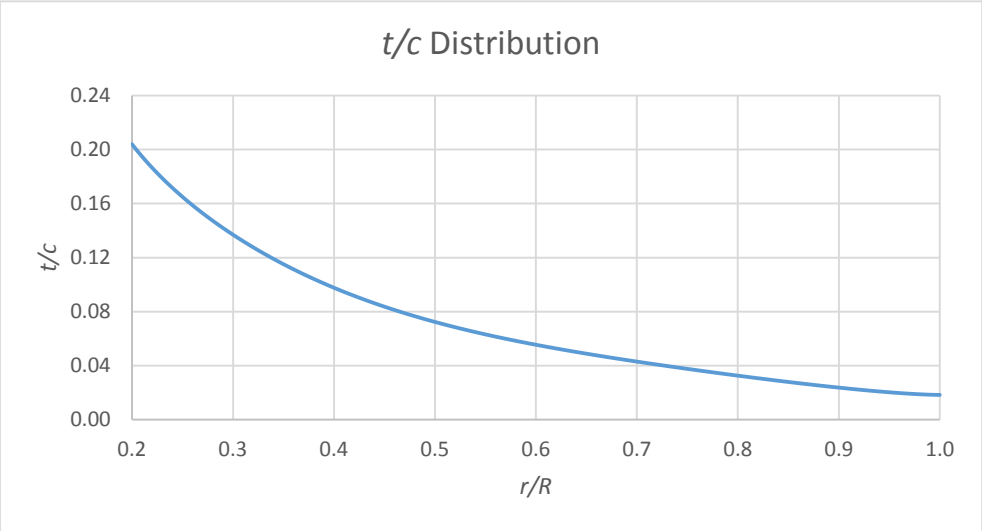

Figure 4.18: The t/c distribution for the tip loaded propeller.

4.3.4 Lifting Line Results

With the exact same settings as described in Chapter 4.2.4, the results are as follows:

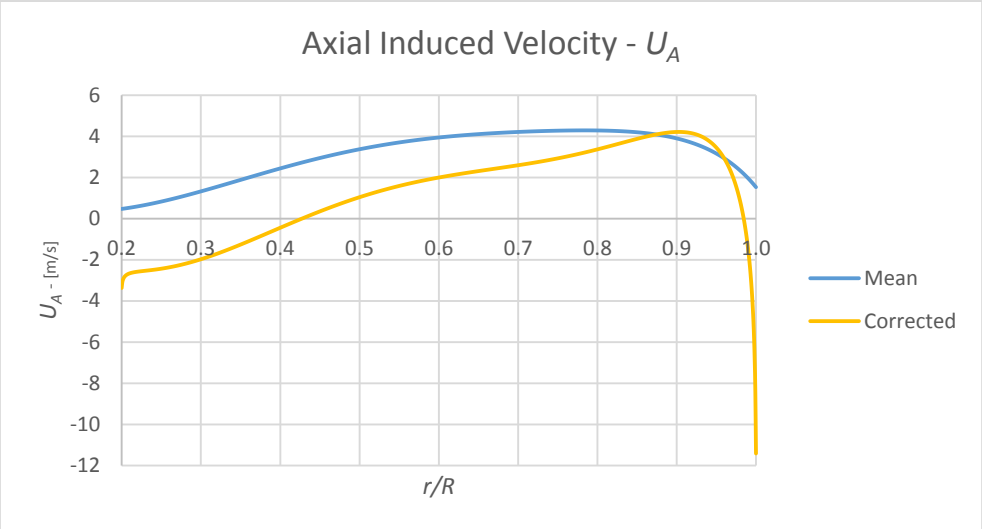

Figure 4.19: Axial induced velocities of the final tip loaded design.

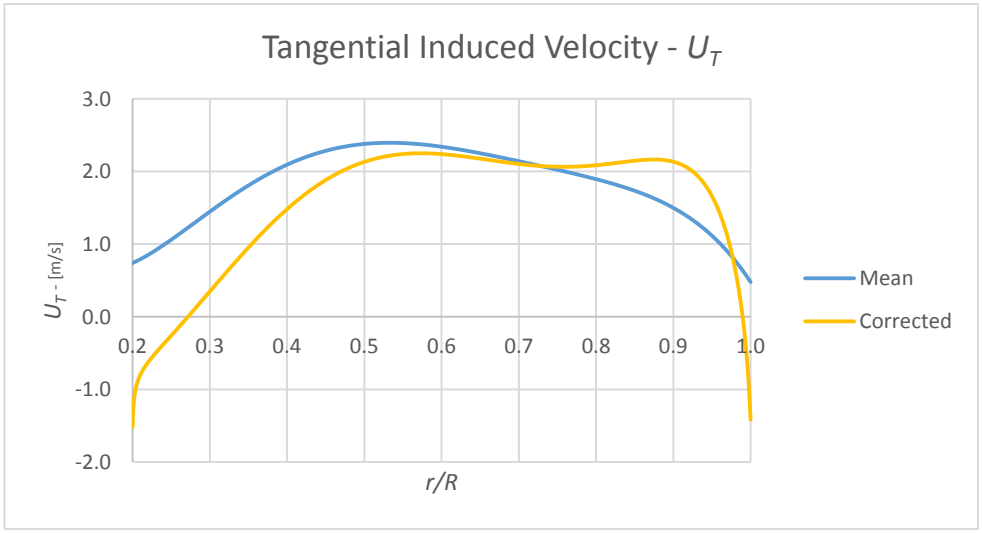

Figure 4.20: Tangential induced velocities of the final tip loaded design.

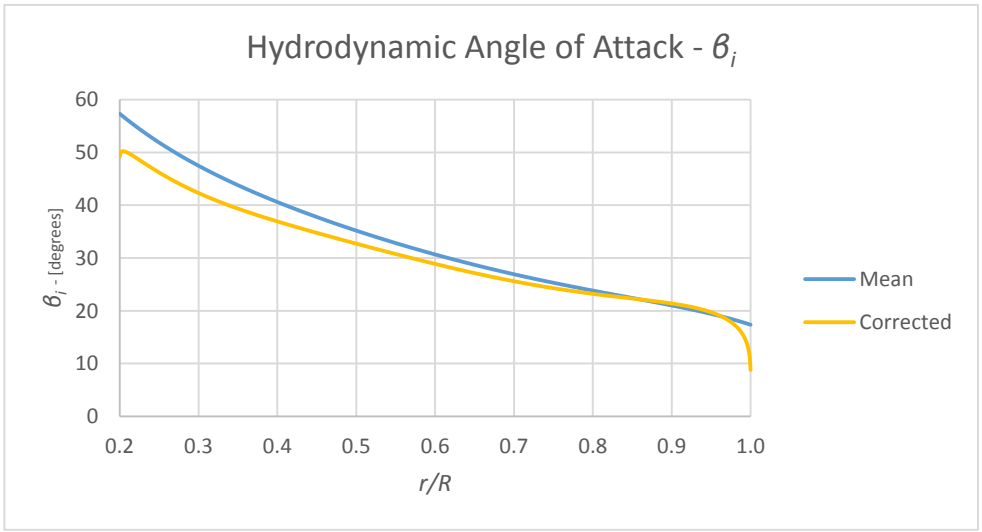

Figure 4.21: Hydrodynamic angle of attack of the final tip loaded design.

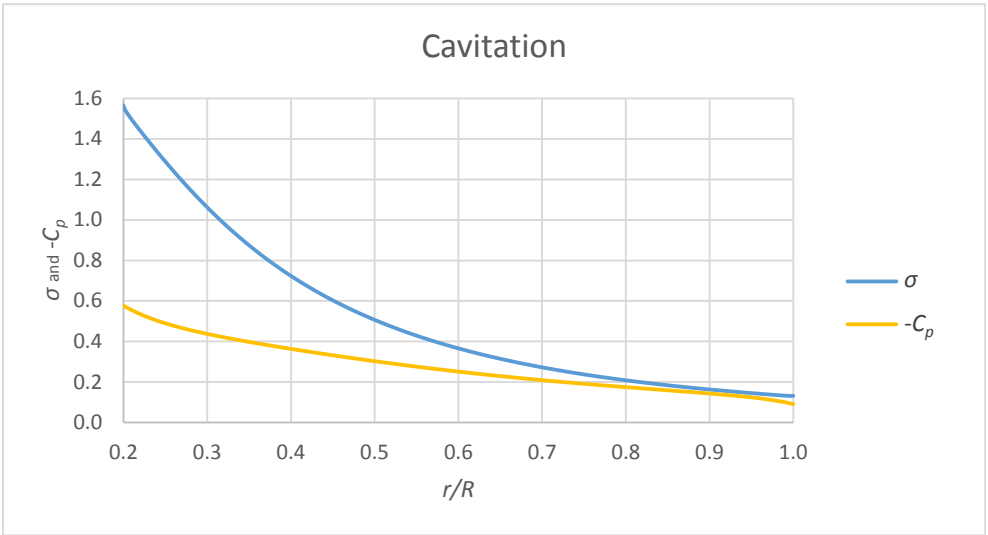

Figure 4.22: Cavitation criteria for the final tip loaded design – no cavitation when $-C_p < \sigma$.

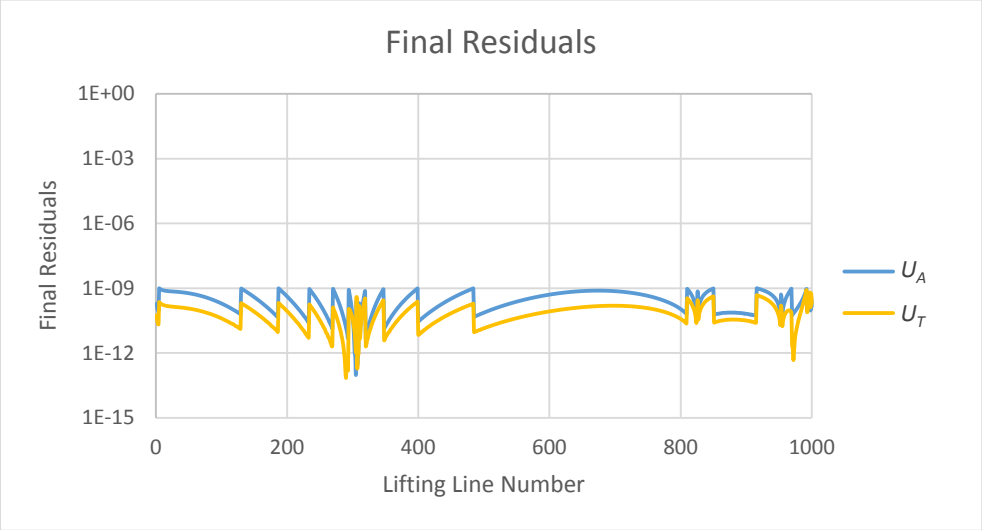

Figure 4.23: Final residuals for each lifting line.

Total thrust	T	2.36 MN
Total torque	Q	3.10 MNm
Efficiency	η	88.01 %
Expanded Area Ratio	EAR	0.7
Pitch ratio at $0.7R$	P/D	1.33
Advance number	J	0.92

Table 4.3: Results of the final tip loaded design.

The hydrodynamic angle of attack is corrected at the end points in the same way as described in Chapter 4.2.4.

4.3.5 3D CAD Modelling

The 3D CAD modelling is done in the same way as described in Chapter 4.2.5. The final design is as follows:

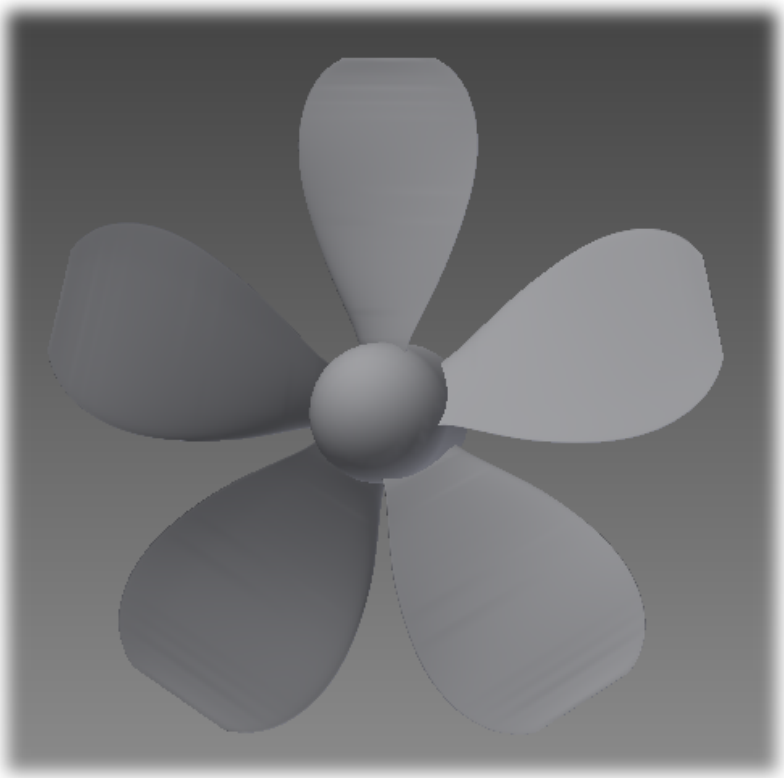

Figure 4.24: Final geometry of the tip loaded propeller.

4.4 Winglet Design

The tip loaded propeller was designed solely to be modified with winglets. A finite circulation at the propeller tip is only possible in theory, as the pressure difference between the suction and pressure side of the propeller cannot be maintained here in reality. The lift obviously has to end as the propeller blade ends. This has to happen gradually, no matter what the theoretical circulation here would be, because discontinuities do not exist in reality. A large circulation at the tip would therefore most likely not give much more lift, but potentially a larger tip vortex instead.

The aim is to design a winglet that will maintain the pressure difference as much as possible towards the propeller tip before the lift is gradually reduced to zero along the winglet span. The foil sections of the winglet itself will therefore be lifting, i.e they will be cambered. Designing a winglet thoroughly is a difficult task, meaning that there are details that simply cannot be evaluated in the limited scope of this thesis. The exact geometry of the winglet, and distribution of lift along it, will therefore not be justified by any grand theories or best practices. There is after all very little guidance to find for such a winglet application.

The winglet fitted propellers are based on the tip loaded propeller geometry defined in Chapter 4.3. A few modifications are done: Some skew is introduced at the outermost foil sections to manage to place the winglets at the desired location. The trailing edge of the propeller blade should not contract towards the propeller center, but rather continue in a more or less straight line to the tip. This is done by skewing the outer foil sections further towards

the trailing edge. The propeller blade is also curved gradually towards the suction side, before the winglet foil sections eventually are added.

4.4.1 Tall Variant

Winglet Foil Sections

Two additional foil sections are used for the winglet. This means that the total number of foil sections used to describe the entire propeller geometry becomes 22 (20 are already printed from the lifting line program). The chord lengths for the winglet sections are half the value of the preceding chord length. When the last chord length prior to the winglet is 1.264 m (as defined by Equation 4.4), the first winglet section has length 0.632 m, and the last section has length 0.316 m. The thickness is kept constant, which means that the t/c value is doubled for each section.

The camber for the first winglet section is the same as the preceding blade section, and the last winglet section has a camber equal to zero.

Suction Side Curvature Distribution

The curvature towards the suction side is as follows, where z is the vertical offset from the base line:

r/R	0.200	$\rightarrow$	0.900	0.958	0.980	0.991	1.000
10 z/D	0.000	$\rightarrow$	0.000	0.038	0.127	0.380	0.633

Table 4.4: Values of the curvature towards the suction side.

This gives a total winglet height equal to 0.5 m. It is important to angle the foil sections so that they have their lift vector normal to the new base line because of the introduced curvature.

Skew Distribution

The skew is as follows, where y is the horizontal offset from the base line:

r/R	0.200	$\rightarrow$	0.700	0.747	0.789	0.832	0.874	0.916	0.958	0.980	0.991	1.000
y/c	0.000	$\rightarrow$	0.000	0.005	0.010	0.020	0.030	0.040	0.100	0.300	1.250	3.300

Table 4.5: Values of the curvature towards the suction side.

The values are made non-dimensional with respect to the local chord length, that is the curve following Figure 4.17, and the values as described in the 'Winglet Foil Section' above. The last winglet foil section is therefore offset by 1.043 m.

3D CAD Modelling

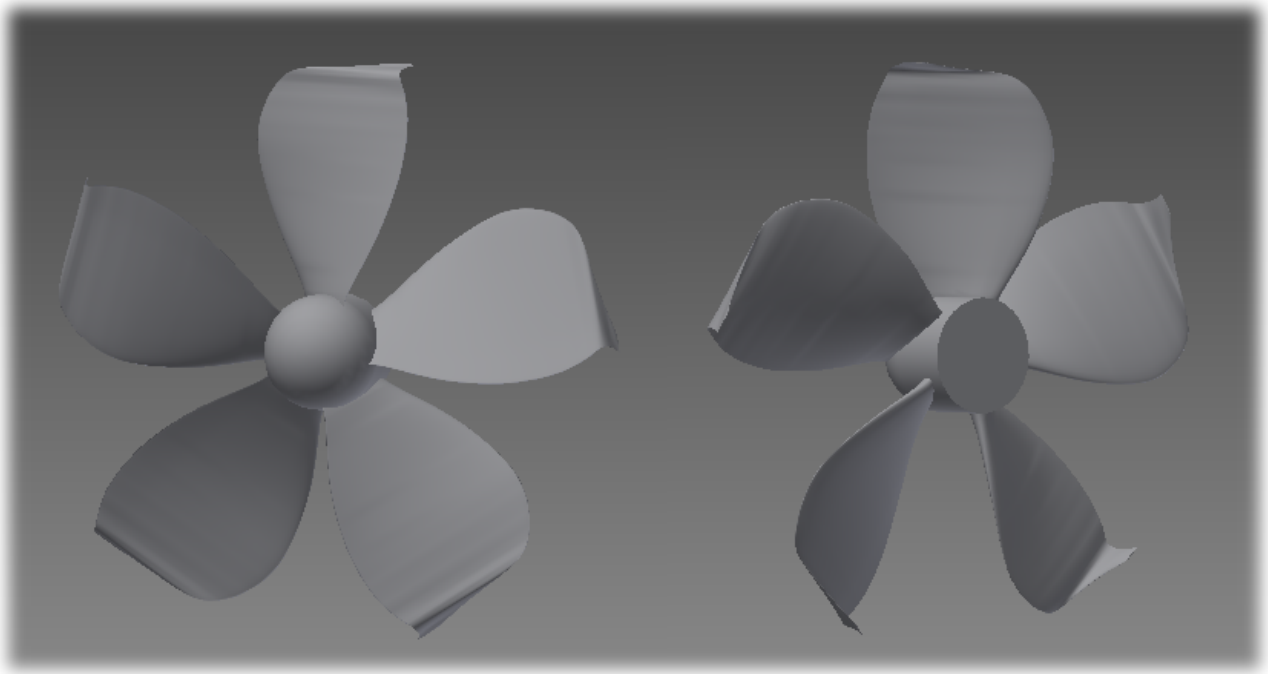

Figure 4.25: Final geometry of the winglet fitted propeller (tall variant).

It is worth specifying that the diameter of the winglet fitted propeller is exactly 7.9 m, just as the conventional design.

An important detail about the design that has to be mentioned is that the winglet is not curved to follow the circular motion of the propeller – that is, it is straight. The winglet chords should be curved to follow a circle with radius equal to the radial position of each section. The author was unable to accomplish this in any good way due to lack of 3D modelling experience. A more skilled CAD user would probably be able to pull it off much better, but the easier way had to be chosen in order to not spend too much time on CAD modelling. This is far from an optimum design, and will most probably make the winglet work with some angle of attack, which is negative for a number of reasons.

4.4.2 Short Variant

Winglet Foil Sections

The foil sections of the short winglet variant is exactly the same as the tall variant.

Suction Side Curvature Distribution

r/R	0.200	$\rightarrow$	0.900	0.958	0.980	0.991	1.000
$10\ z/D$	0.000	$\rightarrow$	0.000	0.025	0.089	0.190	0.380

Table 4.6: Values of the curvature towards the suction side.

This gives a total winglet height equal to 0.3 m.

Skew Distribution

r/R	0.200	$\rightarrow$	0.700	0.747	0.789	0.832	0.874	0.916	0.958	0.980	0.991	1.000
y/c	0.000	$\rightarrow$	0.000	0.005	0.010	0.020	0.030	0.050	0.100	0.350	1.250	3.300

Table 4.7: Values of the curvature towards the suction side.

The total offset of the last winglet foil section is also in this case 1.043 m.

3D Cad Modelling

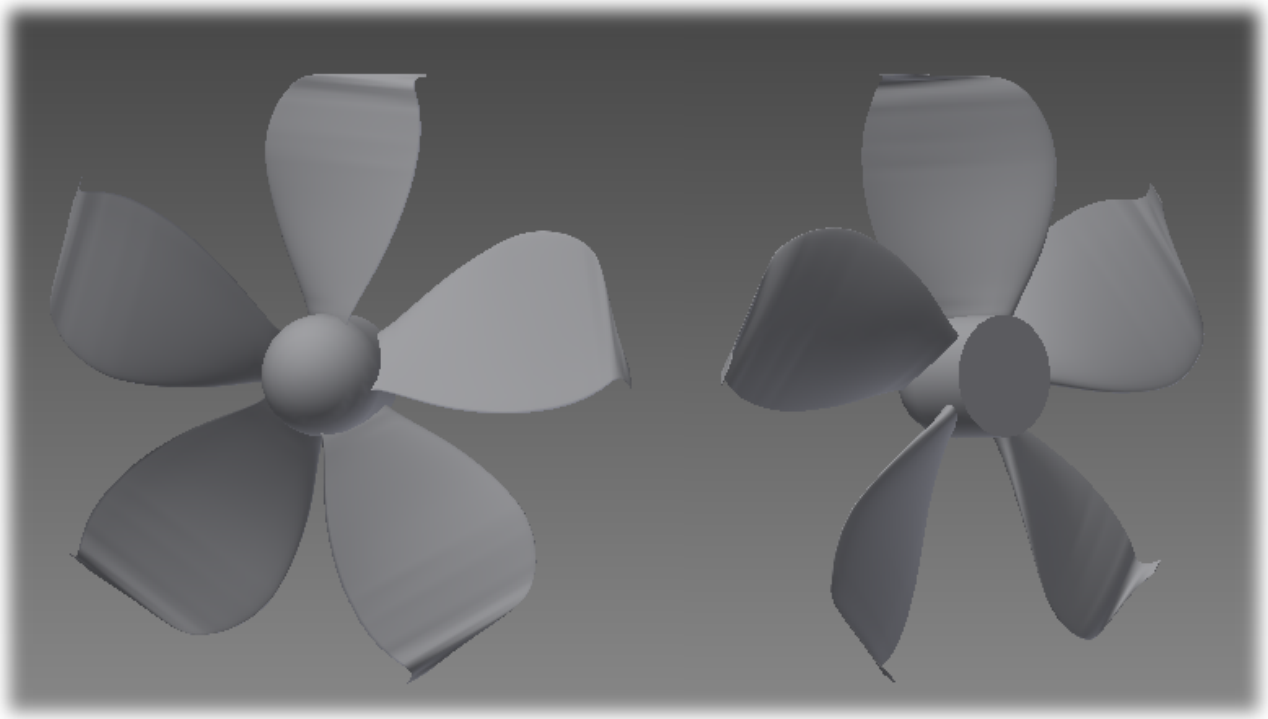

Figure 4.26: Final geometry of the winglet fitted propeller (short variant).

The winglet is also here not curved – same as for the tall variant.

Chapter 5

Fluid Flow Simulations

5.1 Governing Equations

General fluid flow behaves chaotic and random, with both large and small scale spatial and temporal effects present. For example by looking at a river flowing, it is clear that it is dominated by a certain velocity and direction – but it might also swirl into smaller or larger eddies locally, flowing in all directions, more or less at random. The flow becomes increasingly turbulent and chaotic if for example a waterfall approaches – with spray, foam and a mixing of air and water as the outcome.

The mathematical equations governing viscous fluid flow have been known for more than a century, and are usually termed the 'Navier-Stokes Equations', named after Claude-Louis Navier and George Gabriel Stokes who discovered them. These equations are a set of equations, one for each spatial dimension. They include both the time dependent flow acceleration, the nonlinear time independent spatial convective acceleration, as well as pressure driven forces and viscous forces. The constant viscosity, incompressible version of the equations is expressed in compact vector notation in the following way:

$$\rho \frac{D\vec{\mathbf{U}}}{Dt} = -\nabla p + \mu \nabla^2 \vec{\mathbf{U}} + \rho \vec{\mathbf{g}} \tag{5.1}$$

ρ is the fluid density, $\vec{\mathbf{U}}$ is the velocity vector with x-, y- and z-components $[u \ v \ w]$ respectively, p is the pressure, μ is the dynamic viscosity, and the acceleration of gravity vector $\vec{\mathbf{g}}$ with components $[g_x \ g_y \ g_z]$ has been substituted for the general body force vector $\vec{\mathbf{f}}$.

∇ is the vector differential operator, here acting on a general scalar ϕ:

$$\nabla \phi = \begin{bmatrix} \frac{\partial \phi}{\partial x} & \frac{\partial \phi}{\partial y} & \frac{\partial \phi}{\partial z} \end{bmatrix} \tag{5.2}$$

∇^2 is the same as $\nabla \cdot \nabla$, yielding the scalar Laplace differential operator, here acting on a general scalar ϕ:

$$\nabla^2 \phi = \frac{\partial^2 \phi}{\partial x^2} + \frac{\partial^2 \phi}{\partial y^2} + \frac{\partial^2 \phi}{\partial z^2} \tag{5.3}$$

$\frac{D}{Dt}$ is the material derivative operator, here acting on a general scalar ϕ:

$$\frac{D\phi}{Dt} = \frac{\partial \phi}{\partial t} + \vec{\mathbf{U}} \cdot \nabla \phi = \frac{\partial \phi}{\partial t} + u \frac{\partial \phi}{\partial x} + v \frac{\partial \phi}{\partial y} + w \frac{\partial \phi}{\partial z} \tag{5.4}$$

A mass continuity equation is also necessary, ensuring that the total amount of mass in the system is kept constant. The mass continuity equation simplifies to a volume continuity of the following form in the incompressible case:

$$\nabla \cdot \vec{\mathbf{U}} = 0 \tag{5.5}$$

Written explicitly in each of its three components, Equation 5.1 becomes as follows:

$$\rho\left(\frac{\partial u}{\partial t} + u\frac{\partial u}{\partial x} + v\frac{\partial u}{\partial y} + w\frac{\partial u}{\partial z}\right) = -\frac{\partial p}{\partial x} + \mu\left(\frac{\partial^2 u}{\partial x^2} + \frac{\partial^2 u}{\partial y^2} + \frac{\partial^2 u}{\partial z^2}\right) + \rho g_x \tag{5.6}$$

$$\rho\left(\frac{\partial v}{\partial t} + u\frac{\partial v}{\partial x} + v\frac{\partial v}{\partial y} + w\frac{\partial v}{\partial z}\right) = -\frac{\partial p}{\partial y} + \mu\left(\frac{\partial^2 v}{\partial x^2} + \frac{\partial^2 v}{\partial y^2} + \frac{\partial^2 v}{\partial z^2}\right) + \rho g_y \tag{5.7}$$

$$\rho\left(\frac{\partial w}{\partial t} + u\frac{\partial w}{\partial x} + v\frac{\partial w}{\partial y} + w\frac{\partial w}{\partial z}\right) = -\frac{\partial p}{\partial z} + \mu\left(\frac{\partial^2 w}{\partial x^2} + \frac{\partial^2 w}{\partial y^2} + \frac{\partial^2 w}{\partial z^2}\right) + \rho g_z \tag{5.8}$$

Equations 5.6 – 5.8 are a set of mixed hyperbolic-parabolic, unsteady, nonlinear, second order partial differential equations. Let there be no doubt – they are difficult to solve. With present methods, they are in fact *impossible* to solve for turbulent high Reynolds number flows because of randomly time dependent boundary conditions (White 2006). It is the nonlinear convective $\vec{\mathbf{U}} \cdot \nabla\vec{\mathbf{U}}$ term that makes the Navier-Stokes equations particularly troublesome, but good approximate results are obtained through sophisticated numerics and clever turbulence modelling.

Another interesting fact about these equations is that it has yet to be proven that smooth solutions always exist in three dimensional space – smooth in the sense that the solution is without singularities. This is called the 'Navier–Stokes Existence and Smoothness' problem, and is one of the seven 'Millennium Prize Problems' – that is, one of the seven most important open problems in mathematics, awarded with a USD 1 million prize if solved. Despite this fact, the equations are widely used with great practical success – maybe to some mathematicians vexation.

5.2 Computational Fluid Dynamics

It is impossible to solve the Navier-Stokes equations analytically for most (in essence *all*) practical purposes. Fortunately, numerics come to the rescue. Numerical methods used in fluid analysis is termed 'Computational Fluid Dynamics' (CFD), with the 'Finite Volume Method' (FVM) being the most popular technique. The FVM has proven successful since its developments in the early 1970's despite little numerical analysis, and difficulty to extend the method to higher orders of accuracy compared with finite element or finite difference methods. Some reasons for the success are the method's discrete conservation property, integral formulation in physical space, shock capturing capability, geometric flexibility and local grid adaption capability (Müller 2012).

In the FVM, the solution domain is subdivided into a finite number of control volumes that are used to solve the set of equations, which for this purpose are recast into a conservative form. Their integral forms are obtained by integrating them over the cell centred control volumes, which makes it possible to find expressions for values of the conserved variables at the cell faces by difference methods. There are a vast number of ways to do this, depending on the desired level of accuracy and stability. The second order upwind scheme is popular for the convection term, with an applied flux-limiter to reduce numerical oscillations at discontinuities (like for example shocks, but these are not present in an incompressible simulation). In an upwind

scheme, the face values are interpolated from cells that are *upwind* of the flow direction relative to the interesting cell face. The second-order upwind scheme is not especially numerically diffusive, which is good in some cases, but could in other cases lead to poor convergence and non-physical numerical oscillations (like for the already mentioned flow discontinuities). This is handled by flux-limiters that reduce the scheme to something like the first order upwind at discontinuities, which is much more robust in terms of convergence. This is a good trade-off between accuracy and stability.

The goal is to end up with a system of linear equations with a total number of unknowns equal to the number of cells in the solution domain. Linearisations and iterative techniques have to be applied in order to solve the nonlinear parts of the equations, as well as some sort of time-integration scheme to control the transient terms. The time-integration is usually implicit for greater stability, and of first or second order. Modern multigrid algorithms are used to solve the final linear equations, resulting in nearly linear scaling with the number of unknowns.

It is referred to text books describing the FVM in detail for a more in-depth explanation of the different numerical schemes and discretisation techniques, e.g (Versteeg and Malalasekera 2007).

5.3 Choice of Solver and Numerical Models

5.3.1 STAR-CCM+

The CFD software used in this thesis is STAR-CCM+ (version 9.04.011), which is a powerful commercial multiphysics software developed by CD-adapco, with special emphasis put on thermo and fluid dynamics.

A good reputation in marine applications, personal experience, easy access to student licenses and a helpful support service were reasons for the choice of solver.

5.3.2 Numerical Models

Steady State Simulations

The flow field behind a propeller might at a first glance look highly irregular – but actually, the truth is quite the contrary, at least for a smooth inflow, which is the case for an open water test. This allows for a 'steady state simulation', or time independent solution. The flow conditions are set, and the solver iterates until a steady state situation is met, avoiding time-integration altogether. A complete open water test must include a large number of advance numbers (different flow conditions), which would require immense computation resources for an accurate time dependent, unsteady solution. It is therefore highly desirable to use a steady state approach as much as possible, and this has been done for all simulations except for the unsteady cavitation analysis.

The chosen numerical models for the steady state simulations are as follows:

- Incompressible single phase fluid
- Moving Reference Frame
- Segregated flow solver with the SIMPLE algorithm for pressure-velocity coupling
- Algebraic Multigrid iteration technique
- The $k-\omega$ SST Menter turbulence model

- High $y+$ wall treatment
- Second order upwind convection scheme
- Hybrid Gauss-LSQ gradient scheme with the unmodified Venkatakrishnan limiter

The Moving Reference Frame (MRF) model is used to take care of motion in a steady state simulation. This is done by defining both a static region and a 'moving' region within the computation domain, and coupling them with an overlapping interface. A constant grid flux is generated in the appropriate conservation equations of the moving region, based on the reference frame's properties (e.g a specified rotation) (CD-adapco 2015). The propeller is therefore static, but its motion is introduced artificially.

The segregated flow solver solves each equation individually (the momentum equation and the pressure correction equation), and later couples them with the SIMPLE algorithm (Semi Implicit Method for Pressure Linked Equations).

The $k-\omega$ SST (Shear Stress Transport) turbulence model by F. R. Menter is widely used and well proven. It is a two equation model, which blends the $k-\varepsilon$ and original $k-\omega$ model, in theory achieving the best of the two (CD-adapco 2015).

The 'High $y+$ wall treatment' model is all about turbulent boundary layers. The $y+$ parameter is a non-dimensional wall distance, defined as follows:

$$y+ = \frac{u_* y}{\nu} \tag{5.9}$$

u_* is the friction velocity at the nearest wall, y is the distance to the nearest wall (effectively the height of the innermost cell), and ν is the kinematic viscosity of the fluid. u_* is defined as follows, where τ_w is the wall shear stress:

$$u_* = \sqrt{\frac{\tau_w}{\rho}} \tag{5.10}$$

The high $y+$ model is used for the logarithmic region of the turbulent boundary layer, which is valid for $y+$ values in the range of approximately 30 to 500 (McDonough 2007). However, errors increase with large values of $y+$, which makes it wise to aim for upper values substantially lower than 500 (CD-adapco 2015).

The $y+$ criteria puts a constraint on the cell size near the propeller surface. It is important to have a fine enough mesh here to be able to resolve the boundary layer with sufficient accuracy, but it is as always a trade-off between accuracy and computation cost. A maximum $y+$ value of 150 has been set as an upper limit for the simulations in this thesis.

Most of the numerical models and their internal settings are chosen automatically by STAR-CCM+ as a best practice starting point. More skilled users might get even better results by altering the models additionally, but this has not been done in the following simulations.

Additional details and in-depth explanations of the selected numerical models are beyond the scope of this thesis.

Unsteady Simulations

Only the short winglet at three different advance numbers was simulated with an unsteady approach due to the computational cost. The numerical settings were as follows:

- Incompressible two phase solver based on the 'Volume of Fluid' method
- Overset mesh approach ('Chimera grids') with linear interpolation
- Segregated flow solver with the unsteady SIMPLE algorithm for pressure-velocity coupling
- Algebraic Multigrid iteration technique
- 1^{st} order, backward Euler implicit time stepping
- 10 innter iteration per time step
- The $k-\omega$ SST Menter turbulence model
- High $y+$ wall treatment
- Second order upwind convection scheme
- Hybrid Gauss-LSQ gradient scheme with the unmodified Venkatakrishnan limiter

Both water and air has been modelled, and an overset mesh technique has been used to handle the propeller motion, which is one of the many nice features of STAR-CCM+. Two regions are made – one background mesh and one overset mesh that is rotating. The overset mesh is actually on top of the background mesh, and values are linearly interpolated between them. Cells in the background mesh that are 'behind' the overset mesh are disabled and cut away. This approach is particularly useful for large motions, such as a rotating propeller or other arbitrary large scale displacements. The overset mesh is physically moving, contrary to the MRF approach in the steady state simulations where the 'moving' region was static.

The time step size is constrained to ensure 1° of propeller rotation per timestep, implying a magnitude of 0.001634 s when the propeller is rotating at 1.7 rps. Such a small rotation per time step is widely used, and usually the recommended practice (Krasilnikov, Zhang, and Hong 2009).

The physical constants chosen for water and air are as follows, which except for the water density are the standard values selected by STAR-CCM+:

Fluid	*Density* ρ		*Dynamic viscosity* μ	
Water	1025	kg/m^3	$8.88710 \cdot 10^{-4}$	Ns/m^2
Air	1.18415	kg/m^3	$1.85508 \cdot 10^{-5}$	Ns/m^2

Table 5.1: Physical constants of water and air as used in the simulations.

The values for water are identical in the steady state simulations.

5.4 Computer Cluster

CFD simulations are costly in terms of computation resources. The number of control volumes that a fluid domain must be divided into can be in the order of several millions, meaning that sets of linear equations with several million unknowns must be solved iteratively numerous times. This procedure is repeated for each time step in unsteady simulations. With for example a time step in the order of 10^{-3} s and ten inner iterations per time step to ensure convergence, the million-unknown-sized equation set must be solved ten thousand times just to simulate one second of real time. This involves a tremendous number of floating point operations, which is impossible to do on a personal computer within a practical amount of time (given that it has enough memory in the first place). Large computer clusters are therefore used instead, with several powerful CPU's working in parallel. For this thesis, access was gained to the 'Vilje' supercomputer cluster at NTNU in Trondheim, which when introduced in 2012 was the 44^{th} most powerful computer in the world (TOP500 2014). It runs Linux, and is based on the 8-core Intel Xeon E5-2670 'Sandy Bridge' processor. The entire cluster consists of 1404 nodes with two processors per node, giving a total core count of 22 464. Each node has 32 GB of RAM, giving approximately 45 TB of total memory.

Vilje's nodes are grouped in IRU's (Individual Rack Units) of 18 nodes per IRU. Each IRU has two switches connecting nine and nine nodes together, and it is therefore advised to decompose large cases into multiples of nine nodes to ensure best performance (HPC NTNU 2015). The size of the meshes used in the following simulations made it appropriate to use nine nodes. All simulations are therefore done with 144 CPU cores and 288 GB of RAM.

5.5 Computational Domain

The rectangular computational domain is chosen on the basis of a propeller open water test tutorial in the user guide of STAR-CCM+ that introduces many best practices for such CFD simulations (CD-adapco 2015). The domain is extended $5D$ (five propeller diameters) upstream, $10D$ downstream and the total width and height are both set to $6D$.

5.6 Mesh

5.6.1 Steady State Simulations

The trimmer mesher (hexahedral dominant cells) of STAR-CCM+ has been used for the steady state simulations. Refinement regions have been defined where necessary, and the feature lines along the leading and trailing edge of the propeller have also been extracted and meshed at a very high level of refinement in order to capture the sharp geometry features here. A prism layer mesher has been used to control the boundary layer cells and $y+$ values.

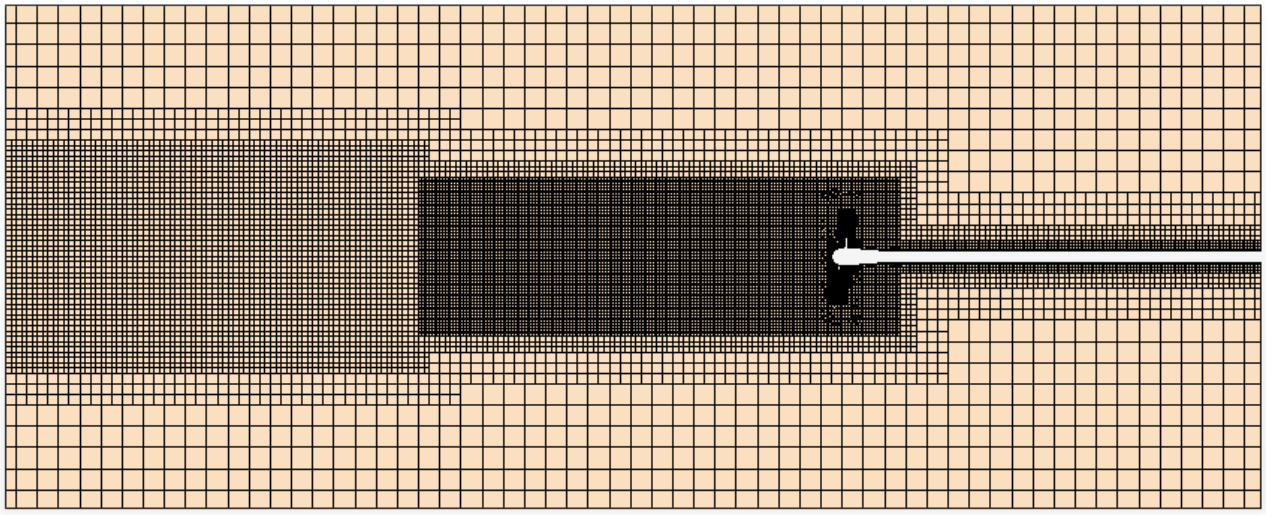

Figure 5.1: Cutting plane of the mesh of the conventional propeller seen from the side. Water inflow is from the right.

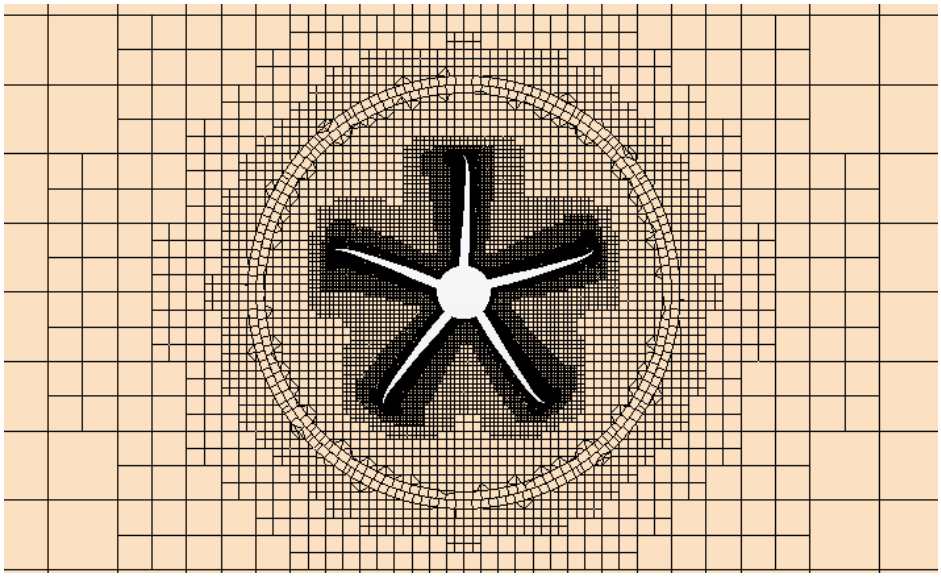

Figure 5.2: Close up cutting plane view of the mesh of the conventional propeller seen from the front. The intersection cells between the static and rotating region are also clearly visible.

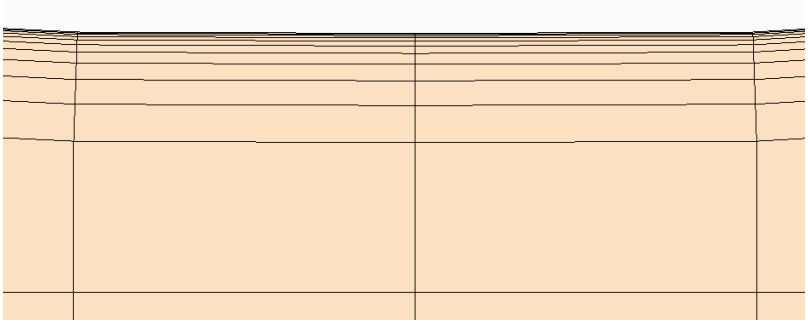

Figure 5.3: View of the prism layers near the propeller surface. A total of ten layers have been added.

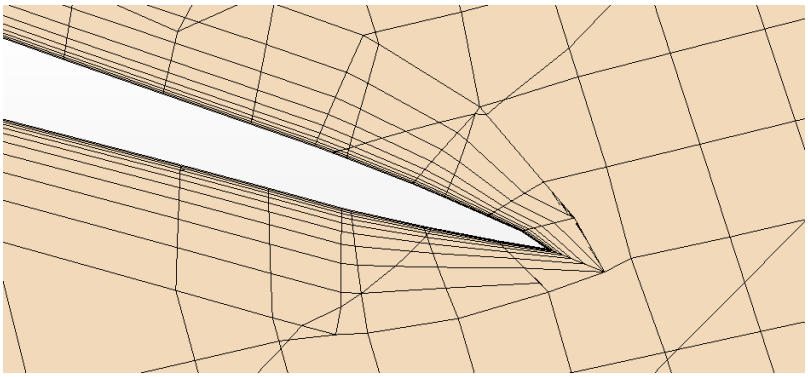

Figure 5.4: View of the mesh around the sharp trailing edge of a propeller blade.

A propeller is not a simple geometry to mesh properly. It is highly three dimensional, and consists of many sharp features. This may pose problems for the prism layers near the trailing edge, as can be seen in Figure 5.4. Some of the layers are truncated, but the mesh is also here of fair quality. The diagonal lines in the figure that seem to connect to arbitrary cells are there because of the angled orientation of the cutting plane. These lines are connected to other vertices than the ones visible.

Figure 5.1 reveals that a propeller axle has been added to the geometry. This is to ensure a nice inflow to the propeller, but also to simulate an open water test as they are done in a cavitation tunnel. This axle is not part of the rotating region, but has been assigned with a rotational wall velocity boundary condition in order to match the rotation of the propeller.

5.6.2 Unsteady Simulations

The mesh for the unsteady simulations used for the cavitation analysis is based on the one used for the steady state simulations. The same domain is used, but the cells used in this simulations are polyhedral, and not hexahedral. Such highly unstructered grids are useful for overset meshes with large displacements, and can also give quicker convergence with fewer cells (Symscape 2013). Only the short winglet variant was simulated in this way.

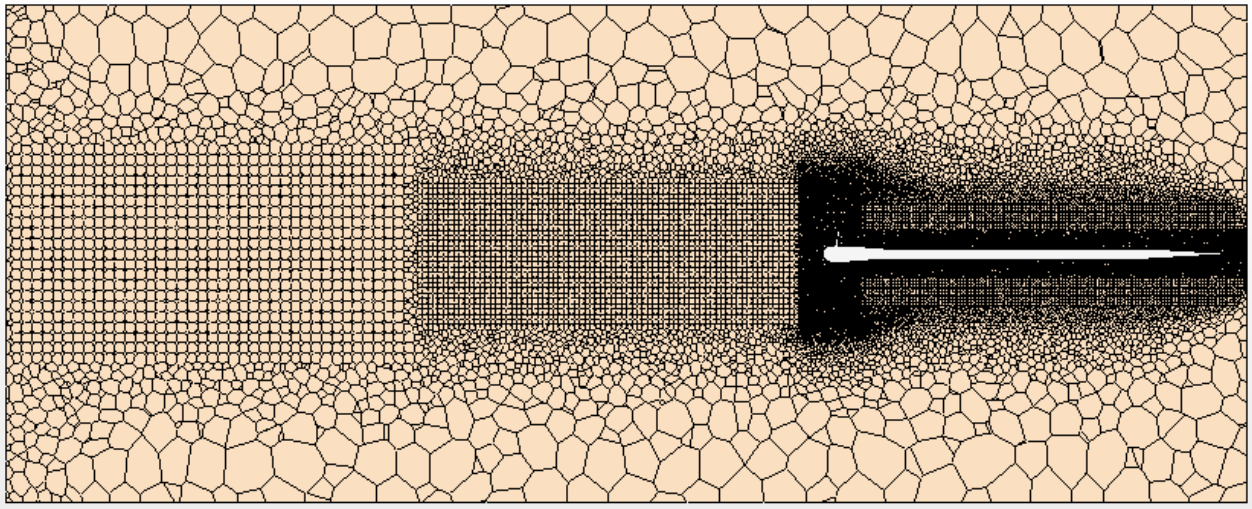

Figure 5.5: Cutting plane of the polyhedral mesh of the short winglet propeller seen from the side. Water inflow is from the right.

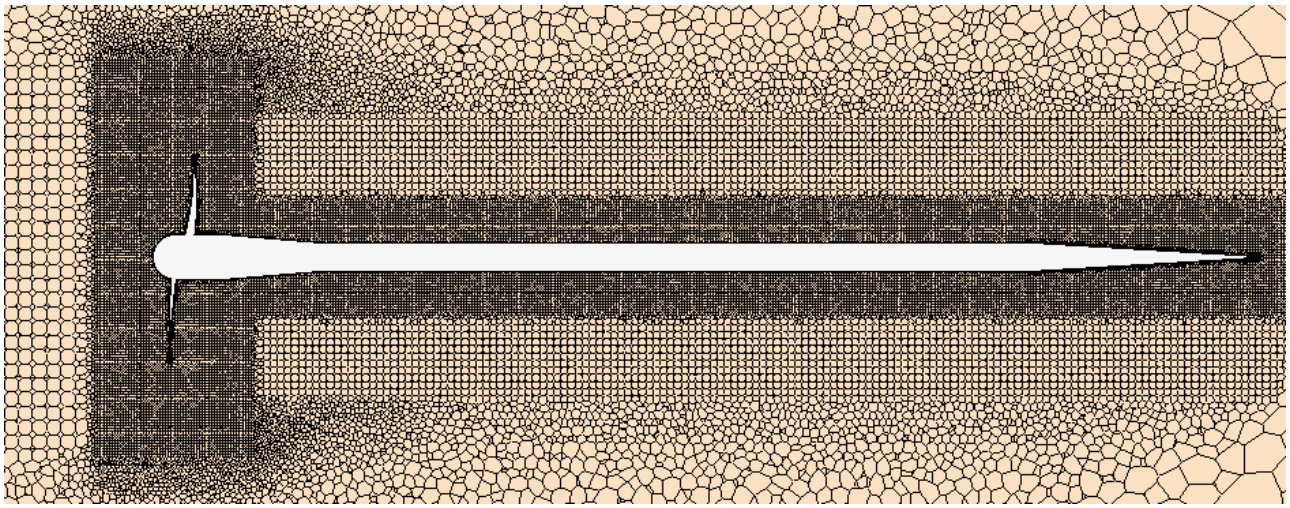

Figure 5.6: Close up cutting plane view of the polyhedral mesh of the short winglet propeller seen from the side.

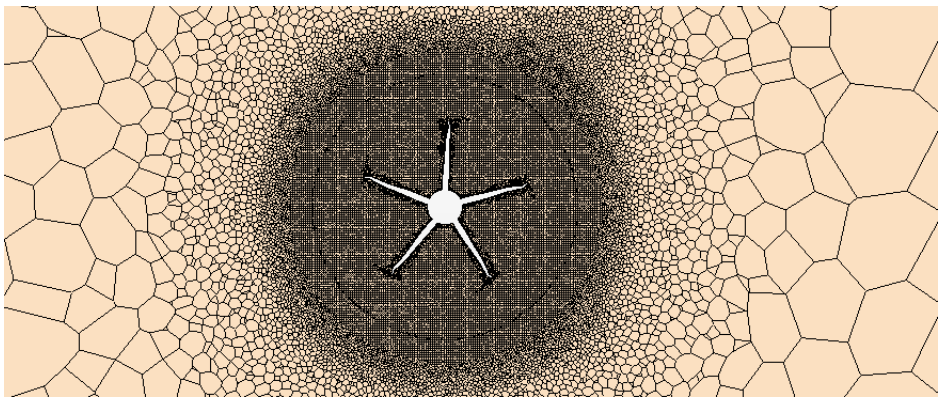

Figure 5.7: Close up cutting plane view of the polyhedral mesh of the short winglet propeller seen from the front. The boundary between the background and rotating overset region is also visible.

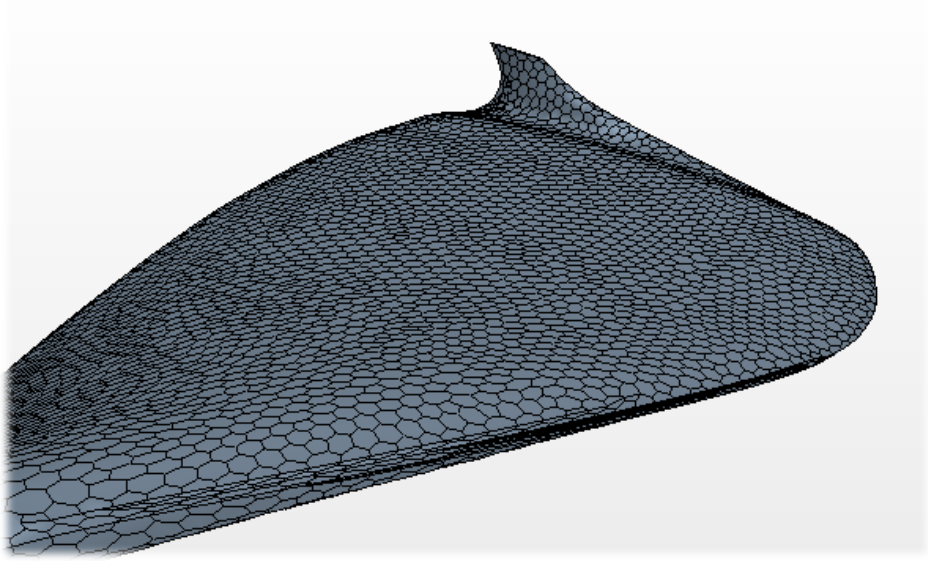

Figure 5.8: The polyhedral surface mesh of one propeller blade for the short winglet propeller.

As can be seen in Figures 5.5 and 5.6, the axle is different from the steady state simulations. This is because the entire axle now is within the rotating overset region, and an overset region should not continue all the way to a domain boundary. The axle was therefore not extended to the inlet in order to avoid an unstable simulation.

The mesh consists of even more cells than the hexahedral mesh used in the steady state simulations. The inclusion of the entire axle within the overset region was expensive in terms of number of cells. It is also important to have similar sized cells in the interface between the background and overset region in order to minimise interpolation errors. Fine cells had therefore to be used quite far away from the overset region itself.

5.6.3 Convergence Study

A test for convergence must be done in order to find what mesh resolution is necessary to ensure valid results. The mesh is made according to a base cell size, which makes it easy to scale the entire mesh by just changing one parameter. Five different base sizes are checked, with the mesh sizes as follows:

Base size	*Mesh size (#cells)*
4.00 m	289 075
2.00 m	578 403
1.00 m	1.670 million
0.50 m	4.562 million
0.25 m	15.967 million

Table 5.2: Mesh sizes for the conventional propeller geometry used in the convergence study.

It seems that the mesh does not necessarily scale by the base size factor to the third power for the coarser meshes.

The convergence study is only done for the conventional propeller, and only at advance number $J = 0.95$. It is assumed that the same mesh has converged for all other propeller geometries and advance numbers. Mesh sizes vary for the propellers, being slightly larger for the winglet equipped ones due to the more complicated geometry.

In the following figure, the percentage change in absolute value is presented for each mesh refinement level relative to the preceding level. This means that the coarsest base size of 4 m is not included, but rather used as a reference for the results of base size 2 m. For example, the propeller thrust has changed with about 3.3 % for base size 2 m compared with base size 4 m. Convergence is reached when the next refinement level has a change in results close to zero.

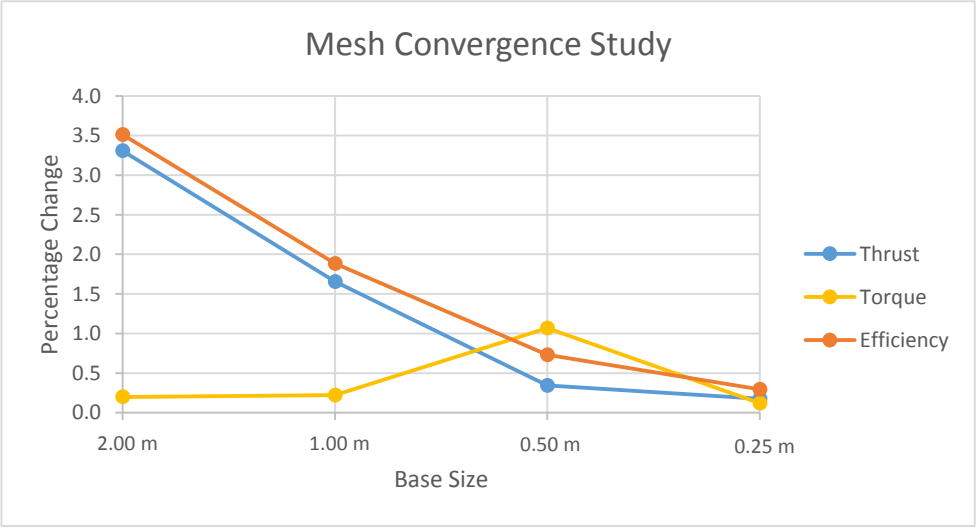

Figure 5.9: Mesh convergence study for the conventional propeller. The x-axis shows increasing level of mesh refinement.

It is clear that convergence has been reached for mesh base size 0.50 m when looking at Figure 5.9. The reason for this is that the changes in results for base size 0.25 m are much less than 0.5 % for all parameters – which for all practical purposes are zero difference.

The reason for the larger change in torque from base size 1 m to 0.5 m than for 2 m to 1 m is believed to be connected to a better resolving of the boundary layer. The $y+$ parameter has

a very high value for the coarsest meshes, making it impossible to capture the boundary layer properly. This affects the viscous drag most, which is visible through the propeller torque.

A mesh base size of 0.5 m is chosen for all simulations as it has properly converged results for all parameters. It is also this mesh that has been presented in Figures 5.1 – 5.4. The same base size was used in the polyhedral mesh which consists of 5.526 million cells. It is this mesh that is presented in Figures 5.5 – 5.8.

5.7 Simulation Procedures

5.7.1 Steady State Simulations

STAR-CCM+ allows for custom defined functions that can be used to control the simulations. This was used heavily in the steady state simulations. The advance number could for example be made dependent on the number of iterations in the following way:

$$\texttt{J = 0.2 + 0.02 * \$i} \tag{5.11}$$

where `i` is defined as follows:

$$\texttt{i = floor(\$Iteration/501)} \tag{5.12}$$

What happens in Equation 5.12 is that `i` increases by one for each 501$^{\text{st}}$ iteration. The dollar sign refers to another function, in this case `Iteration`, which is one of the standard functions in STAR-CCM+ that just keeps track of which iteration is the current. The `floor` function rounds down to the nearest integer no matter how close it is to the next – for example, `floor(1.99) = 1`.

Equation 5.11 refers to `i`, meaning that the advance number is increased by 0.02 for each 501$^{\text{st}}$ iteration. The inflow velocity can then be calculated as $\texttt{V}_\texttt{A}$ `= $J * $n * $D`, where `n` and `D` are nothing else than the propeller speed and diameter. The inflow velocity boundary condition can then be set to $\texttt{\$V}_\texttt{A}$, making the inflow to change automatically according to the current advance number as the simulation proceeds.

By specifying STAR-CCM+ to extract the thrust and torque from the propeller, the K_T and K_Q coefficients, as well as the efficiency η can be defined in much the same way. These parameters can then be plotted for each 500$^{\text{th}}$ iteration, yielding the latest result of the current advance number before the next one is introduced at the next iteration. It is then just to start the simulation, and the total open water diagram is eventually plotted automatically.

This is exactly the way the steady state simulations are done. Starting at $J = 0.2$ and running through to $J = 1.3$ with increments of 0.02 and 500 iterations per advance number. This gives in total 56 different advance numbers and 28 000 iterations for each complete open water test. The finished open water diagram can be extracted right after the simulation is complete by setting the stopping criteria to 28 000 iterations.

500 iterations per time step ensured convergence both for residuals and forces. The residuals for the first 3500 iterations for the conventional propeller open water test are as follows:

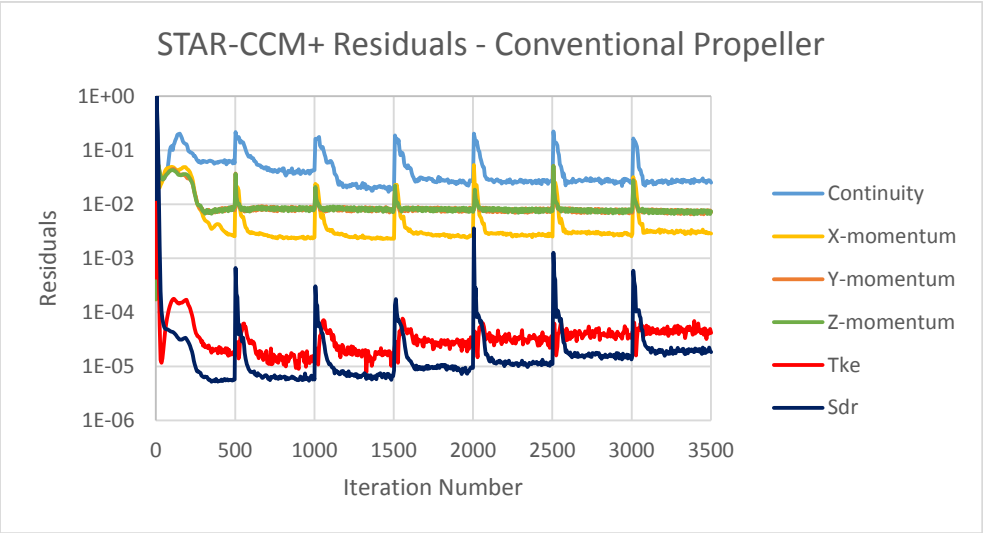

Figure 5.10: The residuals from STAR-CCM+ for the conventional propeller open water test.

'Tke' and 'Sdr' in Figure 5.10 above are related to the turbulence model.

The cavitation analysis is simplified in the steady state simulations. Gravity effects are not included, so the change in hydrostatic pressure is not accounted for. This means that the cavitation extension only can be represented correctly at one blade section. The reference pressure inside STAR-CCM+ must be altered in order to have the correct pressure at the wanted submergence. The propeller hub is located 6.68 m below the water surface, and the worst case submergence in terms of cavitation is this submergence plus the propeller radius ($D/2 = 3.95$ m). 3.90 m was chosen, so to not be positioned exactly at the propeller tip. The water column above this position is of height 6.68 m $-$ 3.90 m $=$ 2.78 m. By adding the pressure from this water column to the atmospheric reference pressure, and also subtracting the vapour pressure of 1500 Pa, cavitation is likely to occur if the absolute pressure on the propeller blade drops below zero. This is, as already mentioned, only correct at the blade portion which is located at exactly 3.90 m radial position, meaning that a conservative estimate of the cavitation sheet is made elsewhere.

Each open water test took on average a little less than three hours to finish with nine nodes at the Vilje cluster.

5.7.2 Unsteady Simulations

It was decided that a cavitation check that included transient effects should be done – both to validate the steady state results and to see the effects of the hydrostatic pressure. Only the short winglet propeller was subject to the unsteady simulations, and at advance numbers $J = 0.2$, 0.6 and 0.95. As already mentioned in Chapter 5.3.2, the time step equalled 1° of rotation, and the total number of complete propeller revolutions was ten. This ensured a properly developed wake field and nicely converged cavitation results.

Ten inner iterations per time step, 360 time steps per complete propeller revolution and a total of ten revolutions results in 36 000 iterations just for one single advance number – compared with only 500 for the steady state simulations. The total computation time was on average 30 hours for each case with nine nodes at the Vilje cluster. For the sake of argument: A full open water test done in this way with the same resolution as the steady state simulations (56 advance numbers) would require ten weeks of non-stop computation time at a supercomputer. It is now obvious why unsteady simulations are extremely costly compared with steady state simulations – and it is clear why they were avoided as much as possible.

It should be noted that some computation time could be saved by not writing images for each time step. However, the cavitation pattern images was in this case the key results and had to be included.

The cavitation simulations here include the hydrostatic pressure, meaning that the dynamic behaviour of the cavitation pattern can be captured since the propeller is physically moving. Cavitation is likely to occur where the absolute pressure drops below zero by again subtracting the vapour pressure of 1500 Pa from the atmospheric reference pressure. There is no need to correct for the free surface since it already is properly modelled.

Chapter 6

Results

The CFD results are presented in the following chapter without much discussion. The detailed discussion takes place in Chapter 7.

6.1 Steady State Simulations

6.1.1 Open Water Tests

Conventional Propeller

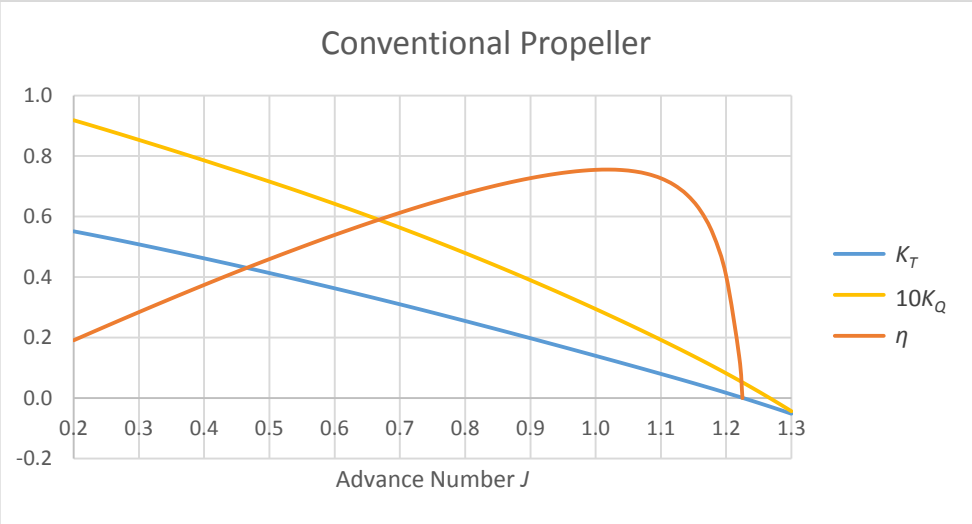

Figure 6.1: Open water diagram for the conventional propeller. $\eta_{\max} = 75.5$ % at $J = 1.02$.

Tip Loaded Propeller

The tip loaded propeller is also included, to see what its characteristics are without the winglets.

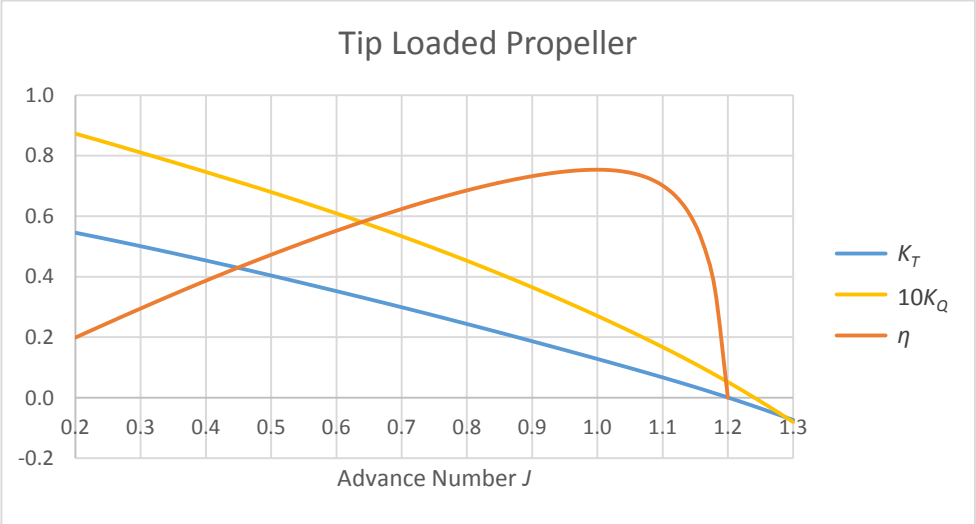

Figure 6.2: Open water diagram for the tip loaded propeller. $\eta_{\max} = 75.4$ % at $J = 1.00$.

Tall Winglet Propeller

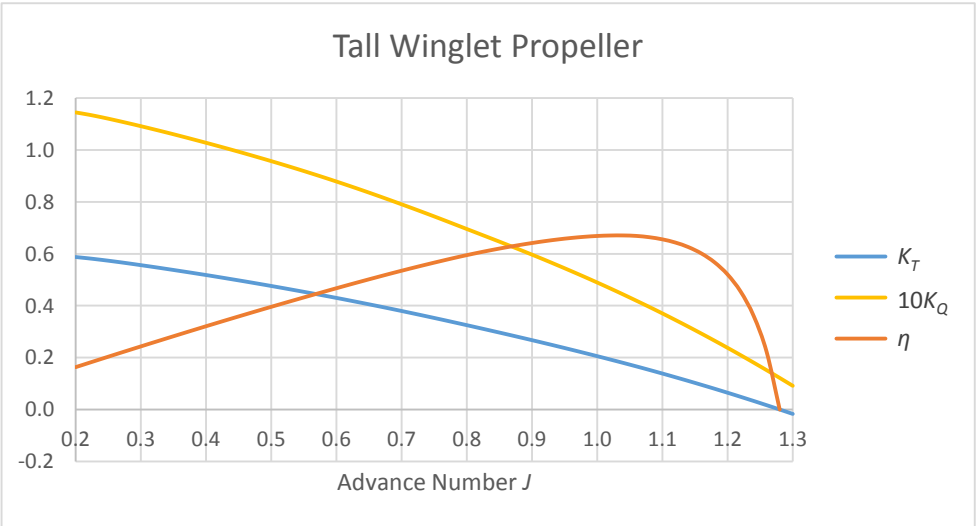

Figure 6.3: Open water diagram for the tall winglet propeller. $\eta_{\max} = 67.1$ % at $J = 1.04$.

Short Winglet Propeller

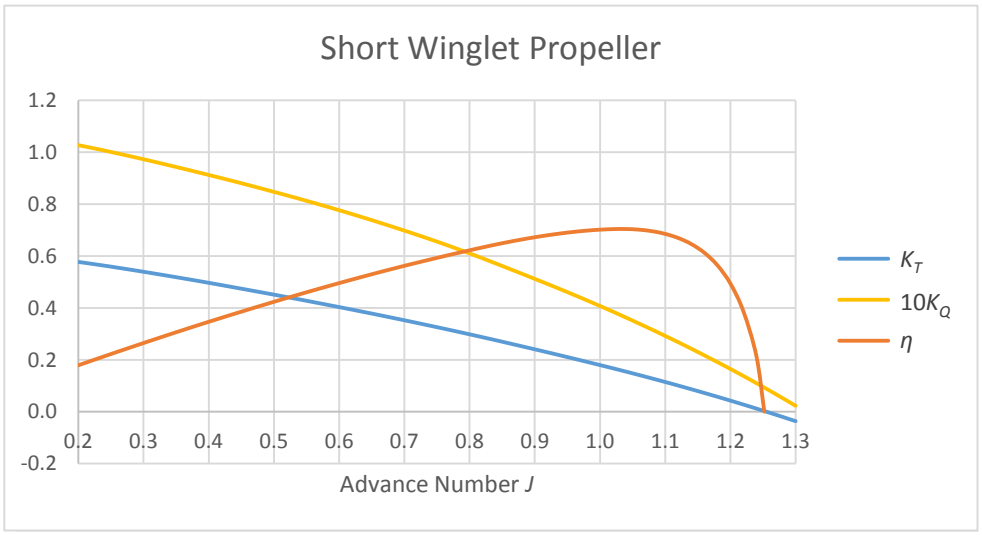

Figure 6.4: Open water diagram for the short winglet propeller. $\eta_{\max} = 70.4\ \%$ at $J = 1.04$.

Combined Plots of Open Water Results

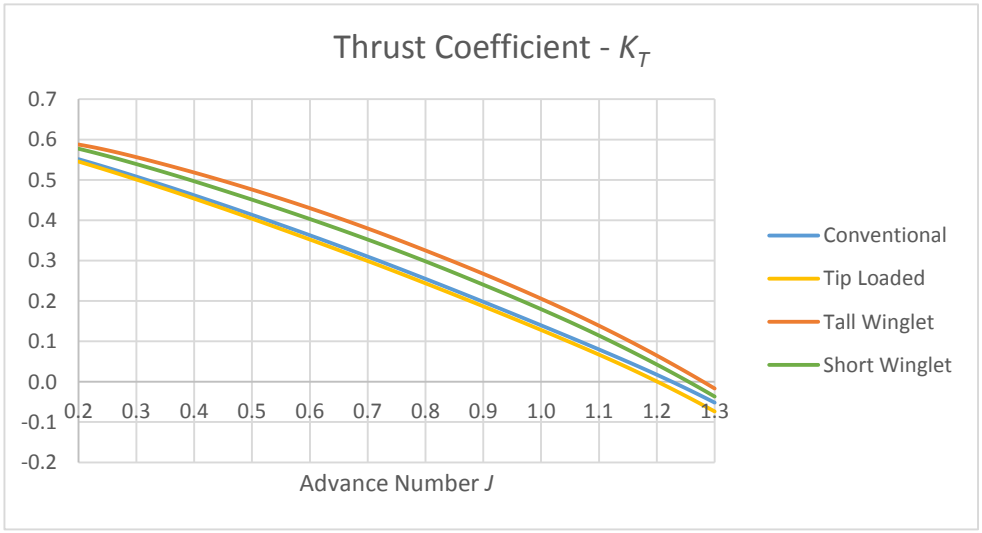

Figure 6.5: Thrust coefficients for all the propellers.

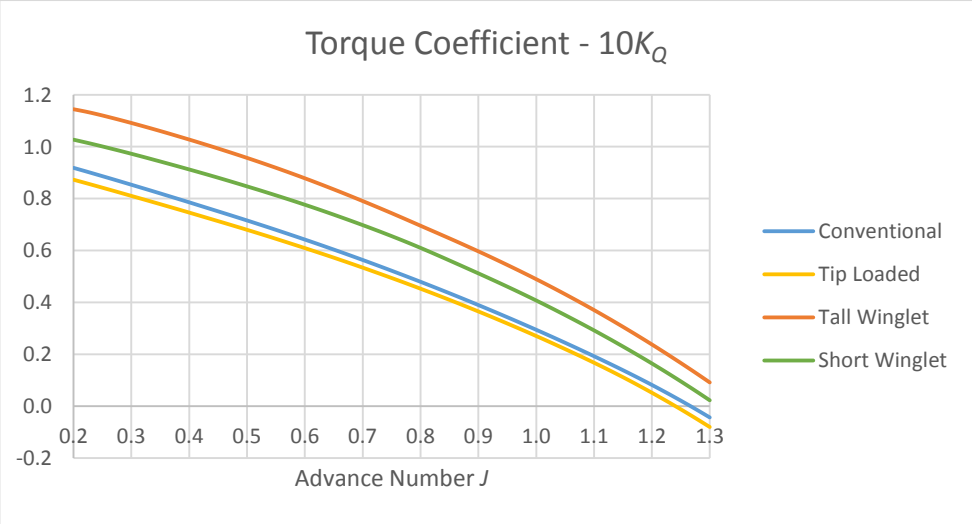

Figure 6.6: Torque coefficients for all the propellers.

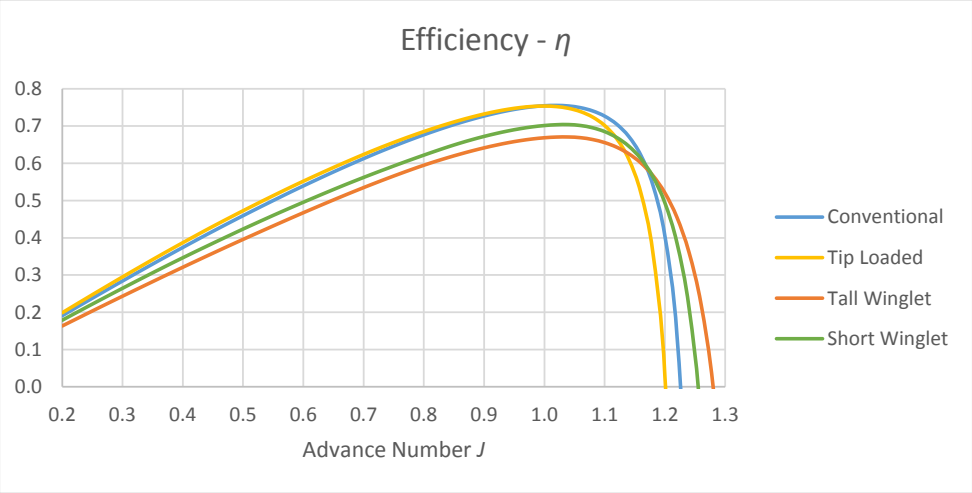

Figure 6.7: Efficiencies for all the propellers.

Summary of Results for $J = 0.95$

Co-supervisor Professor Sverre Steen pointed out that the desired operating point for a propeller is slightly to the left of the optimum efficiency. It is desirable to be located a bit further away from the steep reduction in the efficiency curve that occurs to the right of the optimum point. The propeller loading is far from perfectly constant under real conditions, so a drop in the RPM could potentially reduce the efficiency a lot – which is good to avoid. An advance number of $J = 0.95$ has been selected as the design propulsion point for all the propellers. The results for this advance number are summarised in the following tables:

Propeller	K_T	$10K_Q$	T	Q	η
Conventional	0.169	0.343	1.95 MN	3.12 MNm	74.5 %
Tip loaded	0.158	0.319	1.82 MN	2.90 MNm	74.7 %
Tall winglet	0.237	0.544	2.73 MN	4.96 MNm	65.8 %
Short winglet	0.210	0.461	2.43 MN	4.20 MNm	69.0 %

Table 6.1: Results for $J = 0.95$ for all the propellers.

Parameter	*Tip loaded*	*Tall winglet*	*Short winglet*
K_T	-6.7 %	40.3 %	24.5 %
$10K_Q$	-7.1 %	58.8 %	34.4 %
η	0.2 p.p	-8.7 p.p	-5.5 p.p

Table 6.2: Deviations from the conventional propeller at $J = 0.95$. The values for η are given in percentage points.

Summary of Relative Differences from the Conventional Propeller

The figures below show the difference of the winglet propellers relative to the conventional design for advance numbers J between 0.2 and 1.1 (relative differences are uninteresting and at worst misleading above $J = 1.1$):

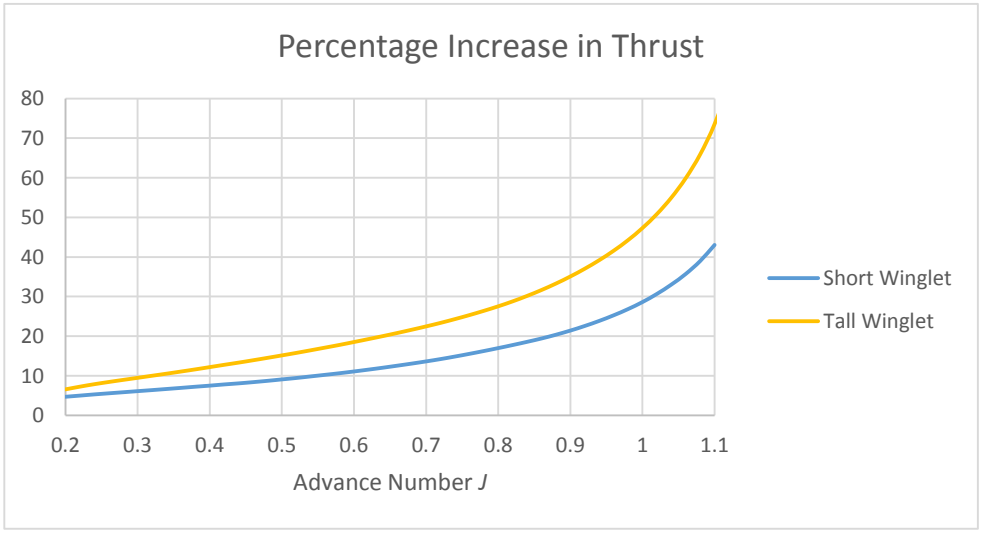

Figure 6.8: Percentage increase in thrust relative to the conventional propeller.

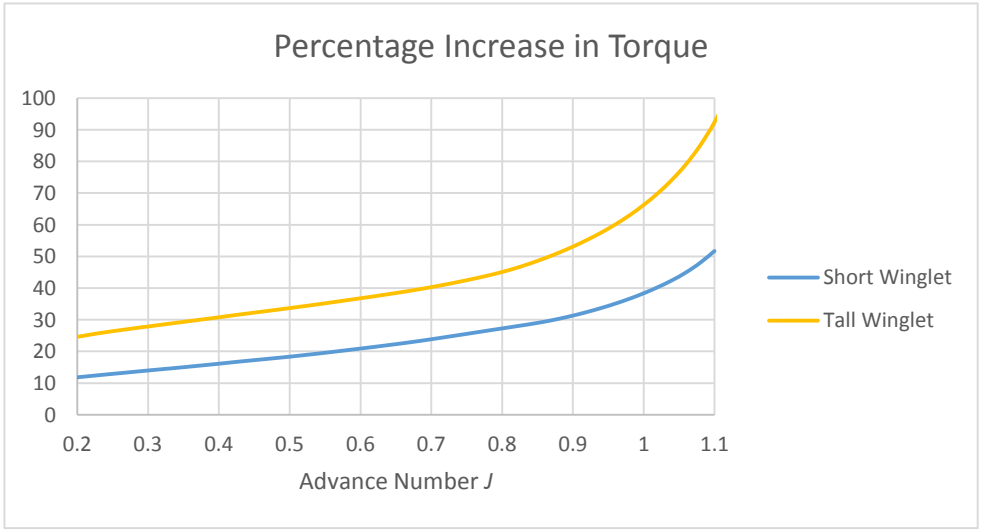

Figure 6.9: Percentage increase in torque relative to the conventional propeller.

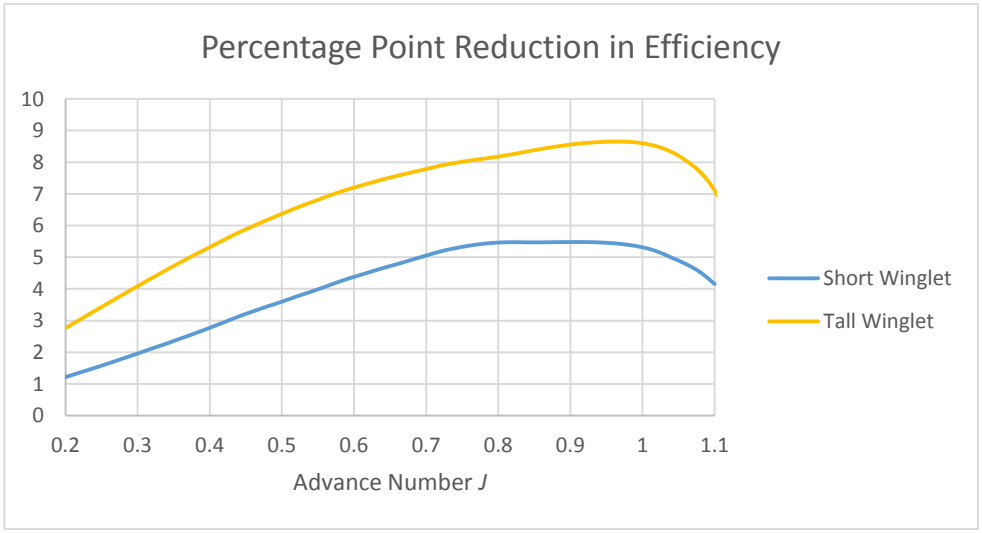

Figure 6.10: Percentage point reduction in efficiency relative to the conventional propeller.

6.1.2 Wake Streamlines

The wake streamlines in the figures below are coloured with the velocity magnitude of the flow field, and the propellers are visualised with the pressure field.

Advance Number $J = 0.20$

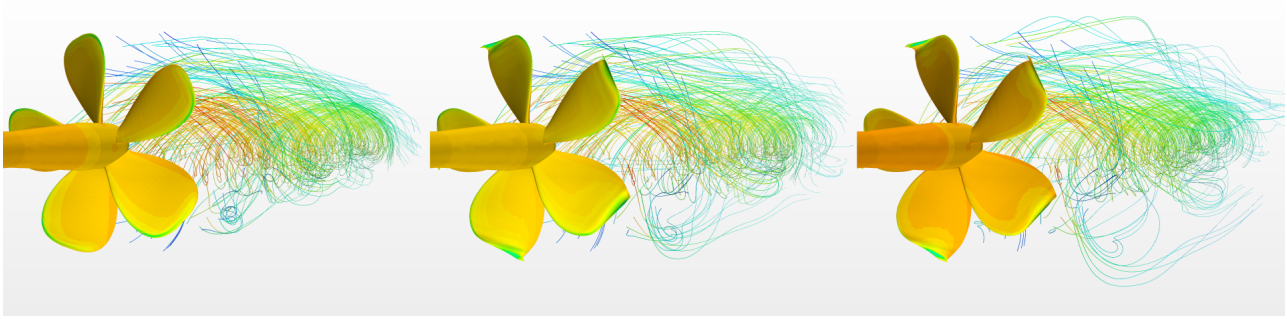

Figure 6.11: Wake streamlines for the conventional, short and tall winglet propellers for advance number $J = 0.20$.

Advance Number $J = 0.60$

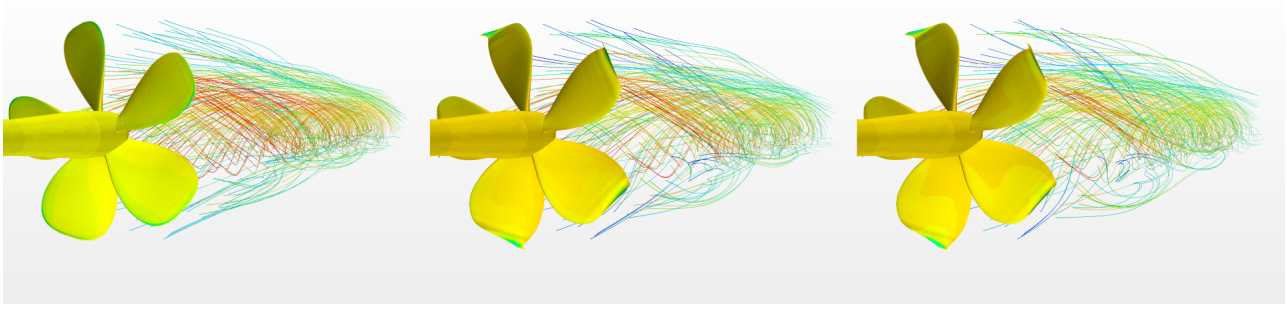

Figure 6.12: Wake streamlines for the conventional, short and tall winglet propellers for advance number $J = 0.60$.

Advance Number $J = 0.95$

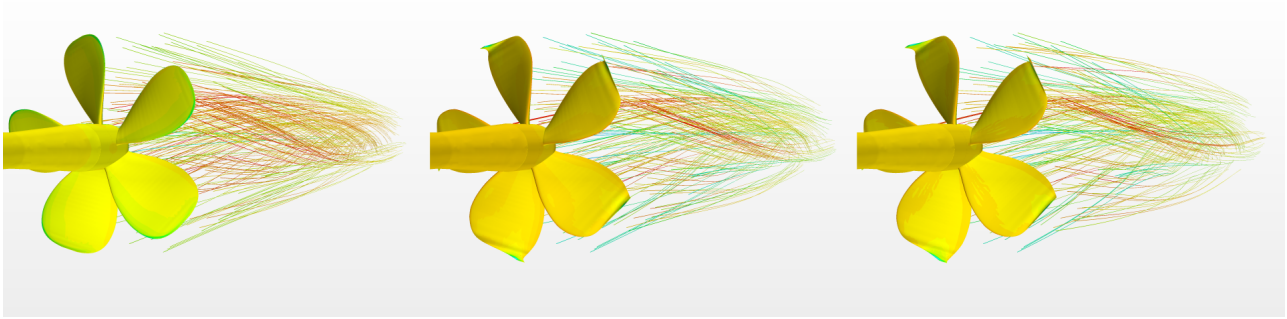

Figure 6.13: Wake streamlines for the conventional, short and tall winglet propellers for advance number $J = 0.95$.

Advance Number $J = 1.20$

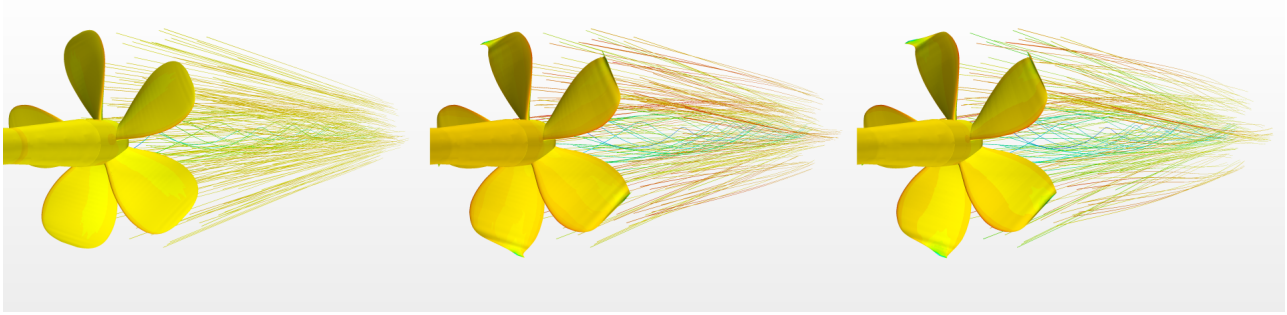

Figure 6.14: Wake streamlines for the conventional, short and tall winglet propellers for advance number $J = 1.20$.

6.1.3 Cavitation

Advance Number $J = 0.20$

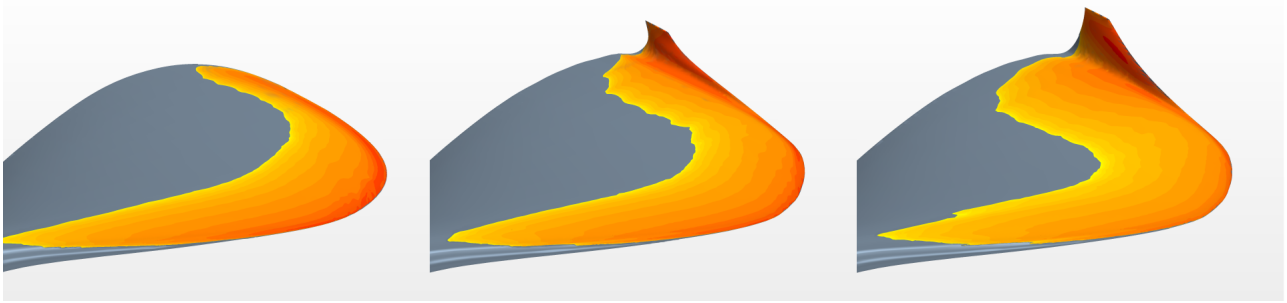

Figure 6.15: Cavitation sheets for the conventional, short and tall winglet propellers for advance number $J = 0.20$.

Advance Number $J = 0.60$

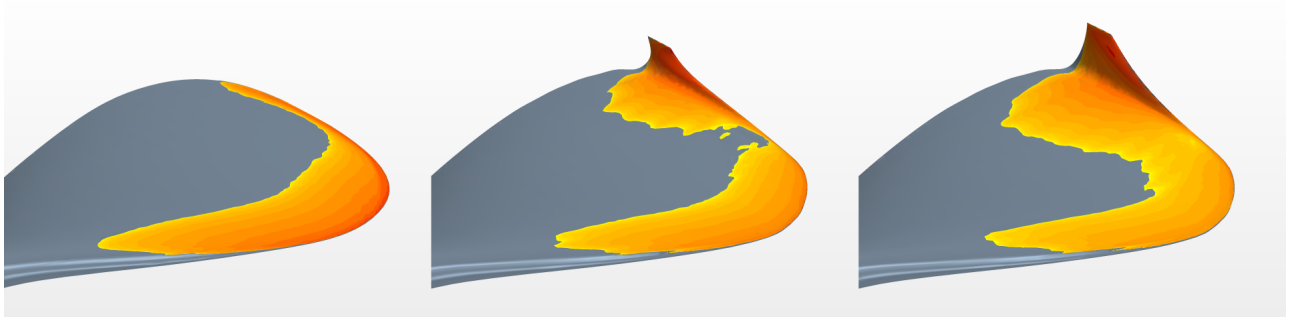

Figure 6.16: Cavitation sheets for the conventional, short and tall winglet propellers for advance number $J = 0.60$.

Advance Number $J = 0.95$

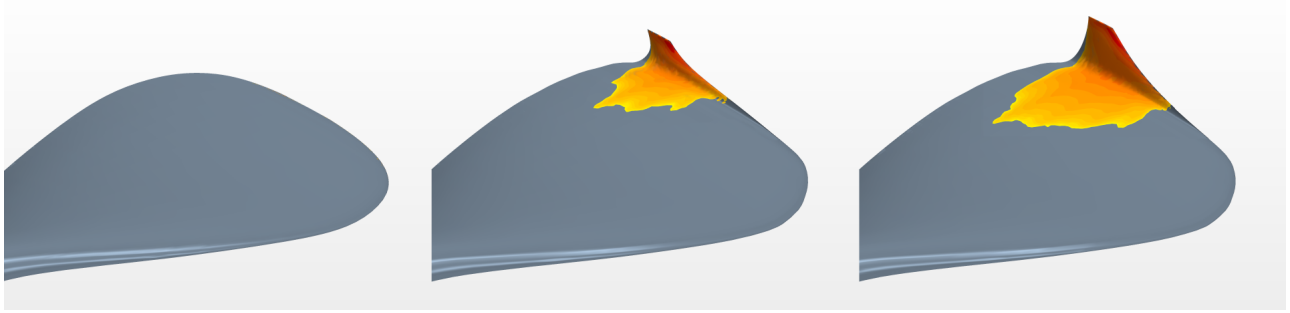

Figure 6.17: Cavitation sheets for the conventional, short and tall winglet propellers for advance number $J = 0.95$.

Advance Number $J = 1.20$

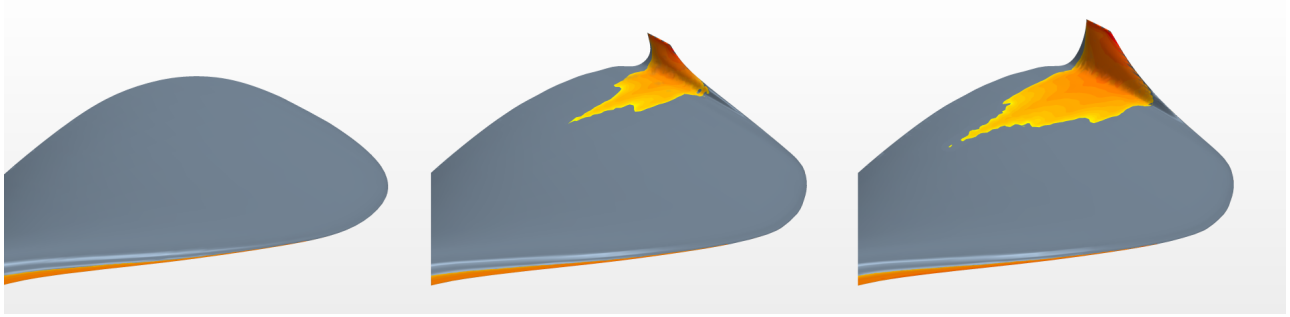

Figure 6.18: Cavitation sheets for the conventional, short and tall winglet propellers for advance number $J = 1.20$. Pressure side cavitation is also present.

6.1.4 Wake Vorticity

The vorticity in the wake have been visualised by the Q-Criterion technique and with cutting planes at distances of $0.5D$, $1D$ and $2D$ behind the propeller. This is to keep track of the tip vortices and to find their magnitudes and directions. Only $J = 0.95$ have been checked, except for one case where similarity in the K_T coefficient was analysed.

The vorticity magnitude is presented, as well as the axial component and the component normal to the axial one.

A three dimensional vorticity field will have components in all spatial directions, but each vortex can be decomposed into three components, with the components' rotational directions specified by a vector and the right hand rule.

The vorticity magnitude shows the total absolute value of all the components, and is therefore a measure of the total vorticity, but information about the direction of spin is lost. The axial component have its positive vector pointed along the propeller axle, i.e into the plane, and will therefore show vortices in the plane, with positive values spinning clockwise and negative values spinning counter clockwise. The component normal to the axial one has its positive vector pointed to the left, meaning that the vortices are spinning into (and out of) the plane. The idea is that this is the vorticity component induced by the pressure leakage between the high pressure side and suction side of the propeller blades. Only the blades at positions perpendicular to the direction vector are able to give any contribution to this component, meaning that the vertically positioned blades are the most visible. The other blades will have more of their contribution in the upwards pointing component, but would actually only show just about the same vorticity decomposed in another way. One of these components are therefore sufficient to see the interesting effects of vortices into the plane.

A distance of two diameters behind the propeller is quite far, meaning that a roll up of the vortices can be expected.

The Q-Criterion figures show the three dimensional vortices up to a certain strength, determined by a selected value. The vortices continue much further in the wake, but are not shown that far because of figure cluttering.

Conventional Propeller

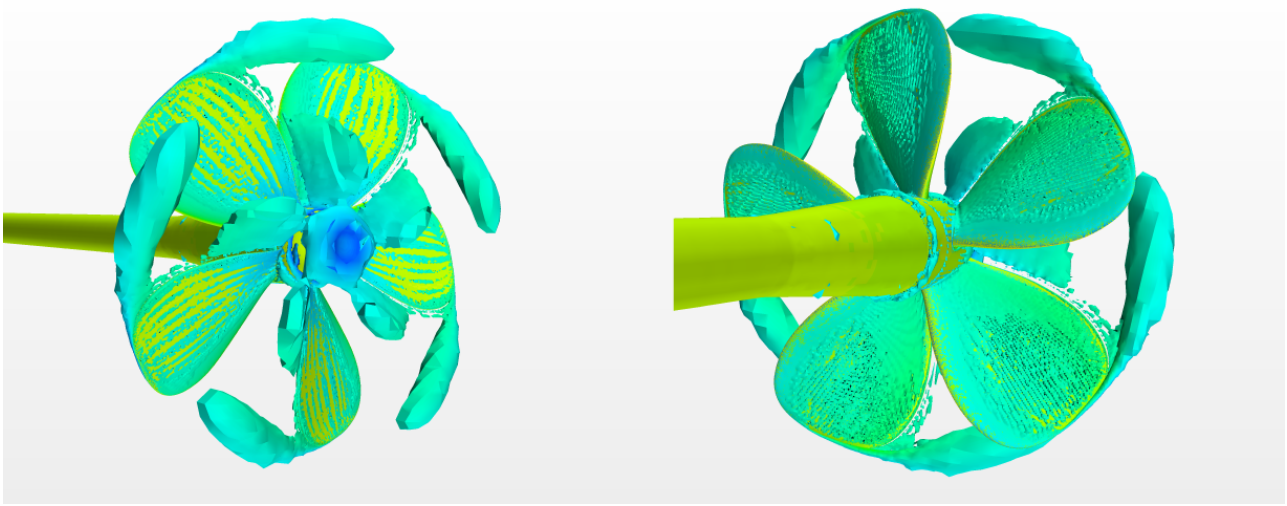

Figure 6.19: The Q-Criterion isosurfaces for a value of 10 s^{-2} for the conventional propeller.

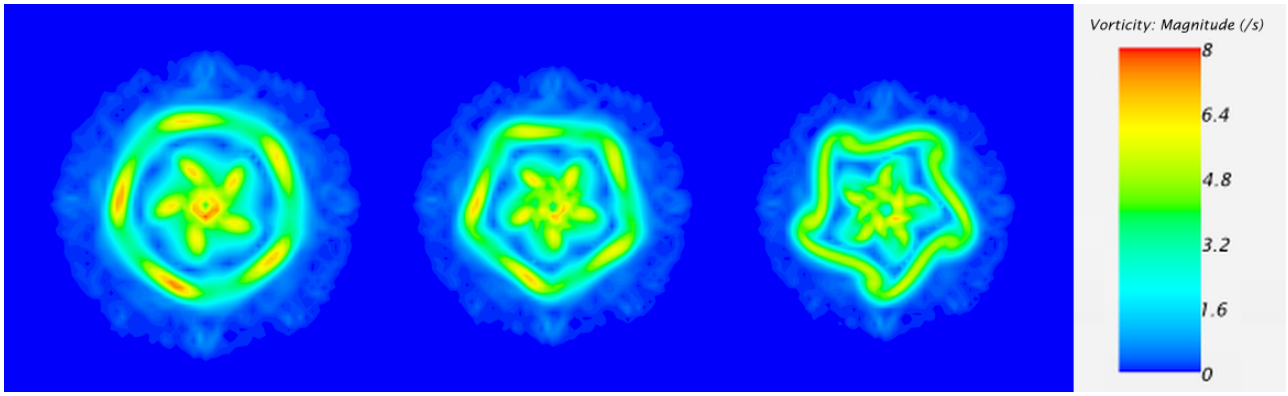

Figure 6.20: The wake vorticity magnitude for the conventional propeller. The planes are, from left to right, located at distances of $0.5D$, $1D$ and $2D$ behind the propeller.

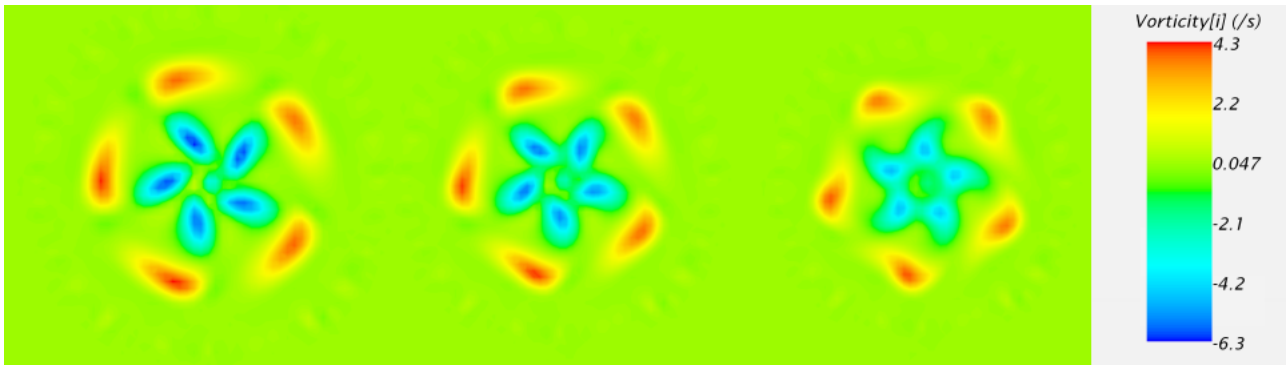

Figure 6.21: The axial wake vorticity component (positive direction for the vector is into the plane) for the conventional propeller. The planes are, from left to right, located at distances of $0.5D$, $1D$ and $2D$ behind the propeller. Red colour is clockwise, blue is anti clockwise.

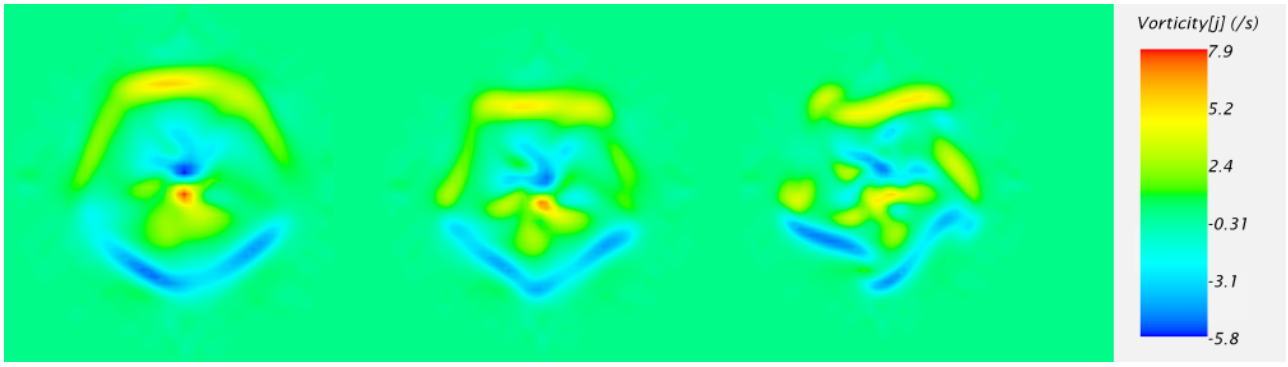

Figure 6.22: The wake vorticity normal to the axial component (positive direction for the vector is to the left) for the conventional propeller. The planes are, from left to right, located at distances of $0.5D$, $1D$ and $2D$ behind the propeller. Red colour is clockwise, blue is anti clockwise – but be sure to remember the right hand rule, implying that the vorticity really is into the plane.

Tip Loaded Propeller

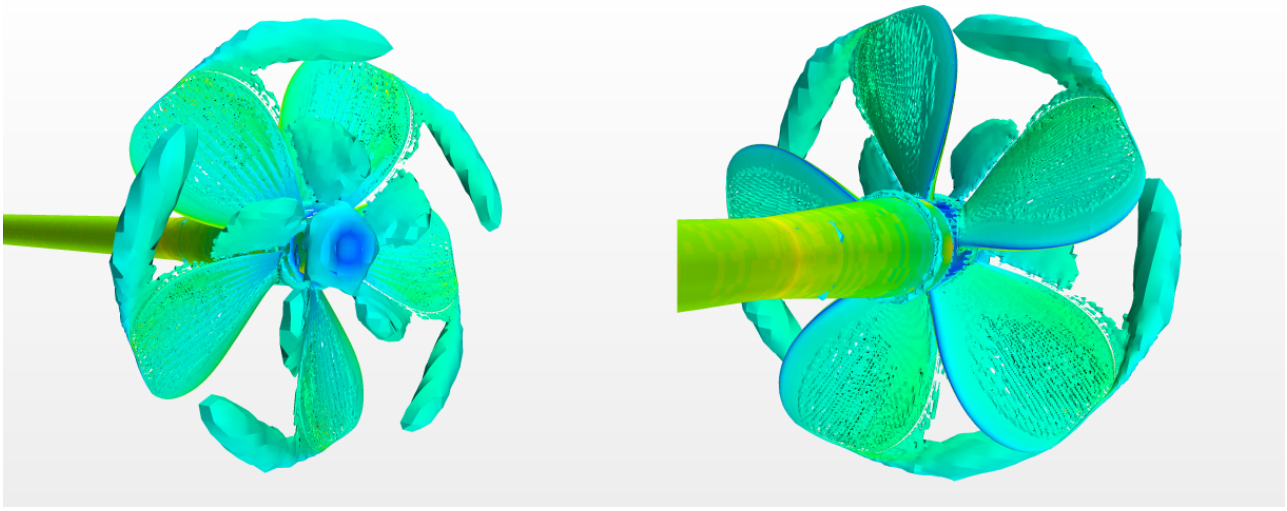

Figure 6.23: The Q-Criterion isosurfaces for a value of 10 s^{-2} for the tip loaded propeller.

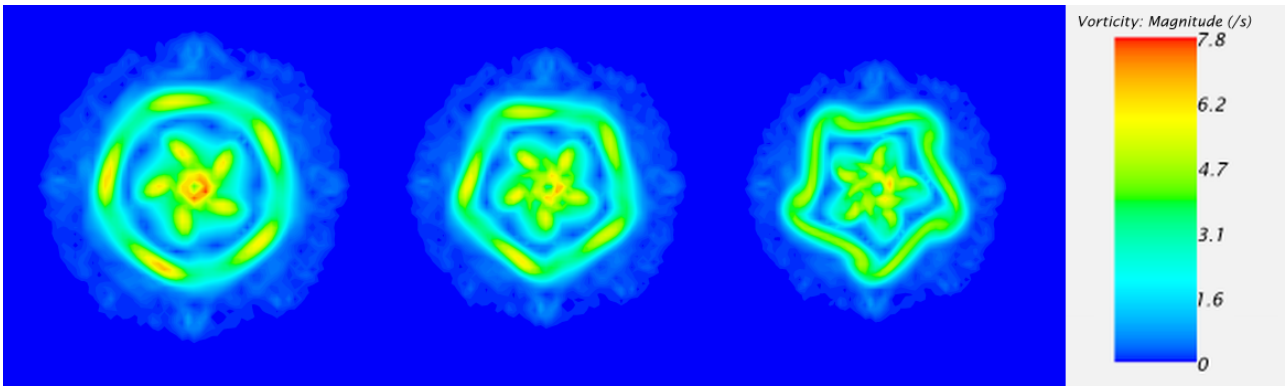

Figure 6.24: The wake vorticity magnitude for the tip loaded propeller. The planes are, from left to right, located at distances of $0.5D$, $1D$ and $2D$ behind the propeller.

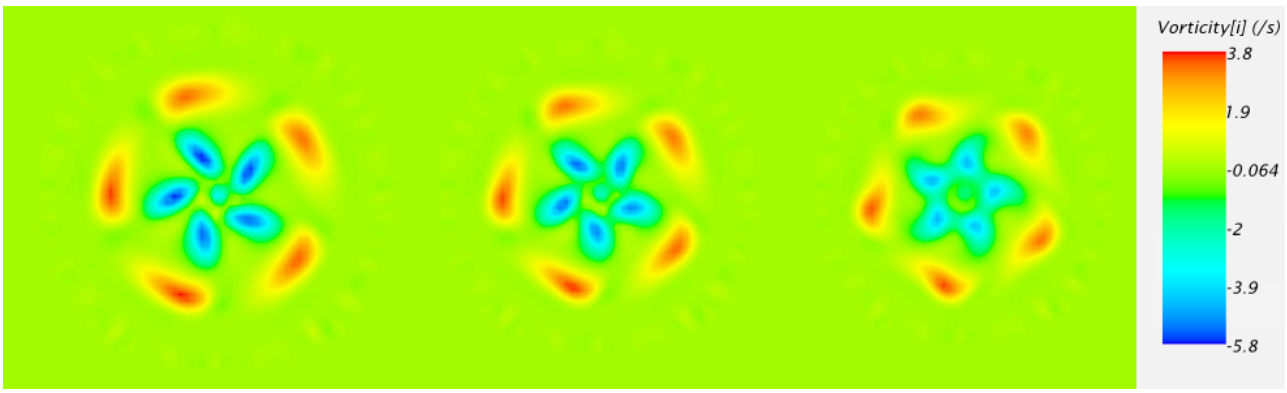

Figure 6.25: The axial wake vorticity component (positive direction for the vector is into the plane) for the tip loaded propeller. The planes are, from left to right, located at distances of $0.5D$, $1D$ and $2D$ behind the propeller. Red colour is clockwise, blue is anti clockwise.

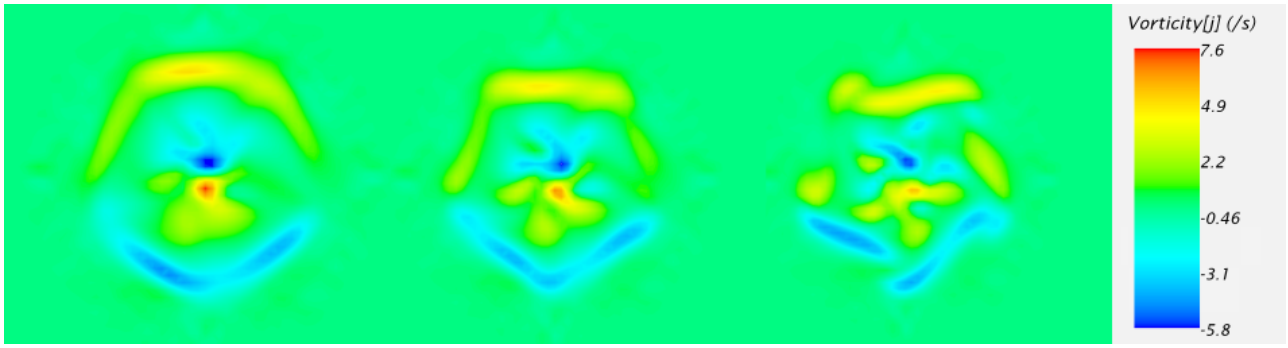

Figure 6.26: The wake vorticity normal to the axial component (positive direction for the vector is to the left) for the tip loaded propeller. The planes are, from left to right, located at distances of $0.5D$, $1D$ and $2D$ behind the propeller. Red colour is clockwise, blue is anti clockwise – but be sure to remember the right hand rule, implying that the vorticity really is into the plane.

Tall Winglet Propeller

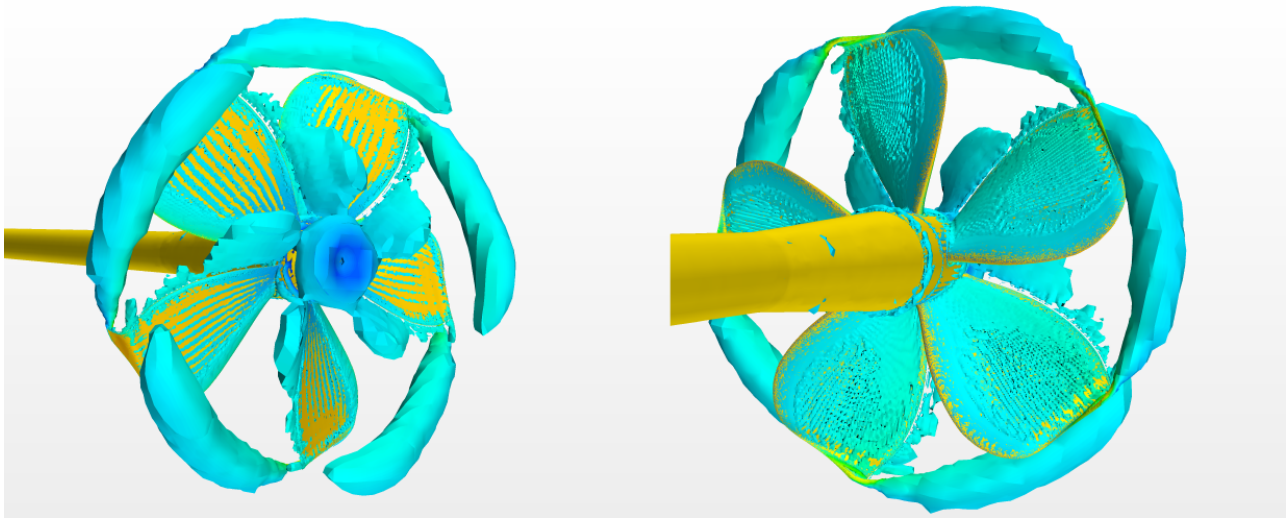

Figure 6.27: The Q-Criterion isosurfaces for a value of 10 s^{-2} for the tall winglet propeller.

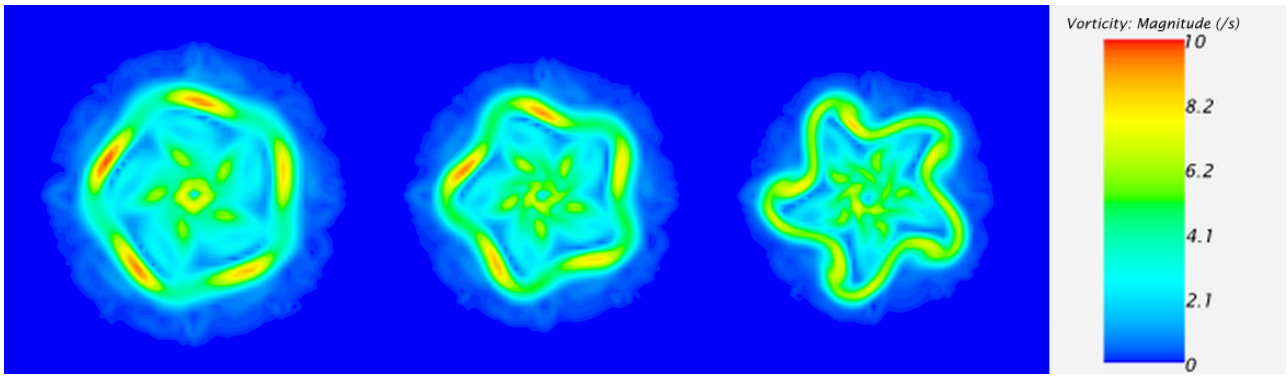

Figure 6.28: The wake vorticity magnitude for the tall winglet propeller. The planes are, from left to right, located at distances of $0.5D$, $1D$ and $2D$ behind the propeller.

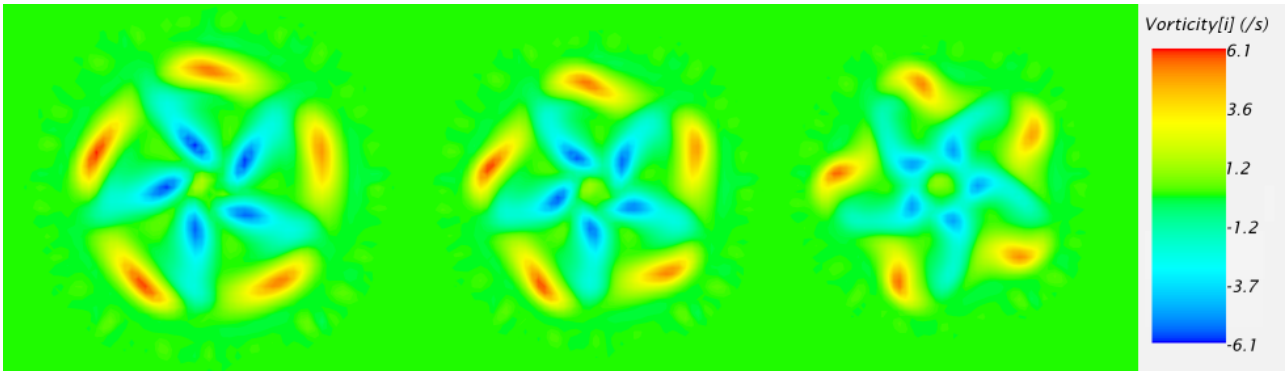

Figure 6.29: The axial wake vorticity component (positive direction for the vector is into the plane) for the tall winglet propeller. The planes are, from left to right, located at distances of $0.5D$, $1D$ and $2D$ behind the propeller. Red colour is clockwise, blue is anti clockwise.

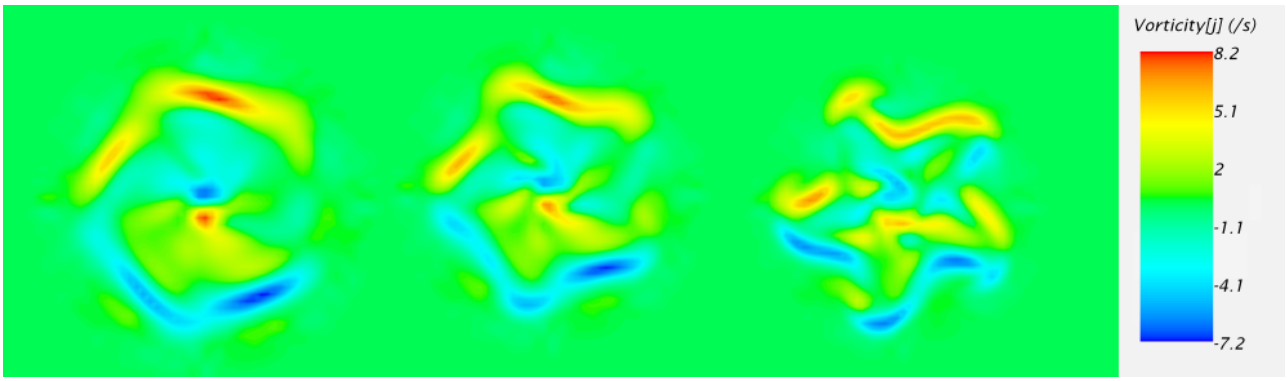

Figure 6.30: The wake vorticity normal to the axial component (positive direction for the vector is to the left) for the tall winglet propeller. The planes are, from left to right, located at distances of $0.5D$, $1D$ and $2D$ behind the propeller. Red colour is clockwise, blue is anti clockwise – but be sure to remember the right hand rule, implying that the vorticity really is into the plane.

Short Winglet Propeller

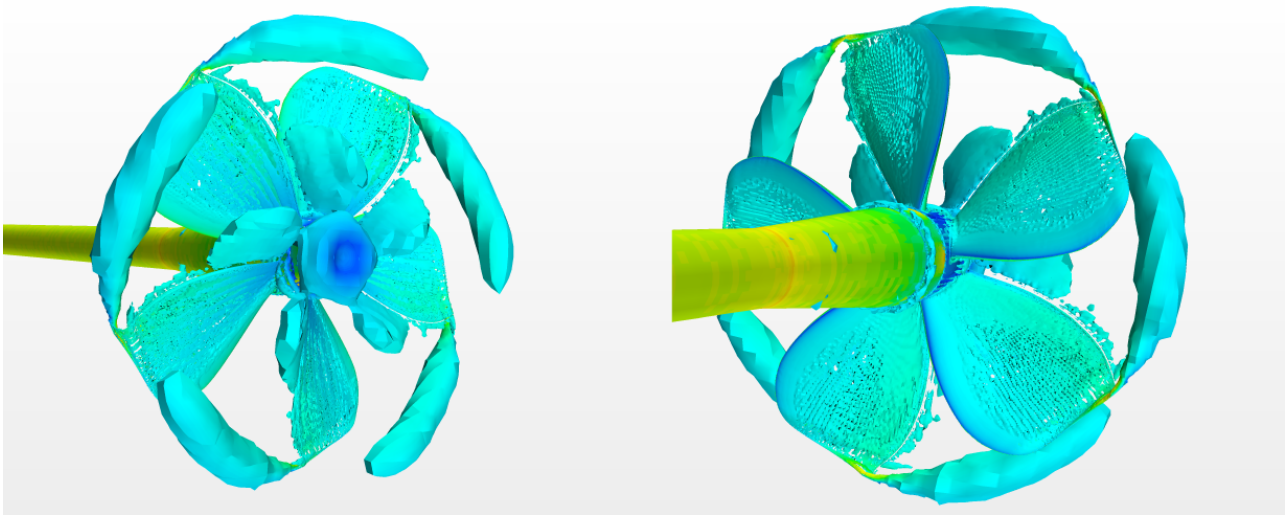

Figure 6.31: The Q-Criterion isosurfaces for a value of 10 s^{-2} for the short winglet propeller.

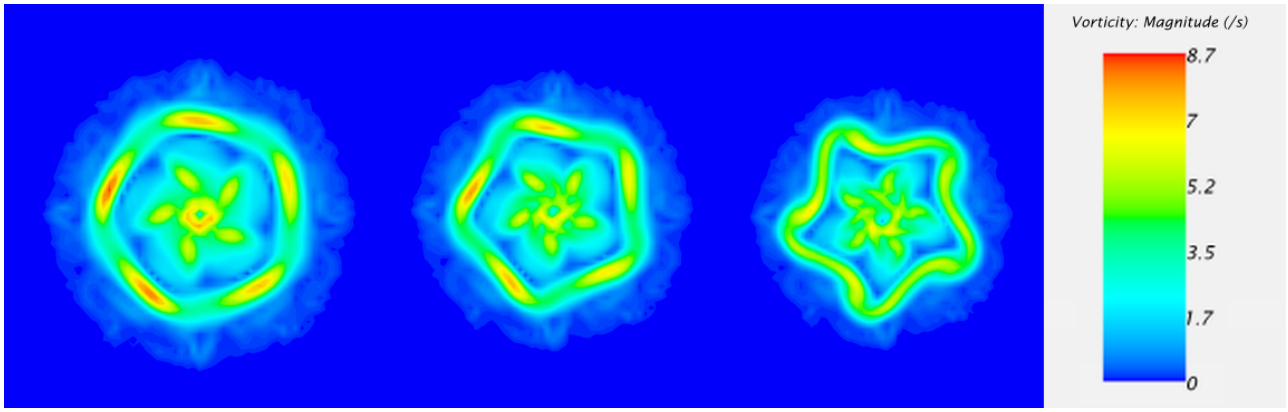

Figure 6.32: The wake vorticity magnitude for the short winglet propeller. The planes are, from left to right, located at distances of $0.5D$, $1D$ and $2D$ behind the propeller.

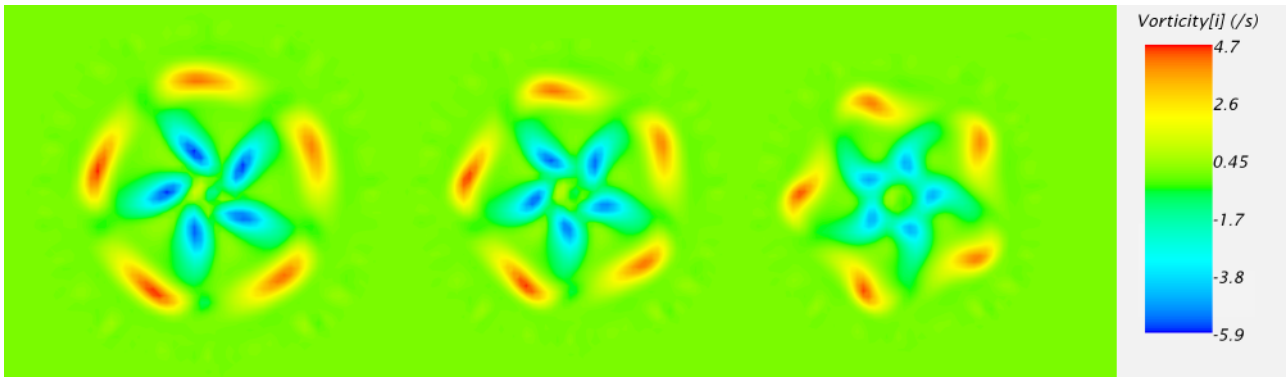

Figure 6.33: The axial wake vorticity component (positive direction for the vector is into the plane) for the short winglet propeller. The planes are, from left to right, located at distances of $0.5D$, $1D$ and $2D$ behind the propeller. Red colour is clockwise, blue is anti clockwise.

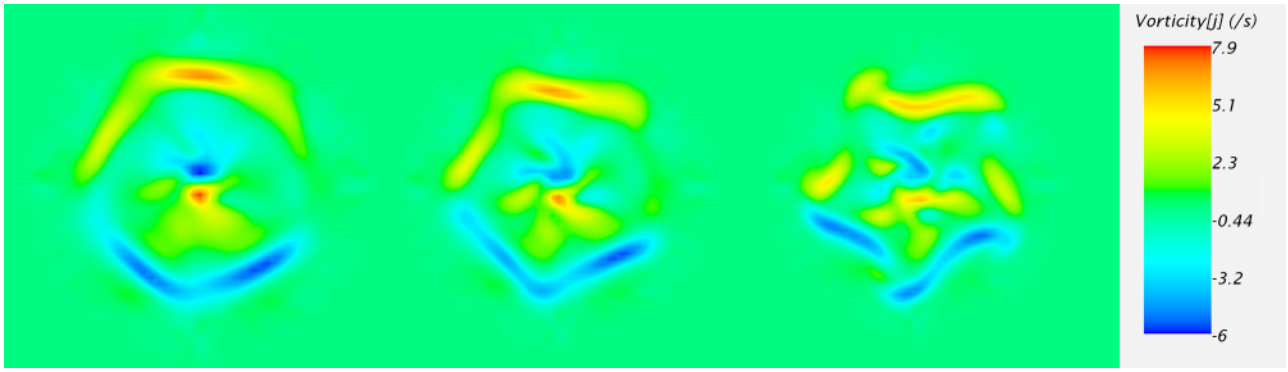

Figure 6.34: The wake vorticity normal to the axial component (positive direction for the vector is to the left) for the short winglet propeller. The planes are, from left to right, located at distances of $0.5D$, $1D$ and $2D$ behind the propeller. Red colour is clockwise, blue is anti clockwise – but be sure to remember the right hand rule, implying that the vorticity really is into the plane.

Closeup View of the Winglets: Q-Criterion

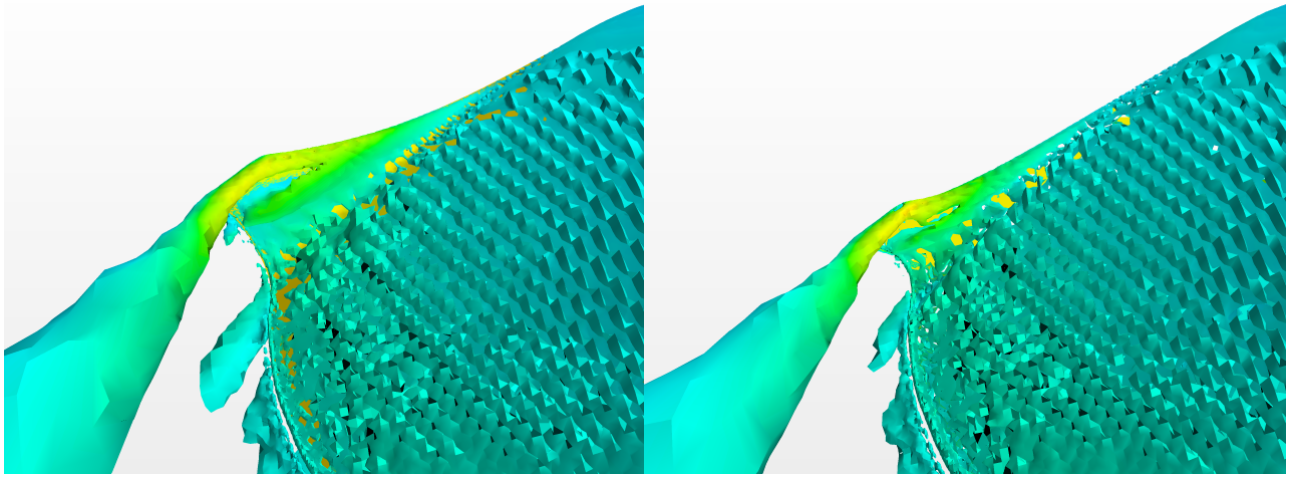

Figure 6.35: The Q-Criterion isosurfaces for a value of 10 s^{-2} for the tall and short winglets.

Tall Winglet Propeller at $K_T = 0.169$

The winglet propellers deliver significantly more thrust than the conventional and tip loaded propellers at the same J, which could potentially make it a bit unfair to compare the vorticity at $J = 0.95$ and expect them to be lower in the case of the winglet propellers. A simulation was therefore done with the tall winglet propeller at $J = 1.056$, which gives the exact same K_T as the conventional propeller has at $J = 0.95$. The propellers then deliver the same amount of thrust, which makes the tip vortices easier to compare. Only the component that is normal to the axial one has been analysed, as this component can give details about the pressure leakage from the high pressure side to the suction side of the propeller blades. The result should be compared with Figure 6.22.

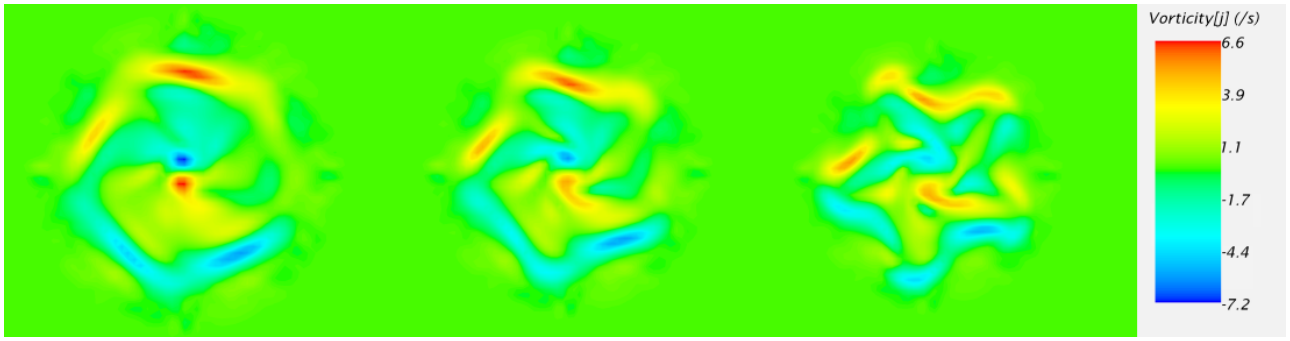

Figure 6.36: The wake vorticity normal to the axial component (positive direction for the vector is to the left) for the tall winglet propeller at $K_T = 0.169$. The planes are, from left to right, located at distances of $0.5D$, $1D$ and $2D$ behind the propeller. Red colour is clockwise, blue is anti clockwise – but be sure to remember the right hand rule, implying that the vorticity really is into the plane.

6.1.5 Wall $y+$

The wall $y+$ values are only presented for the conventional propeller for $J = 0.95$, as they are almost identical for all the propellers at all advance numbers.

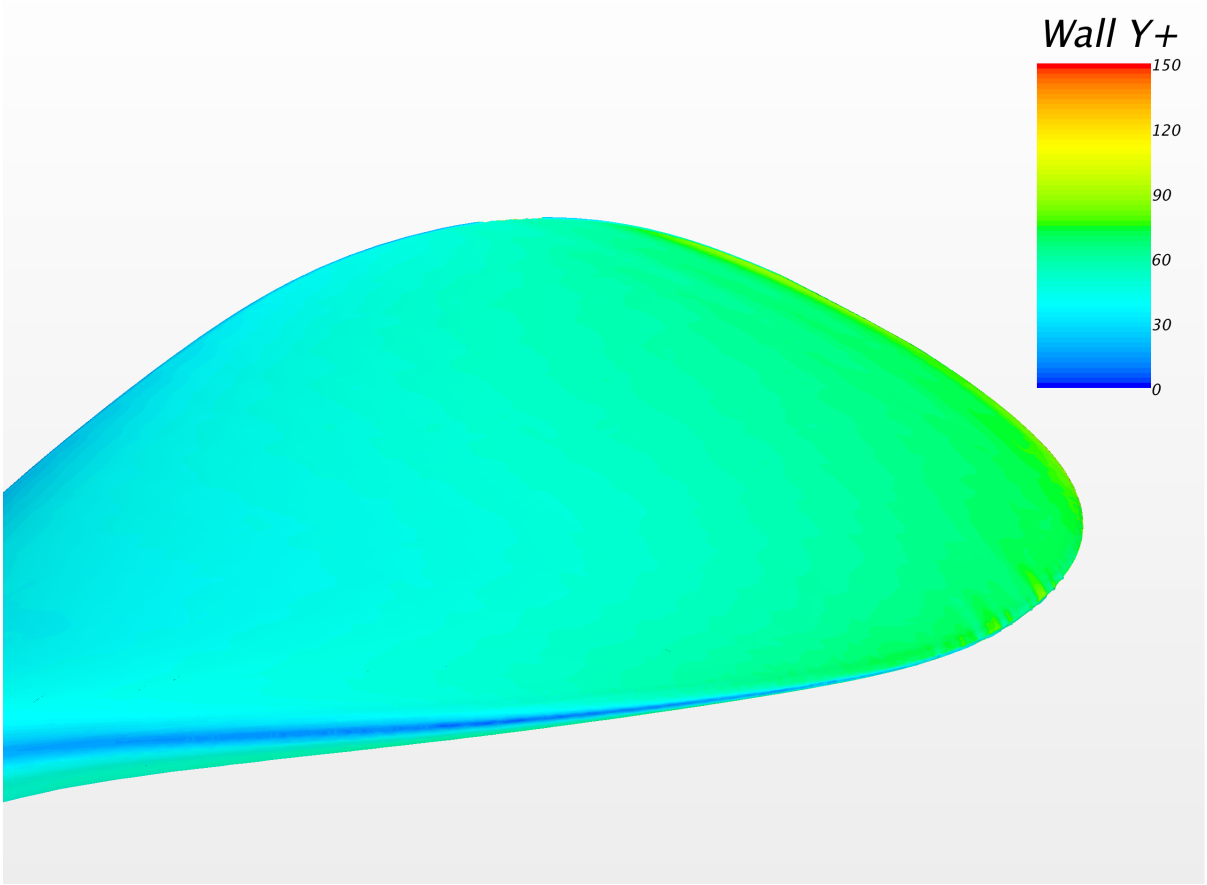

Figure 6.37: The wall $y+$ values for the conventional propeller at $J = 0.95$. The majority of the values are between 30 and 90, therefore making the 'High $y+$ wall treatment' model valid.

6.2 Unsteady Simulations

Only cavitation results are presented for the unsteady simulations. They are all for the short winglet propeller, and for advance numbers 0.2, 0.6 and 0.95. The Courant numbers for these simulations are very low, ensured by the low time step.

6.2.1 Advance Number $J = 0.20$

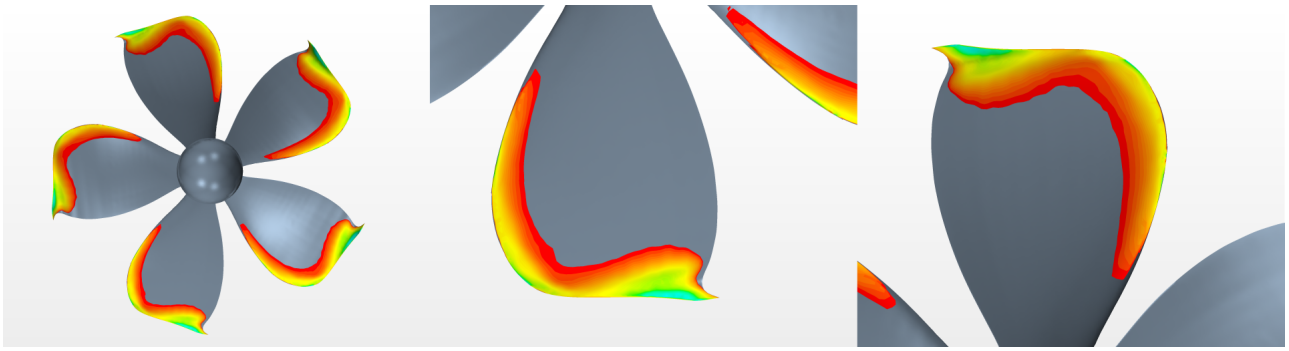

Figure 6.38: The cavitation sheet for the short winglet propeller at $J = 0.20$.

6.2.2 Advance Number $J = 0.60$

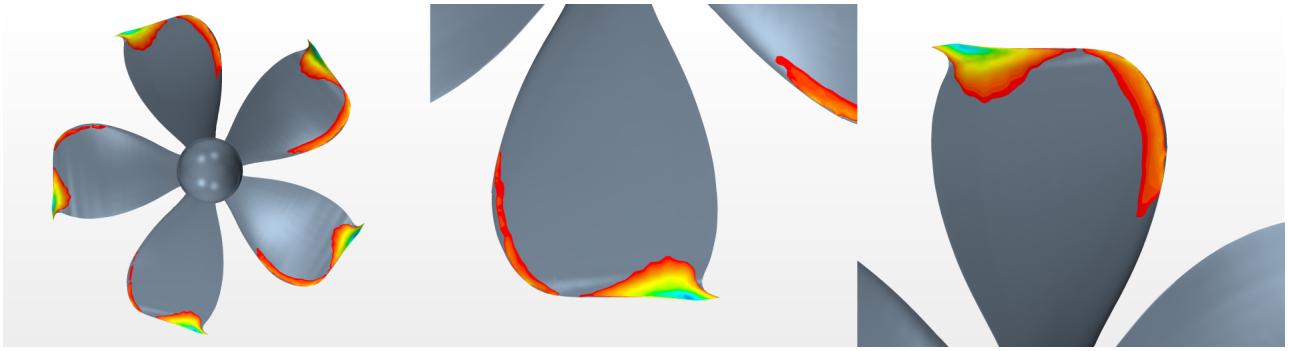

Figure 6.39: The cavitation sheet for the short winglet propeller at $J = 0.60$.

6.2.3 Advance Number $J = 0.95$

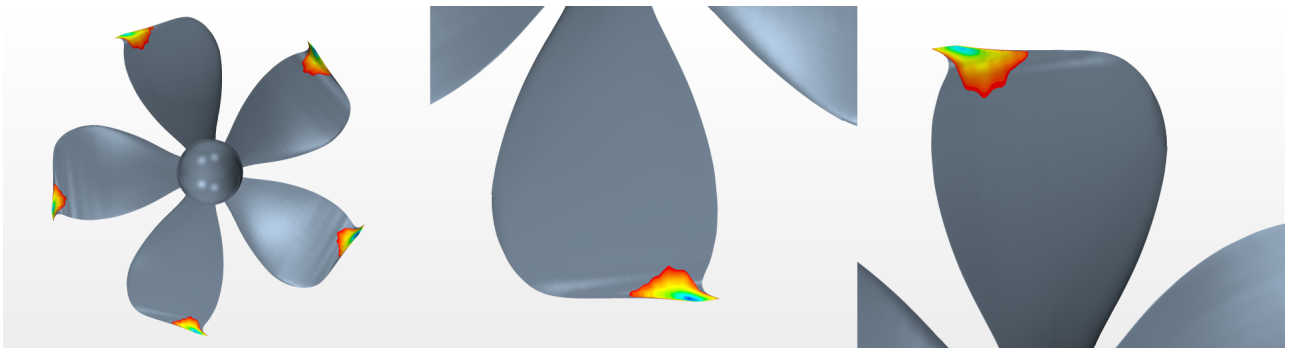

Figure 6.40: The cavitation sheet for the short winglet propeller at $J = 0.95$.

6.3 Comparison With the Wageningen B-Series

It is wise to conduct a comparison of the conventional propeller with the Wageningen B-Series propellers. The B-Series is the most comprehensive series ever tested, containing more than 120 different propellers (Steen 2014). They are assumed to be quite similar in both loading and geometry as the conventional propeller, and should therefore not deviate too much from the presented results.

The B-Series is often presented in so called Bp-δ diagrams, named after the two coefficients used to describe them:

$$Bp = \left(\frac{1}{2\pi\rho}\right)^{1/4} \frac{{\mathrm{P_D}}^{1/4}\, n^{1/2}}{V_A^{5/4}} \tag{6.1}$$

$$\delta = \frac{nD}{V_A} \tag{6.2}$$

$\mathrm{P_D}$ is the delivered power, and V_A is the advance velocity. δ is actually the reciprocal of J.

The 5-bladed diagram was used, with an EAR of 0.75. It is now possible to find either the diameter or the thrust by choosing which parameter to extract from the diagram. The delivered power becomes $\mathrm{P_D} = 1.8 \cdot 24 \cdot \frac{1.852}{3.6}$ MW $= 22.2$ MW by using the ship resistance of 1.8 MN, which makes the Bp coefficient equal approximately 0.43. δ is read from the diagram to be 1.05 ($\delta = 1.05$ is the same as $J \approx 0.95$) by following the optimum efficiency curve. The P/D ratio for the selected propeller is 1.2, and the diameter is found from δ to be 7.63 m. The efficiency is read from the graph to be approximately 71.5 %.

These results deviate from the design diameter of 7.9 m and pitch ratio of 1.37, as well as the EAR of 0.70 and efficiency of 75.5 %, but the results are essentially in quite good agreement.

6.4 Validity of Results

No experimental model tests have been done in order to check the obtained results. There are therefore not any assurances for them to be correct – but things are not that grim. The CFD simulations are based extensively upon a tutorial case from the STAR-CCM+ user guide with the best practice approach for open water tests presented. The propeller analysed in that case was the 'Potsdam Propeller Test Case – VP1304', and very good results were obtained by comparing them with experimental data (CD-adapco 2015). These results were also conservative, meaning that the solver slightly underestimated the thrust and overestimated the torque.

STAR-CCM+ has proved to be a very good and accurate tool in marine engineering, and the results obtained in this thesis are assumed reasonable because the best practices suggested by the software developer have been followed. The comparison with the Wageningen B-Series also supported the validity of the results.

Chapter 7

Discussion and Conclusion

The design advance number for the conventional propeller was $J = 0.92$, which was not matched perfectly by the lifting line program according to the CFD-results. The simulations showed an optimum point at $J = 1.02$, but this is not too far off the lifting line values, meaning that the lifting line program works as a good first approximation – at least for the pitch distribution. It is not a particularly accurate tool with regards to the thrust, torque and efficiency. A thrust of 2.15 MN, a torque of 2.95 MNm and an efficiency of 84.4 % was predicted, whereas the CFD-results showed a thrust of 1.47 MN, a torque of 2.50 MNm and an efficiency of 75.5 % at $J = 1.02$. This is quite far off the predicted values, but at a slightly lower J of 0.95 (which was chosen as the operating point) the values are 1.95 MN, 3.12 MNm and 74.5 % for the thrust, torque and efficiency respectively. The lifting line program is at least in the same ballpark for this advance number, which shows that it gives reasonable results in the vicinity of the design J. It is however imperative to do a more detailed analysis to make sure that the results are as desired.

The cavitation prediction by the lifting line program was satisfactory. The CFD results showed no problems with cavitation for the operating advance number of 0.95. It must be pointed out that the designs proposed in this thesis are for open water only, and therefore tuned to a zero wake situation. A propeller behind a ship works in a wake very far from zero, therefore making the cavitation performance much worse, which must be accounted for by for example reducing the lift coefficient at certain blade sections. The reason for the worsening of the cavitation performance in a wake can be seen in Figure 2.4, where an increase in w will reduce V and also the hydrodynamic angle of attack. The geometric angle of attack is however the same, implying that the propeller blade section must work at a significant angle of attack, which will induce very high velocities and low pressures at the leading edge – and possibly further towards the trailing edge as well. Much the same reason is the explanation for the severe cavitation experienced at low advance numbers, but V is then reduced directly, and not through an increasing w.

An arbitrary wake distribution can be handled fine by the lifting line program, but the wake is as mentioned set to zero.

The unsteady cavitation simulations showed that the cavitation is slightly overestimated by the steady state simulations.

The open water diagrams show a clear difference before and after the winglets were fitted. It is particularly interesting to see the difference in thrust of the tip loaded propeller and winglet fitted propellers, which all share the same base circulation distribution. The thrust for the tip loaded propeller is even lower than the one for the conventional propeller, which has an overall lower total circulation, but the thrust went up by 25 % and 40 % at $J = 0.95$ for the short and tall winglets respectively. Disappointingly, the torque went up even more for the same J,

by 34 % and 59 % respectively – leading to an overall reduction in the efficiency of 5.5 and 8.7 percentage points respectively. The cavitation sheets are more extensive for the winglet propellers, with the winglets more or less completely cavitating at all advance numbers.

There are some plausible explanations to these negative effects (the increased torque and severe cavitation). The winglet geometry is not optimally modelled, as explained in Chapter 4.4.1. Since the chord sections of the winglet are not curved to follow the correct radius, the likely outcomes are increased pressure drag and increased cavitation, with the latter probably connected to the winglet operating at an unfavourable angle of attack. This comes in addition to the already higher viscous drag due to the larger surface area being added by the winglet.

There are some interesting conclusions to draw from the open water diagrams, and especially the comparison of the thrust coefficients in Figure 6.5. The K_T values are shifted to the right, implying that the pitch is increased. An increased pitch will give a higher angle of attack, and hence a higher thrust at any given J. The zero-crossing point along the J-axis is therefore shifted to the right. The geometric angle of attack is the same for both winglet propellers as well as the tip loaded propeller, meaning that something is happening with the hydrodynamic angle of attack – or hydrodynamic pitch angle, as it may also be called. Induced velocities due to vortices must be involved with the change in pitch. The tip vortices will induce a downwash on the outer sections of the propeller blades, leading to a lower angle of attack – or equivalently a higher hydrodynamic pitch angle (look at Figure 2.4 to see what happens when the induced velocities are increased). The winglets will in theory reduce the tip vortices and therefore regain some of the lost lift by reducing the hydrodynamic pitch angle.

However, it is clear that the tip vortices are not reduced after all for the winglet propellers compared with the conventional and tip loaded propellers when looking at the vorticity figures in Chapter 6.1.4. This makes it a bit harder to explain the increased pitch. By looking at Figure 6.35, it is clear that the vortices originate first at the very tip of the winglets, putting a longer distance between the blades' trailing edges and the vortices. This should result in lower induced velocities at the blade sections, therefore reducing the hydrodynamic pitch, despite the larger tip vortices. However, the large vortices come with a cost, which is the increased torque. A vortex is water in a rapid swirling motion. This rotational energy is added to the water by the propeller, therefore making the propeller heavier to rotate. The reason why these vortices are larger than for the conventional propeller is difficult to say for sure, but it is believed to be connected to the unfavourable winglet geometry (as mentioned above and described in Chapter 4.4.1 as well). Also, the winglet should probably be stretched further towards the leading edge than what has been done. Fear of introducing too much viscous drag was the reason for making it shorter, but as the $a = 0.8$ camber line has constant chord-wise circulation all the way from the leading edge until about 80 % of the chord length, it is likely that even more of the vortices could be suppressed by extending the winglet further towards the leading edge. Another thing to point out is that a tall winglet is likely to induce a more powerful vortex in the axial component (the component shown in for example Figure 6.21), than compared with a shorter winglet or no winglet at all. The water will be sheared in this rotational component due to the viscous forces, which will be less critical for a shorter winglet or a conventional propeller. A lower and longer winglet could potentially be beneficial, but this is certainly an optimisation problem.

More of the pressure difference between the high pressure side and suction side of the blades are maintained towards the propeller tip, which also will contribute to the higher thrust and therefore also raise the K_T values. This effect will however not necessarily shift the zero-crossing point to the right, as the hydrodynamic pitch in this case may be close to the same. The first sections of a propeller to experience negative thrust when the advance number is increased is usually the tip. Assuming that the hydrodynamic and geometric pitch is the same, the

section will experience negative thrust at the same advance number regardless of the pressure distribution over the foil section. If however the induced velocities are reduced (something that is believed to be the case for the winglet propellers), the hydrodynamic pitch angle is reduced as well, which effectively is an increase of the propeller pitch. By looking at Figure 2.4 again, an even larger velocity V (i.e a higher J) is needed in order to achieve negative thrust.

This explanation is a simplification, as the pressure distribution is what produces lift, and the lift is proportional to the circulation which again is proportional to the induced velocities. A different pressure distribution will therefore also alter the induced velocities and hydrodynamic pitch, but not necessarily to the same extent as the tip vortices.

It is potentially a bit unfair to compare the propellers at the same advance number. The winglet propellers produce around 25 % and 40 % more thrust than the conventional propeller at $J = 0.95$, so it could therefore be unreasonable to expect the tip vortices to be lower for the winglet propellers at this operating point. A case with similarity in the K_T coefficients of the tall winglet propeller and the conventional propeller was therefore done in order to compare the vorticity of the two. $K_T = 0.169$ was chosen, as this gives the same thrust as the conventional propeller at $J = 0.95$. It is hard to tell much difference between Figures 6.36 and 6.22 seen apart from the the hub vortices. (The other vorticity components have higher values, but they are not presented in Chapter 6.) This would indicate that the winglet propellers indeed are worse than the conventional propeller in terms of tip vortices, and should further back up the theory of the increased thrust being developed by the displacement of the vortices rather than the reduction of them, together with the increased pressure difference towards the winglet.

Other remarks about the results in general are the vortex sheets at the inner blade sections for all the propeller variants. No good explanation for this effect is proposed, especially as the maximum efficiency of the conventional and tip loaded propellers is very high ($> 75\,\%$). It is therefore left unchecked whether this is a common result or rather a significant design flaw.

The results and the discussion may be wrapped up in this list of concluding remarks:

- The lifting line program written for the propeller design was vital for this thesis, and works well as a quick approximation for the propeller performance. More detailed analyses are however needed to be sure of the final results.
- The adding of winglets increased the delivered thrust and torque significantly. The overall efficiency was reduced when compared with the conventional design. The reason for the increased trust is believed to be the increased pressure difference at the outer blade sections, and also an increase of the propeller pitch by reducing the induced velocities at the propeller blades. The reduction of the induced velocities is believed to be connected to the displacement of the tip vortices to the very top of the winglets instead of at the propeller blades themselves. The tip vortices are not reduced as first anticipated, which is believed to be a vital component of the increased torque, together with an unfavourable winglet geometry and the increased viscous drag.
- The cavitation prediction by the lifting line program was good, as demonstrated by the CFD simulations of the conventional and tip loaded propellers. The winglet propellers experience more cavitation, with the winglets more or less covered by cavitation at all advance numbers, which is also believed to be connected with the unfavourable winglet geometry.
- There is great promise to reduce the torque by carefully designing the winglet. It is therefore concluded that there may be a potential of increased efficiency for the propeller designs proposed in this thesis, despite of the results achieved so far.

Chapter 8

Suggestions for Future Work

The main goal, or desired outcome of the thesis work, was to see the open water efficiency improved by adding winglets to the propeller. It is now evident that a much more careful design of the winglets must be done in order to achieve this. The list below proposes what should be done for any further studies regarding winglet equipped propellers on the basis of what has been done in this thesis:

- Make sure that the winglet properly follows the radial curvature at the outer propeller sections.
- Extend the winglet further towards the propeller blade's leading edge.
- Vary the height of the winglet.
- Do parameter studies on the subjects in point two and three above to analyse the sensitivity on thrust, torque, efficiency, cavitation and vorticity.

In addition, the following two points should be looked further into, preferably with parameter studies:

- Study the angle of the winglet relative to the propeller base line.
- Study the circulation on the winglet.

Bibliography

Abbott, Ira H., Albert E. von Doenhoff, and Louis S. Stivers Jr. (1945). "Report No. 824 - Summary of Airfoil Data". In: *National Advisory Committee for Aeronautics - NACA*.

Bertetta, Daniele et al. (2012). "EFD and CFD Characteristics of a CLT Propeller". In: *International Journal of Rotating Machinery*.

CD-adapco (2015). *STAR-CCM+ User Guide*.

Cheng, Hsun-jen et al. (2010). "A Numerical Comparison of End-Plate Effect Propellers and Conventional Propellers". In: *ScienceDirect - Journal of Hydrodynamics*.

DTU (2014). *KAPPEL Propeller*. URL: www.mek.dtu.dk/english/Sections/FVM/Research/KAPPEL_Propeller (visited on 05/20/2015).

Gennaro, Giulio and Juan Gonzalez-Adalid (2012). *Improving the Propulsion Efficiency by means of Contracted and Loaded Tip (CLT) Propellers*. SNAME 2012 – Athens, Greece.

Gonzalez-Adalid, Juan and Giulio Gennaro (2011). *Latest Experiences with Contracted and Loaded Tip (CLT) Propellers*. IMAM 2011 – Genoa, Italy.

Hoerner, Sighard F. (1952). "Aerodynamic Shape of the Wing Tips, Technical Report No. 5752". In: *USAF Technical Reports*.

HPC NTNU (2015). *OpenFOAM – Performance on Vilje*. URL: www.hpc.ntnu.no/display/hpc/OpenFOAM+-+Performance+on+Vilje (visited on 05/24/2015).

Ingeniøren (2014). *Kappel-propellere baner vej for succes hos MAN*. URL: ing.dk/artikel/kappel-propellere-baner-vej-succes-hos-man-167005 (visited on 05/20/2015).

Iranzo, A. et al. (2007). "Calculation of the Resistance and the Wave Profile of a 3600 TEU Container Ship". In: *Canal de Experiencias Hidrodinámicas del Pardo*.

Kerwin, Justin E. (2001). *13.04 Lecture Notes: Hydrofoils and Propellers*.

Krasilnikov, Vladimir, Zhirong Zhang, and Fangwen Hong (2009). *Analysis of Unsteady Propeller Blade Forces by RANS*. First International Symposium on Marine Propulsors 2009 – Trondheim, Norway.

McDonough, J. M. (2007). *Introductory Lectures on Turbulence – Physics, Mathematics and Modeling*. University of Kentucky.

Müller, Bernhard (2012). *Introduction to Computational Fluid Dynamics*.

Nielsen, Jens R. et al. (2012). *Combined Kappel Propeller and Rudder Bulb System for Improved Propulsion Efficiency*. The Motorship Conference 2012 – Hamburg, Germany.

PDAS (2001). *Download the NACA456 Program*. URL: www.pdas.com/naca456download.html (visited on 05/05/2015).

Scott, Jeff (2001). *NACA Airfoil Series*. URL: www.aerospaceweb.org/question/airfoils/q0041.shtml (visited on 05/06/2015).

Simman (2008). *MOERI Container Ship (KCS)*. URL: www.simman2008.dk/KCS/kcs_geometry.htm (visited on 05/07/2015).

Steen, Sverre (2014). *Foil and Propeller Theory*. NTNU.

Symscape (2013). *Polyhedral, Tetrahedral, and Hexahedral Mesh Comparison*. URL: www.symscape.com/polyhedral-tetrahedral-hexahedral-mesh-comparison (visited on 05/24/2015).

The Motorship (2012a). *Close-up view of the CLT propeller on tanker 'Roy Maersk'*. URL: www.motorship.com/news101/engines-and-propulsion/maersk-opts-for-energy-saving-propellers (visited on 05/19/2015).

— (2012b). *Five-bladed Kappel tip fin design FP propeller*. URL: www.motorship.com/news101/industry-news/man-acquires-kappel-propeller-designs (visited on 05/20/2015).

TOP500 (2014). *Top 500 The List – November 2014*. URL: www.top500.org/lists/2014/11 (visited on 05/24/2015).

van Oossanen, Piet (1974). "Calculation of Performance and Cavitation Characteristics of Propellers Including Effects of Non-Uniform Flow and Viscosity". PhD thesis. Netherlands Ship Model Basin, Wageningen.

Versteeg, H. K. and W. Malalasekera (2007). *An Introduction to Computational Fluid Dynamics: The Finite Volume Method, Second Edition*. Prentice Hall.

Whitcomb, Richard T. (1976). "A Design Approach and Selected Wind-Tunnel Results at High Subsonic Speeds for Wing-Tip Mounted Winglets". In: *National Aeronautics and Space Administration - NASA*.

White, Frank M (2006). *Viscous Fluid Flow, Third Edition*. McGraw-Hill.

Wikimedia Commons (2007). *Winglet on Turkish B737-800*. URL: commons.wikimedia.org/wiki/File:Winglet_B737-800.JPG (visited on 05/21/2015).

Appendices

Appendix A

MATLAB Program

A.1 Source Code

lifting_line_induction.m

```
% "lifting_line_induction.m" is a lifting line program intended for marine
% propeller design. It is based on the induction factor method, with NACA
% 16-series profiles and the a = 0.8 camber line. Requires the functions
% "inductions_factors.m" and "NACA_16_a08.m" in order to run properly.
%
% Part of the Master's Thesis "Unconventional Propeller Tip Design" by
% Andreas Ommundsen, June 2015.
% Norwegian University of Science and Technology (NTNU), Trondheim.

function results = lifting_line_induction(N,D,RPM,Z,V_knots,rho,kin_visc, ...
                    draught,N_sections,k,tolerance,yield_strength, ...
                    threeD_corr,circulation_plot,beta_plot,induced_plot, ...
                    pitch_distr_plot,Cl_plot,thickness_plot, ...
                    residual_plot,propeller_plot,print)
tic
clc
close all
    R = D/2;
    D_hub = 0.2*D;
    r_hub = D_hub/2;
    radius = linspace(r_hub,R,N);
    dr = radius(2) - radius(1);
    n = RPM/60;
    V = V_knots*(1.852/3.6);

    sections = linspace(r_hub,R,N_sections);
    section_pos = zeros(1,N_sections);
    for i = 1:N_sections
        for j = 1:N
            if  round(abs(sections(i) - radius(j)),4) <= round(dr/2,4)
                section_pos(i) = j;
            end
        end
    end

    initialise = zeros(1,N);
    thickness_distr = initialise;
    circulation_distr = initialise;
```

```
dgamma_dr = initialise;
Ua_mean = initialise;
Ua = initialise;
Ut_mean = initialise;
Ut = initialise;
V_total = initialise;
Lift_distr = initialise;
Drag_distr = initialise;
pitch_distr = initialise;
Cl_distr = initialise;
Cd_distr = initialise;
T_distr = initialise;
Q_distr = initialise;
beta_mean = initialise;
beta = initialise;
beta_const = initialise;
wake_distr = initialise;
blade_moment = initialise;
necessary_thickness = initialise;
sigma = initialise;
minus_Cp = initialise;
theta = initialise;
thickness_flag = false;
final_residual_matrix = zeros(2,N);
coord = zeros(4*Z,N);
chord_distr_rpos = [0.2 0.3 0.4 0.5 0.6 0.7 0.8 0.9 0.95 0.975 ...
                    0.99 1]*R;
chord_distr_val = [0.16 0.21 0.26 0.296 0.32 0.33 0.32 0.28 ...
                   0.23 0.186 0.14 0.08]*D; % Conventional
chord_distr = interp1(chord_distr_rpos,chord_distr_val,radius,'spline');

if print == true
    fid = fopen('results_induction.txt','w');
end

r_prime = linspace(0,1,N);
r_wag = [0.2 0.3 0.4 0.5 0.6 0.7 0.8 0.9 1];
A_wag = [0.0526 0.0464 0.0402 0.0340 0.0278 0.0216 0.0154 0.0092 0.0030];
B_wag = [0.0040 0.0035 0.0030 0.0025 0.0020 0.0015 0.0010 0.0005 0.0000];
if  Z == 3
    B_wag(8) = 0.0002;
end
t_wag = D*(A_wag - Z*B_wag);
t_wag_int = interp1(r_wag,t_wag,radius/R,'linear')*1000;

EAR = 0;

for i = 1:N
    circulation_distr(i) = k*(-35.064*r_prime(i)^6 + ...
        76.35*r_prime(i)^5 - 53.503*r_prime(i)^4 + ...
        7.7968*r_prime(i)^3 + 3.3104*r_prime(i)^2 + ...
        1.0523*r_prime(i) + 0.0575); % Conventional
%   circulation_distr(i) = k*(-22.85*r_prime(i)^6 + ...
%       46.304*r_prime(i)^5 - 25.427*r_prime(i)^4 - ...
%       4.3941*r_prime(i)^3 + 5.6943*r_prime(i)^2 + ...
%       0.8884*r_prime(i) + 0.0964); % Tip loaded

    if  round((radius(i)/R) - 0.7,4) <= round((dr/2)/R,4)
        index_07 = i;
    end
```

```
%   chord_distr(i) = (-17.659*(radius(i)/R)^6 + ...
%       55.641*(radius(i)/R)^5 - 69.58*(radius(i)/R)^4 + ...
%       43.321*(radius(i)/R)^3 - 14.401*(radius(i)/R)^2 + ...
%       2.9474*(radius(i)/R) - 0.1055)*D; % Tip loaded
    thickness_distr(i) = (t_wag_int(i)/chord_distr(i))*(1/1000);
    EAR = EAR + chord_distr(i)*dr;
    Ut_mean(i) = round(circulation_distr(i)/(2*pi*radius(i)),6);
    a = 1;
    b = 2*V*(1 - wake_distr(i));
    c = -Ut_mean(i)*(4*pi*radius(i)*n - Ut_mean(i));
    sol_1 = (-b + sqrt(b^2 - 4*a*c))/(2*a);
    sol_2 = (-b - sqrt(b^2 - 4*a*c))/(2*a);
    if round(sol_1,6) >= 0
       Ua_mean(i) = sol_1;
    else
       Ua_mean(i) = sol_2;
    end
    if  (Ut_mean(i) == 0) && (Ua_mean(i) == 0)
        beta_mean(i) = pi/4; % Limit of atan(x/x) when x -> 0
    else
        beta_mean(i) = atan(Ut_mean(i)/Ua_mean(i));
    end
end
EAR = (EAR*Z)/(pi*R^2);

for i = 1:N
    % Differentiating the circulation distribution.
    if i == 1
        % First order forward differencing for i = 1
        dgamma_dr(i) = (circulation_distr(i + 1) - ...
                        circulation_distr(i))/dr;
    elseif i < N
        % Second order central differencing scheme for 1 < i < N
        dgamma_dr(i) = (circulation_distr(i + 1) - ...
                        circulation_distr(i - 1))/(2*dr);
    else
        % First order backward differencing for i = N
        dgamma_dr(i) = (circulation_distr(i) - ...
                        circulation_distr(i - 1))/dr;
    end
end

integrand = initialise;
failed_convergence_counter = 0;
res_counter = 0;
for i = 1:N
    residual_Ua = 1;    % Put to 1 in order to enter the while loop
    residual_Ut = 1;    % Put to 1 in order to enter the while loop
    start_Ua = Ua_mean(i);      % Guessing Ua
    start_Ut = Ut_mean(i);      % Guessing Ut
    start_beta = beta_mean(i);  % Guessing beta_i (calculated from Ua
                                % and Ut above)
    counter = 0;
    exit_flag = 0;
    while ((residual_Ua > tolerance) || (residual_Ut > tolerance)) && ...
        (exit_flag == false)
        updated_Ua = 0;
        updated_Ut = 0;
        for j = 1:N
```

```
            ind_factors = induction_factors(radius(i)/radius(j), ...
                start_beta,Z);
            if j ~= i
               updated_Ua = updated_Ua + ((ind_factors.i_a/(2* ...
                   Z*pi))*(dgamma_dr(j))*(1/(radius(i) - radius(j))))*dr;
               updated_Ut = updated_Ut + ((ind_factors.i_t/(2* ...
                   Z*pi))*(dgamma_dr(j))*(1/(radius(i) - radius(j))))*dr;
               if i == N
                   integrand(j) = (ind_factors.i_a/(2*Z*pi))* ...
                        (dgamma_dr(j))*(1/(radius(i) - radius(j)));
               end
               if (isnan(updated_Ua) == true) || (isnan ...
                       (updated_Ut) == true)
                  exit_flag = 1;
               end
            end
        end
        start_beta = atan((V*(1 - wake_distr(i)) + updated_Ua/2)/ ...
                     (2*pi*radius(i)*n - updated_Ut/2));
        residual_Ua = abs(start_Ua - updated_Ua);
        residual_Ut = abs(start_Ut - updated_Ut);
        start_Ua = updated_Ua;
        start_Ut = updated_Ut;
        counter = counter + 1;
        res_counter = res_counter + 1;
        complete_residuals(1,res_counter) = residual_Ua; %#ok
        complete_residuals(2,res_counter) = residual_Ut; %#ok
        if counter == 100
           exit_flag = 1;
        end
    end

    final_residual_matrix(1,i) = residual_Ua;
    final_residual_matrix(2,i) = residual_Ut;

    if print == false
        if exit_flag == false
            disp(['Lifting line ',num2str(i),' of ',num2str(N), ...
                ' converged in ',num2str(counter),' iterations:'])
            disp(['    Final residual Ua = ',num2str(residual_Ua)])
            disp(['    Final residual Ut = ',num2str(residual_Ut)])
            disp(' ')
        else
            failed_convergence_counter = failed_convergence_counter + 1;
            failed_convergence_vector( ...
                failed_convergence_counter) = i; %#ok
            disp(['WARNING: Lifting line ',num2str(i),' of ', ...
                num2str(N),' failed to converge:'])
            disp(['    Final residual Ua = ',num2str(residual_Ua)])
            disp(['    Final residual Ut = ',num2str(residual_Ut)])
            disp(' ')
        end
    else
        if exit_flag == false
            disp(['Lifting line ',num2str(i),' of ',num2str(N), ...
                ' converged in ',num2str(counter),' iterations:'])
            disp(['    Final residual Ua = ',num2str(residual_Ua)])
            disp(['    Final residual Ut = ',num2str(residual_Ut)])
            disp(' ')
            fprintf(fid,'%s \n',['Lifting line ',num2str(i),' of ', ...
```

```
                num2str(N),' converged in ',num2str(counter), ...
                ' iterations:']);
            fprintf(fid,'%s \n',['    Final residual Ua = ', ...
                num2str(residual_Ua)]);
            fprintf(fid,'%s \n',['    Final residual Ut = ', ...
                num2str(residual_Ut)]);
            fprintf(fid,'\n');
        else
            failed_convergence_counter = failed_convergence_counter + 1;
            failed_convergence_vector( ...
                failed_convergence_counter) = i; %#ok
            disp(['WARNING: Lifting line ',num2str(i),' of ', ...
                num2str(N),' failed to converge:'])
            disp(['    Final residual Ua = ',num2str(residual_Ua)])
            disp(['    Final residual Ut = ',num2str(residual_Ut)])
            disp(' ')
            fprintf(fid,'%s \n',['WARNING: Lifting line ',num2str(i), ...
                ' of ',num2str(N),' failed to converge:']);
            fprintf(fid,'%s \n',['    Final residual Ua = ', ...
                num2str(residual_Ua)]);
            fprintf(fid,'%s \n',['    Final residual Ut = ', ...
                num2str(residual_Ut)]);
            fprintf(fid,'\n');
        end
    end

    Ua(i) = real(updated_Ua);
    Ut(i) = real(updated_Ut);
    beta(i) = atan((V + Ua(i)/2)/(2*pi*radius(i)*n - Ut(i)/2));
end

for i = 1:N
    V_total(i) = sqrt((V*(1 - wake_distr(i)) + Ua(i)/2)^2 + ...
                 (2*pi*radius(i)*n - Ut(i)/2)^2);
    Lift_distr(i) = rho*V_total(i)*(circulation_distr(i)/Z);
    Cl_distr(i) = Lift_distr(i)/((0.5*rho*V_total(i)^2)*chord_distr(i));
    Rn = V_total(i)*chord_distr(i)/kin_visc;
    Cf = 0.075/((log10(Rn) - 2)^2);
    Cd_distr(i) = 2*Cf*(1 + 2*thickness_distr(i)/chord_distr(i));
    Drag_distr(i) = 0.5*rho*(V_total(i)^2)*Cd_distr(i)*chord_distr(i);
    T_distr(i) = rho*(circulation_distr(i)/Z)*(2*pi*radius(i)*n - ...
                 Ut(i)/2) - Cd_distr(i)*sin(beta(i));
    Q_distr(i) = rho*(circulation_distr(i)/Z)*(V*(1 - wake_distr(i)) ...
                 + Ua(i)/2)*radius(i) + Cd_distr(i)* ...
                 cos(beta(i))*radius(i);
    pitch_distr(i) = 2*pi*R*atan(beta(i) + (1.54*pi/180)*Cl_distr(i))/D;
    beta_const(i) = tan(beta_mean(i))/tan(beta(i));
end

if failed_convergence_counter > 0
   for i = 1:failed_convergence_counter
       T_distr(failed_convergence_vector(i)) = 0;
       Q_distr(failed_convergence_vector(i)) = 0;
   end
end

I = 7.0994865e-05; % Second area of moment of symmetric NACA 16-012,
                   % with chord length 1 m. Units m^4.
for i = 1:N
    for j = i:N
```

```
        blade_moment(i) = blade_moment(i) + T_distr(j)*dr;
    end
    if  blade_moment(i) < 0
        blade_moment(i) = 0;
    end
    necessary_thickness(i) = sqrt((27*blade_moment(i))/ ...
            (I*(chord_distr(i)^4)*31250*yield_strength))*1000; % mm
    if  thickness_distr(i)*chord_distr(i)*1000 < necessary_thickness(i)
        thickness_flag = true;
    end
end

T_tot = 0;
Q_tot = 0;
for i = 1:N
   T_tot = T_tot + T_distr(i)*Z*dr;
   Q_tot = Q_tot + Q_distr(i)*Z*dr;
end
Eta = (T_tot*V)/(2*pi*n*Q_tot);

for i = 1:N_sections
    results.section(i).r_R = radius(section_pos(i))/R;
    results.section(i).Cl = Cl_distr(section_pos(i));
    results.section(i).t_c = thickness_distr(section_pos(i));
    results.section(i).chord_length = chord_distr(section_pos(i));
end
results.total_thrust = T_tot;
results.total_torque = Q_tot;
results.efficiency = Eta;
results.EAR = EAR;
results.P_D = 2*pi*R*atan(beta(index_07) + (1.54*pi/180)* ...
              Cl_distr(index_07))/D;
results.J = V/(n*D);

if  circulation_plot == true
    figure(1)
    plot(radius/R,circulation_distr)
    title('Circulation distribution')
    xlabel('r/R')
    ylabel('\Gamma(r/R)')
    box on
    grid on
    axis([0.2 1 0 ceil(max(circulation_distr))])
    movegui('west');

    figure(2)
    plot(radius/R,dgamma_dr)
    title('Derivative of the circulation distribution')
    xlabel('r/R')
    ylabel('d/dr \Gamma(r/R)')
    box on
    grid on
    movegui('east');
end

if  beta_plot == true
    figure(3)
    handlevector(1) = plot(radius/R,beta_mean*180/pi);
    hold on
    handlevector(2) = plot(radius/R,beta*180/pi);
```

```
    legend(handlevector,'Complete momentum theory', ...
        'Induction factor method','Location','Best')
    title('\beta_i')
    xlabel('r/R')
    ylabel('Hydrodynamic angle of attack - (degrees)')
    box on
    grid on
    movegui('north');
end

if  induced_plot == true
    figure(4)
    handlevector(1) = plot(radius/R,Ua_mean/2);
    hold on
    handlevector(2) = plot(radius/R,Ua/2);
    legend(handlevector,'Complete momentum theory', ...
        'Induction factor method','Location','Best')
    title('U_a')
    xlabel('r/R')
    ylabel('Induced axial velocity - (m/s)')
    box on
    grid on
    movegui('northwest');

    figure(5)
    handlevector(1) = plot(radius/R,Ut_mean/2);
    hold on
    handlevector(2) = plot(radius/R,Ut/2);
    legend(handlevector,'Complete momentum theory', ...
        'Induction factor method','Location','Best')
    title('U_t')
    xlabel('r/R')
    ylabel('Induced tangential velocity - (m/s)')
    box on
    grid on
    movegui('northeast');
end

if  pitch_distr_plot == true
    figure(6)
    plot(radius/R,pitch_distr);
    title('Pitch distribution')
    xlabel('r/R')
    ylabel('P/D')
    box on
    grid on
    movegui('south');
    figure(7)
    plot(radius/R,beta_const);
    title('Pitch distribution')
end

if  Cl_plot == true
    figure(7)
    plot(radius/R,Cl_distr);
    title('Lift coefficient distribution')
    xlabel('r/R')
    ylabel('C_L')
    box on
    grid on
```

```
    movegui('south');
end

if  thickness_plot == true
    figure(8)
    handlevector3(1) = plot(radius/R,necessary_thickness);
    hold on
    handlevector3(2) = plot(radius/R,t_wag_int);
    handlevector3(3) = plot(radius/R,thickness_distr.* ...
                       chord_distr.*1000);

    legend(handlevector3,'Necessary thickness','Wageningen thickness', ...
        'Current thickness','Location','Best')
    title('Thickness distribution')
    xlabel('r/R')
    ylabel('Thickness - (mm)')
    box on
    grid on
end

if  draught > 0;
    p_a = 101325;
    p_v = 1500;
    g = 9.81;
    % :)
    for i = 1:N
        sigma(i) = (p_a - p_v + rho*g*(draught - radius(i)))/ ...
            (0.5*rho*V_total(i)^2);
        v_V = (1.137 - 1)*thickness_distr(i)/0.12;
        dv_V = Cl_distr(i)*0.278;
        minus_Cp(i) = (1 + v_V + dv_V)^2 - 1;
    end

    figure(9)
    handlevector(1) = plot(radius/R,sigma,'LineWidth',2);
    hold on
    handlevector(2) = plot(radius/R,minus_Cp);
    legend(handlevector,'\sigma','-C_p','Location','Best')
    title('Cavitation check: OK for -C_p < \sigma')
    xlabel('r/R')
    ylabel('-')
    box on
    grid on
end

if  residual_plot == true
    figure(10)
    handlevector(1) = semilogy(1:res_counter,complete_residuals(1,:));
    hold on
    handlevector(2) = semilogy(1:res_counter,complete_residuals(2,:));
    axis([0 res_counter 0 ceil(max(max(complete_residuals)))])
    legend(handlevector,'U_a','U_t','Location','Best')
    title('Total residuals')
    xlabel('Accummulated iteration')
    ylabel('Residuals')
    box on
    grid on
    movegui('southwest');

    figure(11)
```

```
    handlevector(1) = semilogy(1:N,final_residual_matrix(1,:));
    hold on
    handlevector(2) = semilogy(1:N,final_residual_matrix(2,:));
    axis([0 N 0 ceil(max(max(final_residual_matrix)))])
    legend(handlevector,'U_a','U_t','Location','Best')
    title('Final residuals')
    xlabel('Lifting line number')
    ylabel('Residuals')
    box on
    grid on
    movegui('southeast');
end

if  propeller_plot == true
    x_hub = linspace(-r_hub,r_hub,500);
    x_disk = linspace(-R,R,500);
    y_hub_pos = zeros(1,500);
    y_hub_neg = zeros(1,500);
    y_disk_pos = zeros(1,500);
    y_disk_neg = zeros(1,500);
    for i = 1:500
        y_hub_pos(i) = sqrt(r_hub^2 - x_hub(i)^2);
        y_hub_neg(i) = -y_hub_pos(i);
        y_disk_pos(i) = sqrt(R^2 - x_disk(i)^2);
        y_disk_neg(i) = -y_disk_pos(i);
    end

    figure(12)
    hold on
    title('Expanded Propeller View')
    xlabel('Distance - (m)')
    ylabel('Distance - (m)')
    box on
    grid on
    for i = 1:Z
        alpha = (2*pi/Z)*i;
        for j = 1:N
            theta(j) = atan((chord_distr(j)/2)/radius(j));
            coord(i,j) = radius(j)*cos(alpha + theta(j));
            coord(2*i,j) = radius(j)*sin(alpha + theta(j));
            coord(3*i,j) = radius(j)*cos(alpha - theta(j));
            coord(4*i,j) = radius(j)*sin(alpha - theta(j));
        end
        plot(coord(i,:),coord(2*i,:),'Color','b')
        plot(coord(3*i,:),coord(4*i,:),'Color','b')
    end
    plot(x_hub,y_hub_pos,x_hub,y_hub_neg,'Color','b')
    plot(x_disk,y_disk_pos,x_disk,y_disk_neg,'Color','r')
    axis([-R R -R R])
end

if print == false
    if failed_convergence_counter > 0
       disp(['WARNING: ',num2str(failed_convergence_counter),' of ', ...
           num2str(N),' lifting lines failed to converge.'])
       disp(['-------------------------------------------------' ...
             '-----------------------------------'])
       disp(['FINAL RESULTS (ignoring lifting lines that' ...
             ' failed to converge):'])
       disp(['-------------------------------------------------' ...
```

```
            '-------------------------------------'])
    else
       disp(['-------------------------------------------------' ...
            '-------------------------------------'])
       disp('FINAL RESULTS:')
       disp(['-------------------------------------------------' ...
            '-------------------------------------'])
    end
    disp(['Total thrust: ',num2str(round(T_tot,2)),' N'])
    disp(['Total torque: ',num2str(round(Q_tot,2)),' Nm'])
    disp(['Efficiency: ',num2str(round(100*Eta,2)),' %'])
    disp(['Expanded Area Ratio: ',num2str(round(EAR,2))])
    disp(['P/D at 0.7R: ',num2str(round(2*pi*R*atan(beta(index_07) + ...
        (1.54*pi/180)*Cl_distr(index_07))/D,2))])
    disp(['Advance number J = ',num2str(round(V/(n*D),2))])
    disp(['-------------------------------------------------' ...
            '-------------------------------------'])
    if  thickness_flag == true
        disp(['WARNING: Danger of blade failure. Revise the' ...
            ' thickness distribution.'])
    end
    if  max(Cl_distr) > 1
        disp(['Maximum span-wise lift coefficient is ', ...
            num2str(max(Cl_distr)), ...
            ' > 1. Consider revising the propeller design.'])
    end
    if  chord_distr(1)*sin(beta(1) + (1.54*pi/180)*Cl_distr(1)) > D_hub
        disp(['Required hub height is ',num2str(ceil(chord_distr(1)* ...
            sin(beta(1) + (1.54*pi/180)*Cl_distr(1))*1000)), ...
            ' mm. Consider revising the chord distribution.'])
        disp(['    Maximum root chord length when hub height is' ...
            ' constrained to 0.2D: ',num2str(floor((D_hub/ ...
            sin(beta(1) + (1.54*pi/180)*Cl_distr(1)))*1000)),' mm.'])
    end
    if  chord_distr(1)*cos(beta(1) + (1.54*pi/180)*Cl_distr(1)) > D_hub
        disp(['Required hub diameter is ',num2str(ceil(chord_distr(1)* ...
            cos(beta(1))*1000)),' mm. Consider revising ' ...
            'the chord distribution.'])
        disp(['    Maximum root chord length when hub diameter is' ...
            ' constrained to 0.2D: ',num2str(floor((D_hub/ ...
            cos(beta(1) + (1.54*pi/180)*Cl_distr(1)))*1000)),' mm.'])
    end
    disp(['-------------------------------------------------' ...
            '-------------------------------------'])
else
    if failed_convergence_counter > 0
       disp(['WARNING: ',num2str(failed_convergence_counter),' of ', ...
           num2str(N),' lifting lines failed to converge.'])
       disp(['-------------------------------------------------' ...
            '-------------------------------------'])
       disp(['FINAL RESULTS (ignoring lifting lines that' ...
            ' failed to converge):'])
       disp(['-------------------------------------------------' ...
            '-------------------------------------'])
       fprintf(fid,'%s \n',['WARNING: ', ...
           num2str(failed_convergence_counter),' of ',num2str(N), ...
           ' lifting lines failed to converge.']);
       fprintf(fid,'%s \n',['-----------------------------------------' ...
            '-----------------------------------------']);
       fprintf(fid,'%s \n',['FINAL RESULTS (ignoring lifting lines' ...
```

```
                        ' that failed to converge):']);
    fprintf(fid,'%s \n',['----------------------------------------' ...
          '----------------------------------------------']);
else
    disp(['-------------------------------------------------' ...
          '-----------------------------------']);
    disp('FINAL RESULTS:')
    disp(['-------------------------------------------------' ...
          '-----------------------------------']);
    fprintf(fid,'%s \n',['----------------------------------------' ...
          '----------------------------------------------']);
    fprintf(fid,'%s \n','FINAL RESULTS:');
    fprintf(fid,'%s \n',['----------------------------------------' ...
          '----------------------------------------------']);
end
disp(['Total thrust: ',num2str(round(T_tot,2)),' N'])
disp(['Total torque: ',num2str(round(Q_tot,2)),' Nm'])
disp(['Efficiency: ',num2str(round(100*Eta,2)),' %'])
disp(['Expanded Area Ratio: ',num2str(round(EAR,2))])
disp(['P/D at 0.7R: ',num2str(round(2*pi*R*atan(beta(index_07) + ...
    (1.54*pi/180)*Cl_distr(index_07))/D,2))])
disp(['Advance number J = ',num2str(round(V/(n*D),2))])
disp(['-------------------------------------------------' ...
          '-----------------------------------'])
if  thickness_flag == true
    disp(['WARNING: Danger of blade failure. ' ...
          'Revise the thickness distribution.'])
end
if  max(Cl_distr) > 1
    disp(['Maximum span-wise lift coefficient is ',num2str ...
        (max(Cl_distr)),' > 1. Consider revising the'
        ' propeller design.'])
end
if  chord_distr(1)*sin(beta(1) + (1.54*pi/180)*Cl_distr(1)) > D_hub
    disp(['Required hub height is ',num2str(ceil(chord_distr(1)* ...
        sin(beta(1) + (1.54*pi/180)*Cl_distr(1))*1000)),' mm.' ...
        ' Consider revising the chord distribution.'])
    disp(['    Maximum root chord length when hub height is '
          'constrained to 0.2D: ',num2str(floor((D_hub/sin ...
          (beta(1) + (1.54*pi/180)*Cl_distr(1)))*1000)),' mm.'])
end
if  chord_distr(1)*cos(beta(1) + (1.54*pi/180)*Cl_distr(1)) > D_hub
    disp(['Required hub diameter is ',num2str(ceil(chord_distr(1)* ...
        cos(beta(1))*1000)),' mm. Consider revising the' ...
        ' chord distribution.'])
    disp(['    Maximum root chord length when hub diameter ' ...
          'is constrained to 0.2D: ',num2str(floor((D_hub/ ...
          cos(beta(1) + (1.54*pi/180)*Cl_distr(1)))*1000)),' mm.'])
end
disp(['-------------------------------------------------' ...
          '-----------------------------------'])
fprintf(fid,'%s \n',['Total thrust: ',num2str(round(T_tot,2)),' N']);
fprintf(fid,'%s \n',['Total torque: ',num2str(round(Q_tot,2)),' Nm']);
fprintf(fid,'%s \n',['Efficiency: ',num2str(round(100*Eta,2)),' %']);
fprintf(fid,'%s \n',['Expanded Area Ratio: ',num2str(round(EAR,2))]);
fprintf(fid,'%s \n',['P/D at 0.7R: ',num2str(round(2*pi*R* ...
    atan(beta(index_07) + (1.54*pi/180)*Cl_distr(index_07))/D,2))]);
fprintf(fid,'%s \n',['Advance number J = ',num2str(round(V/(n*D),2))]);
fprintf(fid,'%s \n',['----------------------------------------' ...
          '----------------------------------------------']);
```

```
        if  thickness_flag == true
            fprintf(fid,'%s \n',['WARNING: Danger of blade failure.' ...
                                 ' Revise the thickness distribution.']);
        end
        if  max(Cl_distr) > 1
            fprintf(fid,'%s \n',['Maximum span-wise lift coefficient is ', ...
                num2str(max(Cl_distr)),' > 1. Consider revising ' ...
                                          'the propeller design.']);
        end
        if  chord_distr(1)*sin(beta(1) + (1.54*pi/180)*Cl_distr(1)) > D_hub
            fprintf(fid,'%s \n',['Required hub height is ',num2str ...
                (ceil(chord_distr(1)*sin(beta(1) + (1.54*pi/180)*...
                Cl_distr(1))*1000)),' mm. Consider revising the ' ...
                                    'chord distribution.']);
            fprintf(fid,'%s \n',['    Maximum root chord length when hub' ...
                ' height is constrained to 0.2D: ',num2str(floor((D_hub/ ...
                sin(beta(1) + (1.54*pi/180)*Cl_distr(1)))*1000)),' mm.']);
        end
        if  chord_distr(1)*cos(beta(1) + (1.54*pi/180)*Cl_distr(1)) > D_hub
            fprintf(fid,'%s \n',['Required hub diameter is ',num2str(ceil ...
                (chord_distr(1)*cos(beta(1))*1000)),' mm. Consider' ...
               ' revising the chord distribution.']);
            fprintf(fid,'%s \n',['    Maximum root chord length when' ...
                ' hub diameter is constrained to 0.2D: ',num2str(floor ...
                ((D_hub/cos(beta(1) + (1.54*pi/180)* ...
                Cl_distr(1)))*1000)),' mm.']);
        end

        fprintf(fid,'%s',['----------------------------------------' ...
                 '------------------------------------------------']);
        fclose(fid);
    end

    if  threeD_corr == true
        for i = 1:N_sections
            k_c = 1.6946 + 0.5048*(radius(section_pos(i))/R) - 4.0012* ...
                (radius(section_pos(i))/R)^2 + 4.3283* ...
                (radius(section_pos(i))/R)^3;
            k_a = 1 + 1.46*(radius(section_pos(i))/R)^3;
            k_t = 2.5*(thickness_distr(section_pos(i))/radius ...
                (section_pos(i)))*(chord_distr(section_pos(i))/D)* ...
                cos(beta(section_pos(i)));
            NACA_16_a08(Cl_distr(section_pos(i)),thickness_distr ...
                (section_pos(i)),chord_distr(section_pos(i)),R,beta ...
                (section_pos(i))*180/pi,1,i,radius(section_pos(i)), ...
                k_c,k_a,k_t,0)
        end
    else
        for i = 1:N_sections
            k_c = 0;
            k_a = 0;
            k_t = 0;
            NACA_16_a08(Cl_distr(section_pos(i)),thickness_distr( ...
                section_pos(i)),chord_distr(section_pos(i)),R, ...
                beta(section_pos(i))*180/pi,1,i,radius(section_pos(i)), ...
                k_c,k_a,k_t,0)
        end
    end
toc
end
```

induction_factors.m

```
% "induction_factors.m" is part of the lifting line program
% "lifting_line_induction.m", intended for marine propeller design. This
% function calculates the induction factors according to the formulas of
% Piet van Oossanen which are used for calculation of the induced velocities.
%
% Part of the Master's Thesis "Unconventional Propeller Tip Design" by
% Andreas Ommundsen, June 2015.
% Norwegian University of Science and Technology (NTNU), Trondheim.

function induction = induction_factors(R,beta,Z)
    % R = r0/r, where r is the running variable and r0 is the fixed position
    % beta in radians
    % Z is number of blades

    p = 1 + (R/tan(beta))^2;
    a = (sqrt(p) - 1)*(((1/sin(beta)) - 1)^(-1))*(1/R);
    u = exp(Z*(log(a) + sqrt(p) - (1/sin(beta))));
    g = ((sin(beta)^3)*(2 + (9/(tan(beta)^2)))) + (3*p - 5)*p^(-1.5);
    f = (sin(beta)^(-0.5))*p^(-0.25);

    if  R > 1
        A = f*((1/(u - 1)) - (1/(24*Z))*g*log(u/(u - 1)));
        induction.i_a = (R - 1)*((Z*A)/(tan(beta)));
        induction.i_t = (1 - (1/R))*Z*(1 + A);
    elseif R == 1
        induction.i_a = cos(beta);
        induction.i_t = sin(beta);
    else
        B = f*((u/(1 - u)) + (1/(24*Z))*g*log(1/(1 - u)));
        induction.i_a = (1 - R)*(Z/tan(beta))*(1 + B);
        induction.i_t = ((1/R) - 1)*Z*B;
    end
end
```

NACA_16_a08.m

```
% "NACA_16_a08.m" is part of the lifting line program
% "lifting_line_induction.m", intended for marine propeller design. This
% function scales NACA 16-series profiles according to thickness, chord
% length and lift coefficient. The a = 0.8 camber line is used for the lift
% scaling. All coordinates are written to text-files.
%
% Part of the Master's Thesis "Unconventional Propeller Tip Design" by
% Andreas Ommundsen, June 2015.
% Norwegian University of Science and Technology (NTNU), Trondheim.


function NACA_16_a08(Cl,t,c,R,beta,centre,pos_index,pos,k_c,k_a,k_t, ...
                     figure_plot)
    x = [0 0.00005 0.0001 0.0002 0.0003 0.0004 0.0005 0.0006 0.0008 0.001 ...
         0.0012 0.0014 0.0016 0.0018 0.002 0.0025 0.003 0.0035 0.004 ...
         0.0045 0.005 0.006 0.007 0.008 0.009 0.01 0.011 0.012 0.013 ...
         0.014 0.015 0.016 0.018 0.02 0.025 0.03 0.035 0.04 0.045 0.05 ...
         0.055 0.06 0.07 0.08 0.09 0.1 0.12 0.14 0.16 0.18 0.2 0.22 0.24 ...
         0.26 0.28 0.3 0.32 0.34 0.36 0.38 0.4 0.42 0.44 0.46 0.48 0.5 ...
         0.52 0.54 0.56 0.58 0.6 0.62 0.64 0.66 0.68 0.7 0.72 0.74 0.76 ...
         0.78 0.8 0.82 0.84 0.86 0.88 0.9 0.92 0.94 0.95 0.96 0.97 0.975 ...
         0.98 0.985 0.99 0.995 0.999 1];
    N = 98;
    initialise = zeros(1,N);
    theta = initialise;
    x_upper = initialise;
    x_lower = initialise;
    y_upper = initialise;
    y_lower = initialise;
    y_t = [0 0.001257 0.001776 0.002508 0.003068 0.00354 0.003955 ...
        0.004329 0.004993 0.005576 0.006102 0.006585 0.007033 0.007454 ...
        0.007851 0.008762 0.009582 0.010334 0.011032 0.011686 0.012302 ...
        0.013443 0.014487 0.015454 0.016358 0.017209 0.018014 0.01878 ...
        0.019512 0.020212 0.020886 0.021534 0.022765 0.023919 0.026534 ...
        0.02885 0.030934 0.032833 0.034577 0.03619 0.03769 0.039089 ...
        0.041629 0.043875 0.045874 0.04766 0.050693 0.053129 0.055074 ...
        0.056607 0.05779 0.058674 0.059301 0.059709 0.059932 0.06 ...
        0.059937 0.05975 0.059442 0.059015 0.058472 0.057816 0.057048 ...
        0.056173 0.055192 0.054108 0.052923 0.051641 0.050263 0.048793 ...
        0.047234 0.045587 0.043855 0.042041 0.040148 0.038178 0.036134 ...
        0.034019 0.031834 0.029583 0.027269 0.024893 0.02246 0.01997 ...
        0.017427 0.014834 0.012192 0.009506 0.008146 0.006776 0.005396 ...
        0.004703 0.004007 0.003309 0.002608 0.001905 0.25*0.001341 0];
    x_c = [0 0.5 0.75 1.25 2.5 5 7.5 10 15 20 25 30 35 40 45 50 55 ...
           60 65 70 75 80 85 90 95 100]/100;
    y_c = [0 0.287 0.404 0.616 1.077 1.841 2.483 3.043 3.985 4.748 5.367 ...
           5.863 6.248 6.528 6.709 6.790 6.770 6.644 6.405 6.037 5.514 ...
           4.771 3.683 2.435 1.163 0]/100;
    dyc_dx = [((y_c(2)-y_c(1))/(x_c(2)-x_c(1))) 0.48535 0.44925 0.40359 ...
                0.34104 0.27718 0.23868 0.21050 0.16892 0.13734 0.11101 ...
                0.08775 0.06634 0.04601 0.02613 0.00620 -0.01433 ...
                -0.03611 -0.06010 -0.08790 -0.12311 -0.18412 -0.23921 ...
                -0.25583 -0.24904 -0.20385];

    y_t = y_t*(t/0.12);

    Cl = round(Cl,4);
```

```
if  (abs(k_c) > 0) && (abs(k_a) > 0) && (abs(k_t) > 0)
    y_c_int = interp1(x_c,y_c,x,'spline')*Cl*k_c;
    dyc_dx_int = interp1(x_c,dyc_dx,x,'spline')*Cl*k_c;
    alpha_i = 1.54*Cl*k_a + t*k_t;
else
    y_c_int = interp1(x_c,y_c,x,'spline')*Cl;
    dyc_dx_int = interp1(x_c,dyc_dx,x,'spline')*Cl;
    alpha_i = 1.54*Cl;
end

for i = 1:N
    theta(i) = atan(dyc_dx_int(i));
    x_upper(i) = x(i) - y_t(i)*sin(theta(i));
    x_lower(i) = x(i) + y_t(i)*sin(theta(i));
    y_upper(i) = y_c_int(i) + y_t(i)*cos(theta(i));
    y_lower(i) = y_c_int(i) - y_t(i)*cos(theta(i));
end

x_upper = x_upper*c;
x_lower = x_lower*c;
y_upper = y_upper*c;
y_lower = y_lower*c;

if  centre == true
    x_upper = x_upper - c/2;
    x_lower = x_lower - c/2;
    x = x - c/2;
end

if exist('NACA16_sections','dir') ~= 7
   mkdir('NACA16_sections');
end

if  t < 0.1
    fid = fopen(['NACA16_sections/sec',num2str(pos_index), ...
                 '_NACA_16-00',num2str(round(100*t)),'_a08.txt'],'w');
    fprintf(fid,'%s\n',['NACA 16-00',round(num2str(100*t)), ...
                ' a=0.8 with chord length = ',num2str(c),' m']);
else
    fid = fopen(['NACA16_sections/sec',num2str(pos_index), ...
                 '_NACA_16-0',num2str(round(100*t)),'_a08.txt'],'w');
    fprintf(fid,'%s\n',['NACA 16-0',num2str(round(100*t)), ...
                ' a=0.8 with chord length = ',num2str(c), ' m']);
end
fprintf(fid,'%s\n',['-----------------------------------------' ...
                    '---------------------------------']);
fprintf(fid,'%s\n',['BLADE SECTION ',num2str(pos_index)]);
fprintf(fid,'%s\n',['Non-dimensional radial position: ', ...
    num2str(pos/R),' - Absolute radial position: ',num2str(pos),' m']);
fprintf(fid,'%s\n',['Design lift coefficient: Cl = ',num2str(Cl)]);
fprintf(fid,'%s\n',['Design ideal angle of attack: alpha_i = ', ...
    num2str(alpha_i),' degrees']);
fprintf(fid,'%s\n',['Hydrodynamic angle of attack: beta_i = ', ...
    num2str(beta),' degrees']);
fprintf(fid,'%s\n',['Total angle of attack: alpha_i + beta_i = ', ...
    num2str(alpha_i + beta),' degrees']);
fprintf(fid,'%s\n',['-----------------------------------------' ...
                    '---------------------------------']);
fprintf(fid,'%s   %s\n','x/c','t/c');
```

```
    for i = N:-1:1
        string = sprintf('%f   %f',x_upper(i),y_upper(i));
        fprintf(fid,'%s\n',string);
    end

    for i = 2:N
        string = sprintf('%f   %f',x_lower(i),y_lower(i));

        if i ~= N
           fprintf(fid,'%s\n',string);
        else
           fprintf(fid,'%s',string);
        end
    end
    fclose(fid);

    if  figure_plot == true
        hold on
        plot(x_upper,y_upper,'Color',[0.2081,0.1663,0.5292])
        plot(x_lower,y_lower,'Color',[0.2081,0.1663,0.5292])
        plot(x_upper,y_upper,'r.')
        plot(x_lower,y_lower,'r.')
        plot(x*c,y_c_int*c,'r')
        if  t < 0.1
            title(['NACA 16-00',round(num2str(100*t)),' a=0.8'])
        else
            title(['NACA 16-0',round(num2str(100*t)),', a=0.8'])
        end
        axis([min(x_upper) max(x_upper) -1 1])
        xlabel('x/c')
        ylabel('t/c')
        box on
        grid on
    end
end
```

second_area_moment.m

```
% "second_area_moment.m" is part of the lifting line program
% "lifting_line_induction.m", intended for marine propeller design. This
% function calculates the second moment of area of an arbitrary cross
% section around the x-axis, according to the formula I = 1/12 bh^3.
%
% Part of the Master's Thesis "Unconventional Propeller Tip Design" by
% Andreas Ommundsen, June 2015.
% Norwegian University of Science and Technology (NTNU), Trondheim.

function I = second_area_moment(x,y,N)
    % Computes the second moment of area about the axis y = 0. Inputs the
    % half cross section, but the result is for the entire cross section.

    x_int = linspace(min(x),max(x),N);
    y_int = abs(interp1(x,y,x_int,'spline'));
    dx = x_int(2) - x_int(1);

    I = 0;
    for i = 1:(N - 1)
        % Numerical integration by the trapezoidal rule
        I = I + (1/12)*dx*((2*((y_int(i) + y_int(i+1))/2))^3);
    end
end
```

A.2 Example Output

Below are two example outputs from `lifting_line_induction.m` for a calculation on the conventional propeller with only ten lifting lines. The first is for $J = 0.92$ and converges well. The second is for $J = 0.19$ and is fairly unstable. It has also been calculated with a very low material yield strength.

```
Lifting line 1 of 10 converged in 7 iterations:
    Final residual Ua = 2.6658e-10
    Final residual Ut = 6.0199e-11

Lifting line 2 of 10 converged in 6 iterations:
    Final residual Ua = 3.1644e-12
    Final residual Ut = 5.1118e-11

Lifting line 3 of 10 converged in 8 iterations:
    Final residual Ua = 5.6354e-10
    Final residual Ut = 5.6939e-11

Lifting line 4 of 10 converged in 10 iterations:
    Final residual Ua = 7.6469e-11
    Final residual Ut = 3.3891e-12

Lifting line 5 of 10 converged in 10 iterations:
    Final residual Ua = 2.9865e-10
    Final residual Ut = 2.77e-11

Lifting line 6 of 10 converged in 10 iterations:
    Final residual Ua = 7.6151e-10
    Final residual Ut = 9.1804e-11

Lifting line 7 of 10 converged in 11 iterations:
    Final residual Ua = 5.4354e-10
    Final residual Ut = 9.3269e-11

Lifting line 8 of 10 converged in 11 iterations:
    Final residual Ua = 3.7381e-10
    Final residual Ut = 1.0047e-10

Lifting line 9 of 10 converged in 10 iterations:
    Final residual Ua = 8.7525e-11
    Final residual Ut = 2.7198e-11

Lifting line 10 of 10 converged in 8 iterations:
    Final residual Ua = 1.2566e-10
    Final residual Ut = 6.5555e-11

-------------------------------------------------------------------------------------------
FINAL RESULTS:
-------------------------------------------------------------------------------------------
Total thrust: 2091192.17 N
Total torque: 2926265.18 Nm
Efficiency: 82.6 %
Expanded Area Ratio: 0.72
P/D at 0.7R: 1.37
Advance number J = 0.92
-------------------------------------------------------------------------------------------
-------------------------------------------------------------------------------------------
```

```
WARNING: Lifting line 1 of 10 failed to converge:
    Final residual Ua = 4.4843
    Final residual Ut = 10.9629

Lifting line 2 of 10 converged in 10 iterations:
    Final residual Ua = 5.0329e-10
    Final residual Ut = 4.3041e-11

Lifting line 3 of 10 converged in 27 iterations:
    Final residual Ua = 6.6868e-10
    Final residual Ut = 1.5023e-11

Lifting line 4 of 10 converged in 35 iterations:
    Final residual Ua = 6.8425e-10
    Final residual Ut = 4.261e-12

Lifting line 5 of 10 converged in 39 iterations:
    Final residual Ua = 6.6064e-10
    Final residual Ut = 2.1707e-12

Lifting line 6 of 10 converged in 39 iterations:
    Final residual Ua = 5.9528e-10
    Final residual Ut = 5.377e-12

Lifting line 7 of 10 converged in 41 iterations:
    Final residual Ua = 6.7518e-10
    Final residual Ut = 1.368e-11

Lifting line 8 of 10 converged in 36 iterations:
    Final residual Ua = 9.1067e-10
    Final residual Ut = 3.9974e-11

Lifting line 9 of 10 converged in 27 iterations:
    Final residual Ua = 6.2874e-10
    Final residual Ut = 2.6354e-11

Lifting line 10 of 10 converged in 6 iterations:
    Final residual Ua = 6.1063e-10
    Final residual Ut = 3.9063e-11

WARNING: 1 of 10 lifting lines failed to converge.
--------------------------------------------------------------------------------
FINAL RESULTS (ignoring lifting lines that failed to converge):
--------------------------------------------------------------------------------
Total thrust: 2092443.84 N
Total torque: 1313820.12 Nm
Efficiency: 38.35 %
Expanded Area Ratio: 0.72
P/D at 0.7R: 0.74
Advance number J = 0.19
--------------------------------------------------------------------------------
WARNING: Danger of blade failure. Revise the thickness distribution.
--------------------------------------------------------------------------------
```